Optimization of ESPRESSO Fundamental Physics Tests

Ana Catarina de Oliveira Leite
Mestrado em Astronomia
Departamento de Física e Astronomia
2015

Orientador
Carlos J. A. P. Martins, Investigador, Centro de Astrofísica da Universidade do Porto

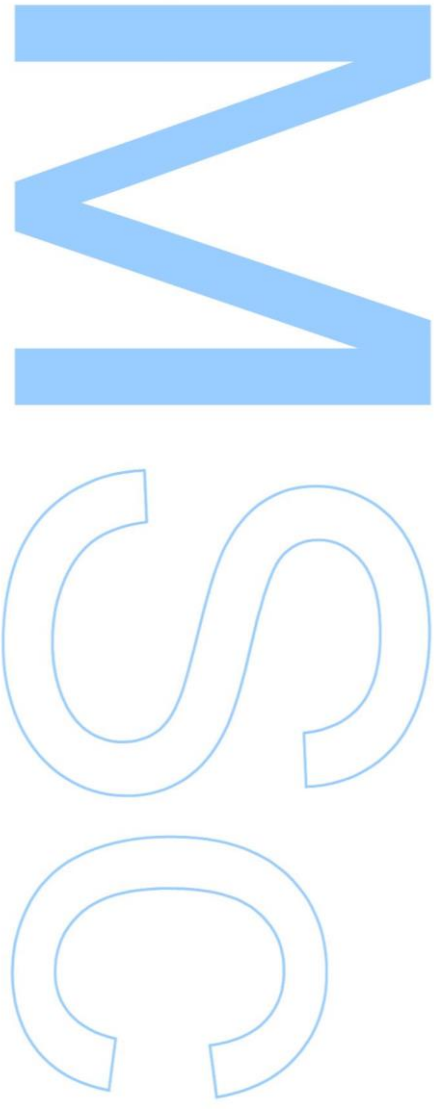

U.PORTO

FACULDADE DE CIÊNCIAS
UNIVERSIDADE DO PORTO

Todas as correções determinadas pelo júri, e só essas, foram efetuadas.

O Presidente do Júri,

Porto, _____/_____/_____

Acknowledgements

I would like to start by thanking my supervisor Carlos Martins for accepting me as his student when I was an undergraduate that knew little or nothing about cosmology and science. I thank him for all the support, opportunities and above all patience. An essential part of this work was to understand the transitions and the observational part of the variation of fundamental constants and for all the help and discussions I would like to thank Paolo Molaro. Others that in one way or another helped me to make sense of what I was doing when I didn't knew barely anything: Nelson Nunes, Luca Amendola, Stefano Cristiani and Hugo Messias.

I am grateful to the Gulbenkian Foundation for the support through Programa de Estímulo à Investigação 2014, grant no. 2148613525. To CAUP and FCUP for helping me in my path.

To my partners in Cosmology: Ana Marta, Miguel, José, David and Pauline: thank you for all the discussions about cosmology, astronomy and trivial life things as well. Big thanks to Pedro Pedrosa for introducing me to all the PCA tools. To my partners in the Master: Raquel you were our guardian angel, a great companion and the best of examples. Thank you. Tony thank you for all informatics advice.

To all 09: You are the main reason why Astronomy is worth it. Thank you for all the support when I was down and all that parties when we were up. Thank you Gil, for being the reason I survived the first years of University classes. Pedro, thank you for never leaving me alone, thank you for, when I am buried in work, keep reminding me that I need to sleep, eat, and live a little. Thank you for dancing with me like I'm a real Disney princess.

Last but not less important I'm very thankful to my parents, for the support and sacrifices you had to made for me. I will always be grateful to you for letting me follow my dreams. My brother, thank you for the sleepless nights talking about nothings, you are and will always be my dearest friend.

Abstract

ESPRESSO is a fiber-fed, cross-dispersed, high-resolution echelle spectrograph for ESO's VLT. Its first light is scheduled for 2016. One of the two scientific programs for the Consortium Guaranteed-Time Observations (GTO) is to study the possible variability of physical constants.

Quasar Absorption Spectral lines provide a precise test of the stability of the fundamental constants over cosmological times and distances. In this work a compilation and study of the existing measurements of the variation of the fine-structure constant, α, is presented, in order to build an optimized observational strategy for ESPRESSO'S GTO of the Consortium.

The measurements of a variation of α can be used to constrain dark energy. A Principal Component Analysis was performed combining Type Ia Supernovae with measurements of the stability of fundamental constants, with the purpose of quantifying the gains in sensitivity that can be expected from ESPRESSO and the high-resolution ultra-stable spectrograph for the E-ELT (ELT-HIRES) with future supernova surveys.

The observational strategy study for ESPRESSO GTO lead to the selection of 14 optimal targets for α measurements, that will allow to improve the constrains on its stability. The improvements of these measurements by themselves on dark energy will not produce accurate results but a bigger sample of targets and/or synergies with other datasets are promising.

Keywords

Fundamental constants, Dark energy, High resolution spectroscopy, Quasar absorption spectra, ESPRESSO

Resumo

O ESPRESSO é um espetrógrafo echelle de alta resolução, de dispersão cruzada, alimentado por fibras, para o telescópio VLT do ESO. O seu início de operações está planeado para 2016. Um dos dois objetivos científicos principais do Consórcio do instrumento para o programa do Tempo Garantido de Observação (GTO) é estudar a possível variação de constantes físicas.

Riscas de absorção em espetros de quasares proporcionam uma ferramenta para realizar testes precisos da estabilidade de constantes fundamentais ao longo de diferentes tempos e distâncias cosmológicas. Neste trabalho a compilação e estudo de medidas já existentes da constante de estrutura fina, α, é apresentada com o intuito de construir uma estratégia observacional otimizada para o GTO do Consórcio do ESPRESSO.

Medições da variação de α podem ser usadas para obter informação sobre energia escura. Dados de Supernovas tipo Ia conjuntamente com medições da estabilidade de constantes fundamentais foram usadas numa Análise Principal de Componentes para quantificar os ganhos em sensibilidade esperados para o ESPRESSO, o espetrógrafo de alta-resolução ultra-estável para o E-ELT (ELT-HIRES) e ainda futuras missões de Supernovas.

O estudo da estratégia observacional para o GTO do ESPRESSO conduziu à seleção de 14 alvos ideias para realizar medições de α que possibilitarão melhorar o teste dos limites à sua estabilidade. Os ganhos que esta lista de medições pode trazer para a energia escura não trará resultados precisos mas uma lista maior e/ou sinergias com outros tipos de medições são promissoras para o futuro.

Palavras-chave

Constantes fundamentais, Energia escura, Espetroscopia de alta-resolução, Espetros de absorção de Quasares, ESPRESSO

Contents

List of Figures

List of Tables

Chapter 1.

Introduction

This work is focused on the search for the variation of fundamental couplings, mainly the fine-structure constant α. It aims to study the dataset of existing data and with that information choose the priority targets for the Guaranteed Time of Observation (GTO) of the ESPRESSO Consortium. We aim to choose the targets with the higher potential to give us a detection and/or test the allegation of a dipole in the sky (Webb et al. 2011). In addition to this primary goal, this thesis explored the potential that this kind of stability tests have to constrain our knowledge of Dark Energy, by themselves and combined with future surveys of type Ia Supernovae.

Part of the work done in the context of this thesis has been reported in Leite et al. (2014) and Leite & Martins (2015) and uses methods initially developed in Amendola et al. (2012) .

1.1 COSMOLOGY

This section will be a simple presentation of the cosmological background necessary to understand the motivation and necessity to test the models that describe our Universe. This section is based on the books by Liddle (2003) and Mo et al. (2010).

Geometry

In general relativity, the fundamental quantity is the metric which describes the geometry of space-time, by giving the distance between neighbouring points in space-time. Consider first the metric of a flat 2D surface, upon which points can be specified by coordinates x_1 and x_2. The

distance ds between two points is given by

$$\Delta s^2 = \Delta x_1^2 + \Delta x_2^2, \tag{1.1}$$

where Δx_1 and Δx_2 are the separations in the x_1 and x_2 coordinates. Now suppose that the surface is no longer a flat surface and is expanding. The physical distance between points would grow with time, and if the expansion is uniform (i.e. independent of position) we would get:

$$\Delta s^2 = a(t)^2[\Delta x_1^2 + \Delta x_2^2], \tag{1.2}$$

where $a(t)$ measures the rate of expansion. The coordinates x_1 and x_2 are comoving coordinates, this is, coordinates carried along with the expansion, that relate to a real distance r in the following way: $\vec{r} = a(t)\vec{x}$.

In general relativity we are interested in the distance between points in four dimensional space-time, and we must also allow for the possibility that space-time might be curved. The separation can be written as

$$ds^2 = \sum_{\mu,\nu} g_{\mu\nu} dx^\mu dx^\nu, \tag{1.3}$$

where $g_{\mu\nu}$ is the metric, μ and ν are indices taking the values 0, 1, 2 and 3, where x^0 is the time space coordinate and x^1, x^2 and x^3 the three spatial coordinates. In general the metric is a function of the coordinates (indeed, to describe a curved space-time there must be some such dependence), and the distances are written in infinitesimal notation as once space-time is curved it only makes sense to give the distance to nearby points. We now assume the cosmological principle that, at a given time, the Universe should not have any preferred locations. This requires that the spatial part of the metric has a constant curvature and the most general spatial metric that satisfy this can be written as

$$ds_3^2 = \frac{dr^2}{1 - kr^2} + r^2(d\theta^2 + sin^2\theta d\Phi^2), \tag{1.4}$$

where ds_3 refers only to the spatial dimensions, and spherical polar coordinates have been

used. k is an undetermined constant which measures the curvature of space. The possibilities for the spatial geometry are: $k > 0$ - spherical; $k = 0$ - flat; $k < 1$ - hyperbolic. time.

The missing dependencies that one can put in the equation are the time dependences, allowing the space to grow or shrink with time. This leads us to the Friedmann-Lemaître-Robertson-Walker metric

$$ds^2 = -c^2dt^2 + a(t)^2\frac{dr^2}{1-kr^2} + r^2(d\theta^2 + sin^2\theta d\phi^2), \tag{1.5}$$

where t is the cosmic time, which is the time seen by an observer moving along with the expansion of the Universe, and $a(t)$ is the scale factor which describes the time-variation of the distance between two objects in the universe. By definition $a(t_0)$ is the scale factor at t_0, the present time.

An important property of light propagation is that it obeys: $ds = 0$. This means that a light ray travels no distance at all in space-time. At a given time all points in space are equivalent, so for simplicity we can consider a light ray propagating radially from $r = 0$ to $r = r_0$, giving $d\theta = d\phi = 0$. For this radial light ray is true by the equation (1.5) that

$$\frac{cdt}{a(t)} = \frac{dr}{\sqrt{1-kr^2}} \tag{1.6}$$

The radial comoving distance for the ray to go from $r = 0$ to $r = r_0$ is defined as

$$\chi = \int_{t_e}^{t_r} \frac{cdt}{a(t)} = \int_0^{r_0} \frac{dr}{\sqrt{1-kr^2}} \tag{1.7}$$

where t_e stands for time of emission and t_r for reception. Now consider a light ray emitted a short time interval later, so the emission time is $t_e + dt_e$. The galaxies are still at the same coordinates,

so we can get the time of reception, $t_r + dt_r$, from a similar integral

$$\int_{t_e+dt_e}^{t_r+dt_r} \frac{cdt}{a(t)} = \int_0^{r_0} \frac{dr}{\sqrt{1-kr^2}}. \tag{1.8}$$

Since the distance travelled by the photon is the same in these coordinates, then

$$\int_{t_e}^{t_r} \frac{cdt}{a(t)} = \int_{t_e+dt_e}^{t_r+dt_r} \frac{cdt}{a(t)}, \tag{1.9}$$

The only difference in the integrals can only occur at the edges since the main part of the domain of the integral is the same; from that, comes

$$\int_{t_e}^{t_e+dt_e} \frac{cdt}{a(t)} = \int_{t_r}^{t_r+dt_r} \frac{cdt}{a(t)} \iff \frac{dt_r}{a(t_r)} = \frac{dt_e}{a(t_e)} \tag{1.10}$$

In an expanding Universe, $a(t_r) > a(t_e)$, so $dt_r > dt_e$. Now imagine that, instead of being two separate rays, they correspond to successive crests of a single wave. As the wavelength is proportional to the time between crests, λ is proportional to dt that is also proportional to $a(t)$ so

$$\frac{\lambda_r}{\lambda_e} = \frac{a(t_r)}{a(t_e)} \tag{1.11}$$

The interpretation is that light is stretched as it travels across the Universe. If we want to compare observed absorption lines with the ones in the laboratory, we can define the shift as being

$$z \equiv \frac{\lambda_r - \lambda_e}{\lambda_e} \Leftrightarrow 1 + z = \frac{\lambda_r}{\lambda_e} \Leftrightarrow 1 + z = \frac{a(t_r)}{a(t_e)}, \tag{1.12}$$

z is typically called redshift. It will always be greater than zero in an expanding Universe, and $z \to \infty$ would be light emitted ever closer to the Big Bang. Referring to the Universe at a redshift of z means the time when the Universe was $1/(1+z)$ of its present size.

General Relativity

The evolution of the metric is given by the Einstein equations:

$$R^{\mu}_{\nu} - \frac{1}{2} g^{\mu}_{\nu} R = \frac{8\pi G}{c^4} T^{\mu}_{\nu}, \tag{1.13}$$

where T^{μ}_{ν} is the energy-momentum tensor of any matter which is present, and R^{μ}_{ν} and R are the Ricci tensor and scalar respectively, which give the curvature of space-time.

Einstein's equations tell us how the presence of matter curves space-time, and so we need to describe the matter under consideration. The possible constituents of the Universe are usually considered to be perfect fluids, and then the energy-momentum tensor would be

$$T^{\mu}_{\nu} = diag(-\rho c^2, p, p, p), \tag{1.14}$$

ρ being the mass density and p the pressure.

The time-time Einstein equation gives the Friedmann equation:

$$\left(\frac{\dot{a}}{a}\right)^2 + \frac{kc^2}{a^2} = \frac{8\pi G}{3}\rho, \tag{1.15}$$

Another important equation that arises from the Einstein equations is:

$$2\frac{\ddot{a}}{a} + \left(\frac{\dot{a}}{a}\right)^2 + \frac{kc^2}{a^2} = -\frac{8\pi G}{c^2}p. \tag{1.16}$$

From these two previous equations the fluid equation can be derived:

$$\dot{\rho} + 3\frac{\dot{a}}{a}\left(\rho + \frac{p}{c^2}\right) = 0. \tag{1.17}$$

The fluid equation maintains energy conservation for the fluid as the Universe expands.

The Hubble parameter, $H(t)$, at a cosmic time t is defined to be the rate of change of the proper

distance d between any two fundamental observers at time t in units of r: $dr/dt \equiv H(t)r$, then we can define it as $H(t) = \dot{a}/a$, denoting $a = a(t)$ for simplification of notation.

Applying the Hubble parameter and rearranging the equation (1.15), (1.16) and (1.17) we get the set of three equations that define the dynamics of an isotropic and homogenous Universe:

$$\begin{cases} H^2 + \frac{k}{a^2} = \frac{8\pi G}{3}\rho \\ \frac{\ddot{a}}{a} = -\frac{4\pi G}{3}(\rho + 3p) \\ \dot{\rho} + 3H\left(\rho + p\right) = 0. \end{cases} \tag{1.18}$$

The first equation is the Friedmann equation, the second one is the Raychaudhuri equation and the last one is the conservation of energy. The c is used in natural units, $c = 1$.

Components of the Universe

From the Friedmann equation in (1.18), one can define a critical density for which $k = 0$, that is, the Universe would be flat:

$$\rho_c = \frac{3H^2}{8\pi G} \tag{1.19}$$

If we define $\Omega \equiv \rho/\rho_c$, as a dimensionless energy density parameter, then the Friedmann equation can be rewritten as

$$\frac{k}{a^2H^2} = \Omega - 1 \tag{1.20}$$

In the same way as before:

- $\Omega(t) < 1 \rightarrow k < 0$ - implies a close Universe;
- $\Omega(t) = 1 \rightarrow k = 0$ - implies a flat Universe;
- $\Omega(t) > 1 \rightarrow k > 0$ - implies an Universe.

The Universe is composed by 3 main components: Matter, Radiation and Dark Energy. Each of these components can be characterized by its relative density (Ω_X), and equation of state ($\omega_X = p_X/\rho_X$). **Matter** is composed of non-relativistic particles with a very low pressure, $P_m = 0$ and thus an equation of state $\omega_m = 0$. And it's usually separated in ordinary matter and dark matter components. **Radiation** is composed of relativistic particles and also includes neutrinos and photons, its pressure is given by $P_r = \omega_r \rho$, and the equation of state $\omega_r = 1/3$. **Dark Energy** is considered to be the component responsible for the Universe's accelerated expansion, its pressure follows $P_\Lambda < -\rho/3$, with an equation of state $\omega_\Lambda < -1/3$. The standard cosmological model considers dark energy to be a vacuum energy (or a cosmological constant) with $\omega_{vac} = -1$.

Considering the three components relative densities (Ω_m - matter, Ω_r - radiation, Ω_Λ - dark energy) and the contribution from curvature to be: $\Omega_k = -k/(a^2H^2)$, the Friedmann equation can be written as

$$\Omega_m(t) + \Omega_r(t) + \Omega_\Lambda(t) + \Omega_k(t) = 1, \tag{1.21}$$

The equation of energy conservation in (1.18) can be written using the constant equation of state parameter

$$\frac{\dot{\rho}}{\rho} = -3(1+w)\frac{\dot{a}}{a}, \tag{1.22}$$

that can be used to represent the different components of the Universe and compute its evolutions

$$\frac{\dot{\rho_X}(t)}{\rho_{X,0}} = \left(\frac{a(t)}{a_0}\right)^{-3(1+\omega)}, \tag{1.23}$$

the 0 subscript stands for the values today. Applying, to the previous equation, the correspondent ω_X (and assuming they are constant), one gets

$$\begin{cases} \frac{\dot{\rho}_m(t)}{\rho_{m,0}} = \left(\frac{a(t)}{a_0}\right)^{-3} & \text{matter} \\ \frac{\dot{\rho}_r(t)}{\rho_{r,0}} = \left(\frac{a(t)}{a_0}\right)^{-4} & \text{radiation} \\ \frac{\dot{\rho}_\Lambda(t)}{\rho_{\Lambda,0}} = 1 & \text{dark energy.} \end{cases} \tag{1.24}$$

For this description of the expanding Universe, the radiation dominates at early times, till the redshift at which the Universe becomes matter dominated (z_{eq}), and finally the dark energy became dominant at late times. The latest Planck data (Planck Collaboration et al. 2014) say that its composition is 68.3% of dark energy, 26.8% dark matter and 4.9% of ordinary matter.

Dark Energy

One of the problems of the modern Cosmology is to understand if Dark Energy is indeed a Cosmological Constant or if has some other explanation. The most simple explanation is assuming a fluid with negative pressure with uniform vacuum energy, leading to an equation of state of $\omega = -1$. But this required vacuum energy is many orders of magnitude smaller than the expected in the standard model of particle physics, which gives rise to the Cosmological Constant problem.

If we assume that the ω is constant but not equal to -1 through cosmological times we would get the general expression using equation (1.23)

$$\frac{\dot{\rho}_D E(t)}{\rho_{DE,0}} = \left(\frac{a(t)}{a_0}\right)^{-3(1+\omega)} \tag{1.25}$$

that leads to a different Friedmann equation

$$H^2(z) = H_0^2 \left[\Omega_{m,0}(1+z)^3 + \Omega_{DE,0}(1+z)^{3(1+\omega)}\right], \tag{1.26}$$

the equation assumes that when the Dark Energy component is relevant, the radiation contribution can be ignored. The equation has been adapted from a to z. This parametrization can be

tested by different astrophysical observables.

Another alternative for the Cosmological Constant involves scalar fields, an example of which is the recently discovered Higgs field (Aad et al. 2012, Chatrchyan et al. 2012). Observationally, the main differences are that not only the density of dark energy is allowed to change but its equation of state changes too. One way to distinguish models is by testing the equation of state of dark energy in different epochs in the Universe.

A simple example is a quintessence model, described by a scalar field ϕ minimally coupled to gravity. The action of this scalar field is

$$S = -\int d^4x\sqrt{-g}\left[\frac{1}{2}(\nabla\phi)^2 - V(\phi)\right] + S_m, \tag{1.27}$$

where the kinetic energy of the field can be rewritten as $(\nabla\phi)^2 = g^{\mu\nu}\partial_\mu\phi\partial_\nu\phi$, and the $V(\phi)$ is the potential of the field. S_m represents the matter action.

Using the Friedmann-Lemaître-Robertson-Walker metric and the above action we get the evolution of the field with time:

$$\ddot{\phi} + 3H\dot{\phi} + \frac{dV}{d\phi} = 0, \tag{1.28}$$

Considering a perfect fluid we get:

$$\rho_\phi = \frac{1}{2}\dot{\phi}^2 + V(\phi) P_\phi = \frac{1}{2}\dot{\phi}^2 - V(\phi) \tag{1.29}$$

And then the equation of state of the field is defined as

$$\omega_\phi = \frac{P_\phi}{\rho_\phi} = \frac{\dot{\phi}^2 - 2V(\phi)}{\dot{\phi}^2 - 2V(\phi)} \tag{1.30}$$

In general these quintessence models can be separated in 2 classes, called "thawing" and "freezing", according to their evolution (Caldwell & Linder 2005). The main distinction between them, in terms of the equation of state, is that, for thawing models at early time the equation of state of the field is $\omega_\phi \sim -1$ and moves towards less negative values, whilst the freezing models having $\omega_\phi > -1$ initially and then they evolve towards $\omega_\phi \sim -1$.

A dynamical scalar field to explain the Dark energy component would need to be slow-rolling close to the present day. It then follows that if the field couples to the rest of the model - which it will naturally do, unless some new symmetry is postulated to suppress the couplings - it will lead to potentially observable long-range forces and time dependencies of the constants of nature. (Martins 2015)

1.2 FUNDAMENTAL CONSTANTS

Physical constants have a fundamental importance in science as they are responsible for defining the magnitudes of the physical processes. A fundamental constant can be defined as being a parameter that cannot be explained by the theory. They are quantities that can only be measured. As discussed in Uzan (2011), they are assumed to be constant in theoretical framework for two reasons:

- *The considered framework does not provide any way to compute these parameters, i.e., it does not have any equation of evolution for them since otherwise it would be considered as a dynamical field;*
- *These parameters can only be measured. If the theories in which they appear have been validated experimentally, it means that, at the precisions of these experiments, these parameters have indeed been checked to be constant, as required by the necessity of the reproducibility of experimental results.*

Testing the constancy of this parameters is in itself a test of the theories where they are used. They allow us to test the domain of their validity and if their constancy doesn't hold true to expand our knowledge.

Variation of Fundamental Constants

When testing the variation of constants one needs to be careful about which ones to test. Dicke (1962) pointed out the important difference between dimensional and dimensionless constants. For example, when testing the time taken for the light to travel between two points, if one finds

two different values for the speed of light, c, in different days, one might conclude that this implies a varying c. An equally valid conclusion could be a varying meter rule and/or a varying clock. In order to test a change in a dimensional quantity, like c, specifying which units are to be held fixed is necessary. In order to avoid this problem, one should test the stability of fundamental constants searching for variations in dimensionless quantities. Detection of variation in a dimensionless quantity guarantees that it is the quantity under consideration which is changing, and would therefore unambiguously imply that physics is changing. Two of these fundamental constants are the proton-to-electron mass ratio, μ, and fine-structure constant, α.

The proton-to-electron mass ratio, μ, is defined as the ratio between proton mass, m_p, and the electron mass, m_e, through the expression: $\mu \equiv m_p/m_e$. The current 2014 CODATA recommended value is $\mu = 1836.15267389(17)$ (Mohr et al. 2015). μ is related with the interplay between the strong and electroweak sectors of particle physics.

The fine-structure constant, α, is defined in cgs units as: $\alpha \equiv e^2/\hbar c$, where e is the electron charge, $\hbar$ is Planck's constant, and c is the speed of light. The current 2014 CODATA recommended value is $\alpha = 1/137.035999139(31)$ (Mohr et al. 2015). In quantum electrodynamics, α represents the strength of the coupling between the electron and the photon, and therefore determines the effective strength of the electromagnetic force.

Another parameter that will be relevant for this work is the T_{CMB}. If gravitation is described by general relativity and electromagnetism by Maxwell theory then photons propagate along null geodesics and the CMB black-body temperature must follow the relation:

$$T_{\rm CMB}(z) = T^0_{\rm CMB} \times (1+z)^{1-\beta}, \tag{1.31}$$

with $\beta = 0$ and where $T^0_{\rm CMB}$ = 2.725±0.002 K (Mather et al. 1999) is the temperature measured locally (at redshift $z = 0$). This relation, which is a theoretical consequence of the adiabatic expansion of the Universe, needs to be verified by direct measurements (Noterdaeme et al. 2011). In practice, spectroscopic measurements probe:

$$\frac{\delta T}{T}(z) = \frac{T_{true}(z) - T_{std}(z)}{T_{std}(z)}. \tag{1.32}$$

Models of Dark energy with Varying Constants

One can use scalar fields to get a direct connection from the variation of the fine structure constant with the evolution of the Dark Energy equation of state, $\omega(z)$. Let us consider the standard class of models for which the variation of the fine-structure constant α is linearly proportional to the displacement of a scalar field, and further assume that this field is a quintessence type field, this is, responsible for the current acceleration of the Universe as in Dvali & Zaldarriaga (2002), Chiba & Kohri (2002), Anchordoqui & Goldberg (2003), Copeland et al. (2006), Marra & Rosati (2005), Dent et al. (2009). We take the coupling between the scalar field and electromagnetism to be

$$\mathcal{L}_{\phi F} = -\frac{1}{4} B_F(\phi) F_{\mu\nu} F^{\mu\nu}, \tag{1.33}$$

where the gauge kinetic function $B_F(\phi)$ is linear,

$$B_F(\phi) = 1 - \zeta\kappa(\phi - \phi_0), \tag{1.34}$$

$\kappa^2 = 8\pi G$ and ζ is the coupling constant. This can be seen as the first term of a Taylor expansion, and should be a good approximation if the field is slowly varying at low redshift. Then, the evolution of α is given by

$$\frac{\Delta\alpha}{\alpha} \equiv \frac{\alpha - \alpha_0}{\alpha_0} = \zeta\kappa(\phi - \phi_0)\,. \tag{1.35}$$

For a flat Friedmann-Lemaître-Robertson-Walker Universe with a canonical scalar field, $\dot{\phi}^2 = (1+\omega(z))\rho_\phi$, hence, for a given dependence of the equation of state parameter $\omega(z)$ with redshift, the scalar field evolves as

$$\phi(z) - \phi_0 = \frac{\sqrt{3}}{\kappa} \int_0^z \sqrt{1+\omega(z)} \left(1 + \frac{\rho_m}{\rho_\phi}\right)^{-1/2} \frac{dz}{1+z}. \tag{1.36}$$

where we have chosen the positive root of the solution, since we physiccaly expect that the field is rolling down its potential. Note that this allows us to write the evolution of α as

$$\frac{\Delta\alpha}{\alpha}(z) = \zeta \int_0^z \sqrt{3[1+\omega(z)]\Omega_\phi(z)}\frac{dz}{1+z}\,, \tag{1.37}$$

where $\Omega_\phi = \rho_\phi/(\rho_m + \rho_\phi)$ is the fraction of the universe's energy in the scalar field. Analogous derivations could be done, in other cases - for example, phantom fields.

In chapter 4, a principal component analysis will be used to test the potential of the measurements of variation of α to constrain the equation of state of dark energy, assuming this model parametrization. To test that we will need to assume some fiducial equation of state parameters, and we will specially consider three:

$$\omega_c(z) = -0.9, \tag{1.38}$$

$$\omega_s(z) = -0.5 + 0.5\tanh\left(z - 1.5\right), \tag{1.39}$$

$$\omega_b(z) = -0.9 + 1.3\exp\left[-\tfrac{(z-1.5)^2}{0.1}\right]. \tag{1.40}$$

At a phenomenological level, these describe the three qualitatively different interesting scenarios: an equation of state that remains close to a cosmological constant throughout the probed redshift range, one that evolves towards a matter-like behaviour by the highest redshifts probed, and one that has non-trivial features over a limited redshift range, perhaps associated to a low-redshift phase transition (see Mortoson et al. (2009) for further discussion). We will refer to them as the *constant*, *step* and *bump* fiducial models, respectively.

Chapter 2.

Spectroscopic Measurements of Fundamental Constants

Quasar (QSO) absorption spectra are powerful laboratories to test the variation of fundamental constants. Absorption lines produced by the intervening clouds along the line of sight of the QSO give access to physical information on the atoms present in the cloud, this means that they give access to physics at different cosmological times and places. An illustrative representation of the QSO spectra and the information contained in is presented in Fig. 2.1.

Three important characteristics/components of quasar spectra make them important to perform measurements of constant variations:

- The Lyman-α forest - caused by absorption of intervening HI along the line of sight to the quasar. Reservoirs of neutral hydrogen are associated with damped Lyman-α systems (DLAs), which are also associated with molecular hydrogen absorption. When these systems have column densities of H_2 in the range between $logN[H_2/cm^{-2}] \backsim 14$ and 18, they are considered systems than can yield a $\Delta\mu/\mu$ measurement. A column density outside this range would either yield a small number of detectable H_2 transitions or a high number of saturated transitions. It's possible to use other molecular species to do this QSO μ measurements, such as HD and CO. They have similar sensitivities to the variation of μ but normally their column densities are $\sim 10^5$ times smaller than the ones from H_2. (J. Bagdonaitė Ph.D. Thesis 2015)

- The quasar spectra display, redshifted from the Lyman-α forest, metal absorption lines[1], which can be due to the presence of this elements in clouds associated either with the

[1] any element more massive than Helium

material of the galaxy that hosts of the QSO, or related with some other different objects at other cosmological distances in the same line of sight. These lines are sensitive to α variation, and each element presents a different sensitivity to it. A single line can not be used to measure $\Delta\alpha/\alpha$ because the redshift of the absorbing system is unknown but when combining two or more transitions that have different sensitivities, and therefore different effects in the line position on the spectra, the effect of redshift is no longer degenerate for the measurement. In the following section of this chapter: 2.1, three existing methods to combine different metal absorption lines will be presented.

- The presence of absorption features associated with the *CO* molecule if detected allows to test the $T_{CMB}(z)$ (i.e. test equation (1.31), because its energy differences between rotational levels are close to $kT_{\rm CMB}$ at high redshift. *CO* has been detected in absorption only very recently at high-z. Other molecules can be used to measure T_{CMB}, but *CO* is the only one SNR limited. This kind of measurement is more usual using the *CN* molecule, which has proven to be a remarkable thermometer of the CMB in the Galaxy. The fact that *CN* is not used for $T_{CMB}(z)$ is simply because it has not been detected in diffuse gas at high redshift. (Noterdaeme et al. 2011)

A general discussion of the method used to test the variation of the dimensionless constants is presented in King's Ph.D. Thesis (2012): for a dimensionless constant, P, and observable quantity, O, one attempts to derive a change in the observed quantity as a function of a change in a relevant dimensionless ratio

$$\Delta O = k\frac{\Delta P}{P} + \mathcal{O}\left(\frac{\Delta^2 P}{P^2}\right), \tag{2.1}$$

where k determines the sensitivity to the effect; for a particular circumstance k is referred to as the "sensitivity coefficient". The second order term can be neglected in almost all circumstances as the variations in the fundamental constants, if they occur, are small in all regimes. In many circumstances, multiple dimensionless constants are relevant to the problem, in which case this

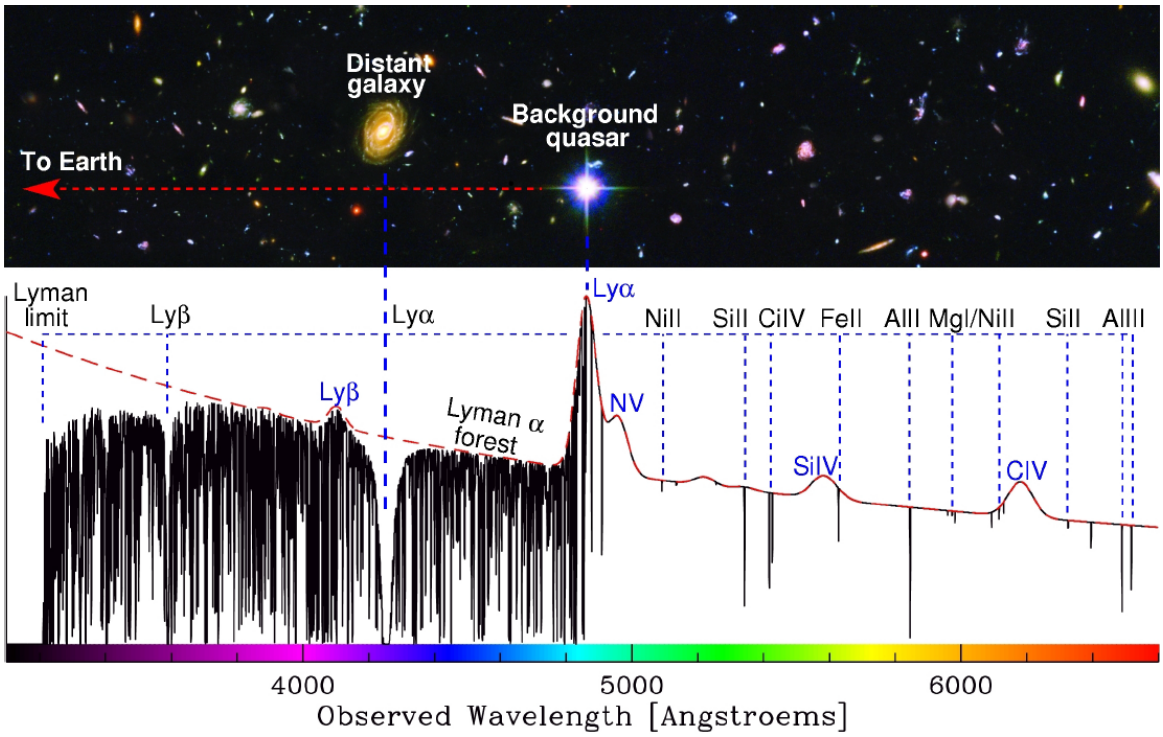

Figure 2.1: Schematic overview of a quasar spectrum. The emission line marked "Lyα" at $\lambda \sim 4950$Å is due to Lyman-α emission by the quasar. Bluewards of the Lyman-α emission peak is a dense series of absorption lines - the Lyman-α forest - caused by absorption by intervening HI along the line of sight to the quasar. Clouds with sufficiently high HI column density display damped wings, and are known as Damped Lyman-α absorbers if the HI column density is greater than $2 \times 10^{20} cm^{-2}$. Other HI absorbers - Lyman limit systems (LLSs) - still have sufficiently high column densities, of $N(HI) \geqslant 2 \times 10^{17} cm^{-2}$, to cause a substantial drop in the transmitted quasar flux below the Lyman limit (at ~ 911.8Å in the rest frame of the absorber). A LLS is indicated in this system by the "distant galaxy" and absorption at $\lambda \sim 4250$Å. Metal lines are often observed redwards of the Ly-α emission peak, indicated here by the narrow absorption lines corresponding to NiII, SiII, CIV, FeII, AlII and AlIII (all in black text). These are due to metal line absorption along the line of sight to the quasar. Metal lines also fall in the Ly-α forest, but are often observed out of the forest simply because some transitions possess rest wavelengths significantly longer than the 1216Å Lyman-α line. These metal lines prove useful to search for a change in α. The redshifted transitions of molecular hydrogen, which can be used to search for a change in μ, all have rest wavelengths shorter than 1216Å, and therefore are observed only in the Lyman-α forest. All absorption and emission is observed with respect to an underlying power law spectrum, indicated by the dashed red line. Diagram by: Michael Murphy, Swinburne University of Technology, Melbourne, Australia. (King's Ph.D. Thesis 2012)

becomes a sum over the constants of interest,

$$\Delta O = \sum_i k_i \frac{\Delta P_i}{P_i}. \tag{2.2}$$

One then compares the observations of O at different time periods to probe temporal evolution in the various P_i, or at different places to probe spatial variation in P_i.

From the observational point of view the variation in μ and α are then defined as:

$$\frac{\Delta \mu}{\mu} \equiv \frac{\mu_z - \mu_0}{\mu_0}, \tag{2.3}$$

where μ_z is the measurement of μ at some redshift z, and μ_0 is the laboratory value. In the same

way:

$$\frac{\Delta\alpha}{\alpha} \equiv \frac{\alpha_z - \alpha_0}{\alpha_0}. \tag{2.4}$$

2.1 VARIATION OF THE FINE STRUCTURE CONSTANT

AD, MM and SIDAM

QSO metal absorption lines are capable of testing the stability of α. One QSO line of sight can have several absorption systems, that originate in clouds at different redshifts. Typically a single absorption system (absorption lines originated in the same cloud/object) has more than just one ionized species creating signatures in the QSO spectra. The information of the multiple transitions can be combined. The velocity complexity of the cloud produces a broadening effect that is taken into account when studying the transitions, by fitting different components/parts of the cloud.

There are three methods to use these transitions and compute the $\Delta\alpha/\alpha$ measurement. A detailed description of the three methods can be found in King's Ph.D. Thesis (2012), Murphy's Ph.D. Thesis (2002) and Uzan (2011), here I will summarize some aspects of each one of them.

For an **alkali doublet** (AD), the separation between the two fine-structure transitions scales as α^2 (Bethe et al. 1977). For a small change in α, $\Delta\alpha/\alpha \equiv (\alpha_z - \alpha_0)/\alpha_0$, (where $|\Delta\alpha/\alpha| \ll 1$), the change in the doublet separation is given by

$$\frac{\Delta\alpha}{\alpha} = \frac{c}{2}\left[\frac{(\Delta\lambda)_z}{(\Delta\lambda)_0} - 1\right], \tag{2.5}$$

where $(\Delta\lambda)_z$ and $(\Delta\lambda)_0$ are the relative doublet separations in the cloud rest-frame, at redshift z, and in the laboratory. The constant c [2] is different for different doublets, and accounts for higher order relativistic effects. In practice one compares the observed relative spacings in quasar spectra with laboratory spectra to determine $\Delta\alpha/\alpha$. Because two transitions are being used, $\Delta\alpha/\alpha$ is not degenerate with the determination of the redshift. The AD method does not make

[2] not to be confused with the speed of light

use of all available information in the quasar spectra.

The **many multiplet** (MM) makes use of different atomic transitions that have significantly larger sensitivities to a variation in α than the ones for the alkali doublets. A general application for the MM method is described below.

If α varies, the energy level of a given transition varies such that:

$$\omega_z = \omega_0 + q_1 x_z + q_2 y_z, \tag{2.6}$$

where ω_z is the wavenumber of the transition in the rest-frame of the cloud at redshift z. x_z and y_z are related to $\Delta\alpha/\alpha$:

$$x_z = \left(\frac{\alpha_z}{\alpha_0}\right)^2 - 1 \quad \text{and} \quad y_z = \left(\frac{\alpha_z}{\alpha_0}\right)^4 - 1. \tag{2.7}$$

If $\alpha_z \neq \alpha_0$ then x_z and y_z are non-zero and the magnitude and sign of q_1 and q_2 determine the shift in the transition wavenumber. Since we only consider $\Delta\alpha/\alpha \ll 1$, we can write:

$$\omega_z = \omega_0 + q x_z. \tag{2.8}$$

where q_1 and q_2 consolidate into $q = q_1 + 2q_2$.

The sign and magnitude of q differs significantly depending on the species and transition under consideration. Ultimately it is not the actual value of q that constrains $\Delta\alpha/\alpha$, due to the need to simultaneously determine the redshift of the absorber, but the differences in the q values between different transitions used.

Note that

$$\left(\frac{\alpha_z}{\alpha_0}\right)^2 - 1 = \left(\frac{\Delta\alpha}{\alpha}\right)^2 + 2\left(\frac{\Delta\alpha}{\alpha}\right) \approx 2\left(\frac{\Delta\alpha}{\alpha}\right), \tag{2.9}$$

where the approximation is valid for $|\Delta\alpha/\alpha \ll 1|$. From equation 2.8, the velocity shift($\Delta v/c \approx \Delta\lambda/\lambda = -\Delta\omega/\omega$), Δv, for a given transition is thus given by

$$\Delta v \approx -\frac{2cq_i}{\omega_0}\left(\frac{\Delta\alpha}{\alpha}\right) = -2cq_i\lambda_0\left(\frac{\Delta\alpha}{\alpha}\right), \tag{2.10}$$

where q_i is the q coefficient for the transition.

The main advantages and limitations of the MM over the AD method are (Murphy's Ph.D. Thesis 2002):

- Sensitivity gain (in the best case one order of magnitude) - maximal Δq of ~ 4000, potentially much larger than AD method ($\Delta q \sim 500$ for *SiIV*);
- Statistical advantage simply through the use of more data (transitions) - the velocity structure of the absorber is better constrained and is more likely to be a good representation of the physical processes;
- When MM uses transitions with both positive and negative q coefficients the systematic effects are minimized;
- MM assumes that the transitions arise from the same location, which may be not true for a inhomogeneous cloud.

A particular case of the MM method is **Single Ion Differential α Method** (SIDAM) which measures shifts between transitions of only one species (usually *FeII*). Whilst this does address the potential concern of spatial origin between different species, it also implies a reduction of sensitivity relative to the full MM method.

The SIDAM has some limitations: it relies on *FeII* transitions and their q coefficients. If Δq is low it can lead to a worse measurement. All *FeII* transitions have a similar $q \sim 1500$ except for the $\lambda = 1608$Å that has a $q \sim -1300$ (see table B.1 in Appendix B). Because of that the SIDAM method is very dependent of the presence of this specific transition, and any error in the $\lambda 1608$ laboratory wavelength, q coefficient determination and/or any problem with spectra contamination in this transition will significantly affect the measured value of $\Delta\alpha/\alpha$.

Characteristics of Transitions

The table B.1, from King's Ph.D. Thesis (2012), presents information of all the transitions used to do measurements of variation in α . The table presents the laboratory wavelength and the coefficient of sensitivity. These measurements assume an isotopic abundance of the elements equal to the solar one, which can be a dangerous assumption.

Some of these transitions present positive q (*TiII* 3067, 3073, 3230, 3242, 3384; *CrII* 2056; *MnII* 2576, 2594, 2606; *FeII* 1611, 2260, 2344, 2374, 2382, 2586, 2600; *ZnII* 2026, 2062) meaning that the shifts detected in the spectra would be to the higher wavelengths. The negative q, that shift to the blue, are fewer (*CrII* 2062, 2066; *FeII* 1608; *NiII* 1741, 1751) but this property makes them important. A high Δq, particularly when a measurement is done with both negative and positive sensitive transitions, assures that the systematic effects due to redshift uncertainties are much lower, or even non-existent.

Anchor transitions have an important role too. Anchor transitions are transitions that have low q coefficient (*MgI* 2026, 2852; *MgII* 2796, 2803: *AlII* 1670; *AlIII* 1854, 1862; *SiII* 1526, 1808; *SiIV* 1393, 1402), because of that they are good tools for calibration of the spectra.

The SIDAM method requires that the transitions used for a single measurement have to be from the same species, to ensure that all transitions originate in the same cloud with the same physical effects and the same velocity profile, avoiding contamination from other sources. The most famous species to do that is the FeII because its different transitions have positive and negative q, that are frequently detected in the observed QSO spectra.

Each species and each ionization transition have a particular signature, not only associated with the wavelength and q coefficient, but with its isotopic/hyperfine structure. In Murphy & Berengut (2014) the structure of each transition was discussed in detail and a study of the changes in the structures of the transitions due to assuming the solar abundances in the measurements presented. They point out that the MgII, AlII and MnII present the highest and significant systematic effect when the isotopic structure is ignored.

The Measurements Today

The best measurements of α in QSO spectra existing today were obtained with two high-resolution spectrographs: UVES - Ultraviolet and Visual Echelle Spectrograph, an instrument of the VLT- Very Large Telescope; HIRES - High Resolution Echelle Spectrometer, an instrument of the Keck observatory.

Quasar spectra obtained using these two separate observatories show a spatial variation in the relative spacings of absorption lines which could be due to an as yet undetected systematic

effect, or a dipole variation of α. (Webb et al. 2011) The fit to the dipole (in the direction Right Ascension: 17.5 ± 0.9 hours, Declination -58 ± 9 degrees.) has a statistical significance of 4.2σ. A variation at redshift $z \sim 2 - 3$, is also reported, with a relative variation at the level of a few parts per million. A detailed analysis of the data reduction, dipole computation and search for systematics is described in King's Ph.D. Thesis (2012).

The two data sets of UVES/VLT and HIRES/Keck with spectral data of QSO were reported in King's Ph.D. Thesis (2012) and in Murphy's Ph.D. Thesis (2002) respectively and are here presented in appendices C and D. These two datasets were compiled from gathered spectra observed with no specific purpose of testing for an α variation. Other sets of dedicated measurements have been reported, and with the purpose of gathering all the potential targets for future dedicated programs they are presented in table 2.1.

Table 2.1: List of dedicated measurements of the variation of α with UVES spectrograph. Column 1 gives the quasar name; the redshifts of the absorption system are given in Column 2; Column 3 the transitions used to do the measurement, presented as the code in B.1. Column 4 gives the value of measurement and the correspondent uncertainty. The last Column gives the references for each measurement.

Name	z_{abs}	Transitions	$\Delta\alpha/\alpha\,(10^{-5})$	Ref.
J000344−232355	0.4524	$b_1 b_2 j_5 j_6 j_8 a_2$	-0.963 ± 0.747	[1]
J000344−232355	2.1854	$b_1 b_2 j_4 j_5 j_6 e_1$	3.926 ± 2.431	[1]
J000344−232355	2.1872	$b_2 j_4 j_5 j_7 e_1$	-0.122 ± 0.774	[1]
J000448−415728	1.5419	$b_1 b_2 j_4 j_6 j_7 j_8$	-4.655 ± 0.988	[1]
J000448−415728	2.1679	$j_1 j_4 j_6 j_7 j_8 e_1$	0.115 ± 0.731	[1]
J000448−415728	2.3006	$j_4 j_6 e_1$	-0.075 ± 1.001	[1]
J011143−350300	1.1827	$b_1 b_2 j_4 j_6 j_8 a_2$	0.249 ± 0.764	[1]
J011143−350300	1.3489	$j_4 j_5 j_6 j_7 j_8 a_2 e_1$	-2.724 ± 1.144	[1]
J012417−374423	0.8221	$b_1 b_2 j_4 j_6 j_7 j_8 a_2$	1.062 ± 0.859	[1]
J012417−374423	0.8593	$b_1 b_2 j_6 j_7 j_8 a_2$	-4.803 ± 0.941	[1]
J012417−374423	1.2433	$b_1 b_2 j_4 j_5 j_6$	-2.447 ± 1.579	[1]
J024008−230915	1.6359	$b_1 b_2 j_4 j_7 j_8 e_1$	-0.124 ± 0.498	[1]
J024008−230915	1.6372	$b_1 b_2 j_1 j_4 j_7 j_8$	1.539 ± 0.939	[1]
J024008−230915	1.6574	$b_1 b_2 j_4 j_7 j_8$	0.510 ± 0.514	[1]
J045523−421617	0.9084	$b_1 b_2 j_4 j_6 j_8$	-1.507 ± 0.549	[1]
J045523−421617	1.8584	$b_1 b_2 j_4 j_6 j_8$	0.315 ± 0.712	[1]
J134427−103541	0.8728	$b_1 b_2 j_4 j_6 j_7$	-0.100 ± 0.567	[1]
J134427−103541	1.2767	$b_1 b_2 j_4 j_5 j_6 j_8$	0.524 ± 2.062	[1]
J134427−103541	1.9154	$j_1 j_4 j_5 j_6 j_8 e_1 e_2$	0.767 ± 0.627	[1]
J135038−251216	1.4393	$j_4 j_7 e_1 e_2$	-1.272 ± 0.767	[1]

Continued on next page

Table 2.1 – continued from previous page

Name	z_{abs}	Transitions	$\Delta\alpha/\alpha\,(10^{-5})$	Ref.
J212912−153841	2.0225	b_2e_1	-2.725 ± 1.344	[1]
J222006−280323	0.9425	$b_1b_2j_6j_8$	-1.453 ± 0.852	[1]
J222006−280323	1.5558	$b_1b_2j_4j_6j_7j_8e_1$	0.183 ± 0.639	[1]
HE 0515−4414	1.1508	$j_4j_5j_6j_7j_8$	0.05 ± 0.24	[2]
HE 2217−2818	1.6919	$c_1d_1d_2j_1j_5j_6$	0.13 ± 0.24	[3]
Q 1101−264	1.84	$j_1j_6j_8$	0.54 ± 0.25	[4]
HE 0515−4414	1.15	$j_1j_4j_5j_7$	-0.012 ± 0.179	[5]
Q 1101−264	1.84	$j_1j_6j_8$	0.566 ± 0.267	[5]
Q 1331+1704	1.776	$j_1j_5j_7$	0.590 ± 0.620	[5]
HE 1347−2457	1.439	$j_1j_4j_5$	-2.13 ± 0.36	[5]
HE 0001−2340	2.185	j_1j_6	2.32 ± 1.56	[5]
HE 0001−2340	2.185	$b_1b_2j_6$	0.32 ± 1.81	[5]
HE 0001−2340	2.187	$j_1j_4j_7$	2.08 ± 1.20	[5]
J1551+1911	1.143	$j_1j_4j_7$	0.880 ± 0.560	[6]
J1551+1911	1.342	$j_1j_4j_7$	0.002 ± 0.764	[6]
J1551+1911	1.802	$j_1j_4j_7$	0.066 ± 1.465	[6]

References: [1]-Chand et al. (2004) with corrections from Murphy et al. (2008) [2]-Chand et al. (2006), [3]-Bonifacio et al. (2014), [4]-Levshakov et al. (2007), [5]-Molaro et al. (2008), [6]-Evans et al. (2014)

In the work from Chand et al. (2005) other QSO spectral measurements of α were done using the AD method.

2.2 THE MEASUREMENTS TOMORROW - ESPRESSO AND ELT

In order to verify the claims of Webb et al. (2011) about a spatial variation of fine structure constant a confirmation of variability of α with high statistical significance is of crucial importance. Only a high-resolution spectrograph that combines a large collecting area with extreme wavelength precision can either improve the constrains on variations of fundamental constants or detect a non null result.

ESPRESSO is the next generation European exoplanet hunter, combining the efficiency of

Table 2.2: Summary of ESPRESSO's instrument modes and corresponding performance. Table from Pepe et al. (2013).

Parameter/Mode	singleHR (1 UT)	multiMR (up to 4 UTs)	singleUHR (1 UT)
Wavelength range	$380 - 780$ nm	$380 - 780$ nm	$380 - 780$ nm
Resolving power	134000	59000	225000
Aperture on sky	1.0 arcsec	4×1.0 arcsec	0.5 arcsec
Spectral sampling (average)	4.5 pixels	5.5 pixels (binned$\times 2$)	2.5 pixels
Spatial sampling per slice	9.0 (4.5) pixels	5.5 pixels (binned$\times 4$)	5.0 pixels
Simultaneous reference	Yes (no sky)	Yes (no sky)	Yes (no sky)
Sky subtraction	Yes (no simul. ref.)	Yes (no simul. ref.)	Yes (no simul. ref.)
Total efficiency	11%	11%	5%
Instrumental RV precision	$< 10cms^{-1}$	$10cms^{-1}$	$< 10cms^{-1}$

a modern echelle spectrograph with extreme radial velocity and spectroscopic precision, using wavelength calibration done with a Laser Frequency Comb. ESPRESSO will be installed in the Combined Coudé Laboratory of the VLT and linked to the four Unit Telescopes (UT) through optical coudé trains, operated either with a single UT or with up to four UTs for a 1.5 magnitude gain. The instrumental radial velocity precision will reach the $10cms^{-1}$ level and ESPRESSO will achieve a gain of two magnitudes with respect to its predecessor HARPS (High Accuracy Radial velocity Planet Searcher at the ESO La Silla telescope). This is the first VLT instrument using the incoherent combination of light from four telescopes and, together with the extreme precision requirements, calls for many innovative design solutions while ensuring the technical heritage of HARPS. (Pepe et al. 2013)

The specifications of ESPRESSO are presented in table 2.2 in each one of the three modes of operation.

The ESPRESSO Consortium is composed by teams of four countries (Switzerland, Italy, Spain and Portugal) and ESO itself. The consortium will be awarded Guaranteed Time Observations (GTO), eighty percent of these observing nights will be invested in the search for and characterisation of rocky planets in the habitable zone of G, K and M stars in the 1-UT mode. Ten percent of the time will be dedicated to the determination of the possible variability of the fundamental constants. Depending on the magnitude of the targets, this programme will be carried out partially in the 1-UT and 4-UT modes. The remaining ten percent of GTO time will be reserved for outstanding science cases and allocated as a function of topical questions arising at the moment

of the observations.(Pepe et al. 2013)

A relative variation in α or μ of 1 ppm leads to velocity shifts of about $20ms^{-1}$ between typical combinations of transitions. ESPRESSO is expected to provide an increase in the accuracy of the measurement of these two constants by at least one order of magnitude compared to VLT with UVES or Keck with HIRES. A schematic view of the improvements on the precision of the α of the next generation instruments is presented in fig. 2.2 taken from Maiolino et al. (2013).

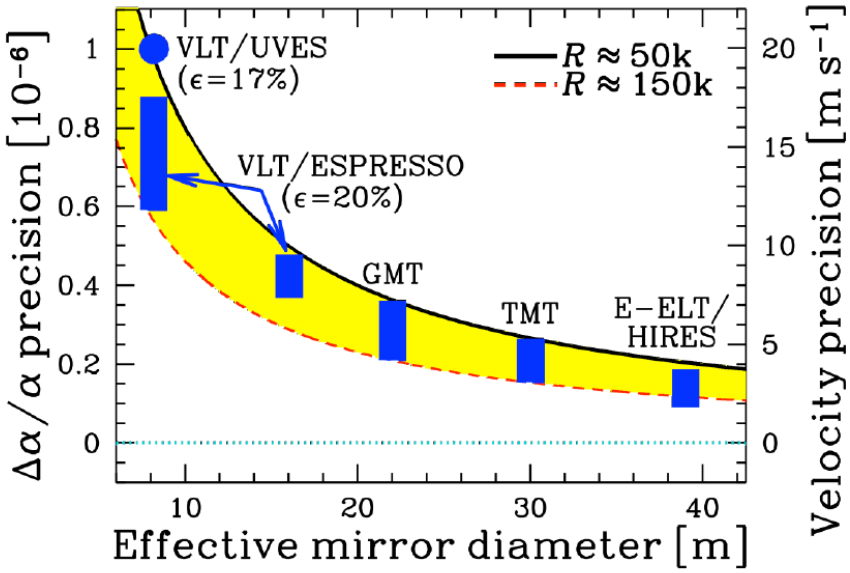

Figure 2.2: Expected statistical precision on variation in the fine-structure constant, $\Delta\alpha/\alpha$, achievable with future spectrographs as a function of telescope diameter. The equivalent velocity precision of the measurements is also shown (assuming a typical variety of metal-ion transitions). The length of the bars indicates the range of precision expected for different spectral resolutions available on those facilities. Two modes of operation for VLT/ESPRESSO are shown, its single-telescope mode (8-m effective diameter), with a range of resolving powers, and its anticipated four-telescope mode (16-m effective diameter), with R up to ≈ 70000. Figure from Maiolino et al. (2013).

One of the main aims of this work was to choose the target list for the purpose of testing the stability of fundamental constants for the ESPRESSO Consortium GTO. See section 3.2 in chapter 3.

One of the crucial limitations of ESPRESSO is the wavelength range, that is shorter than the ones of its predecessors (HARPS, UVES and Keck-HIRES). The effect of the shorter wavelength coverage of ESPRESSO versus a larger one from UVES is represented in figure 2.3. In the same figure it's shown the coverage in redshift of every common transition used to do measurements of the variation of α. It presents in blue the transitions that shift to blue and in red the opposite. It's a good tool for identifying the accessible redshift where the measurements can be preformed efficiently, this is, having a red and blue sensitive shifter and one anchor (transition less sensitive

to the α variations). In table 2.3 the range in redshift for measurements of the μ variation using H_2 molecules and for measurements of $T_{CMB}(z)$ with *CO*, taking into account the ESPRESSO and ELT-HIRES capabilities are presented.

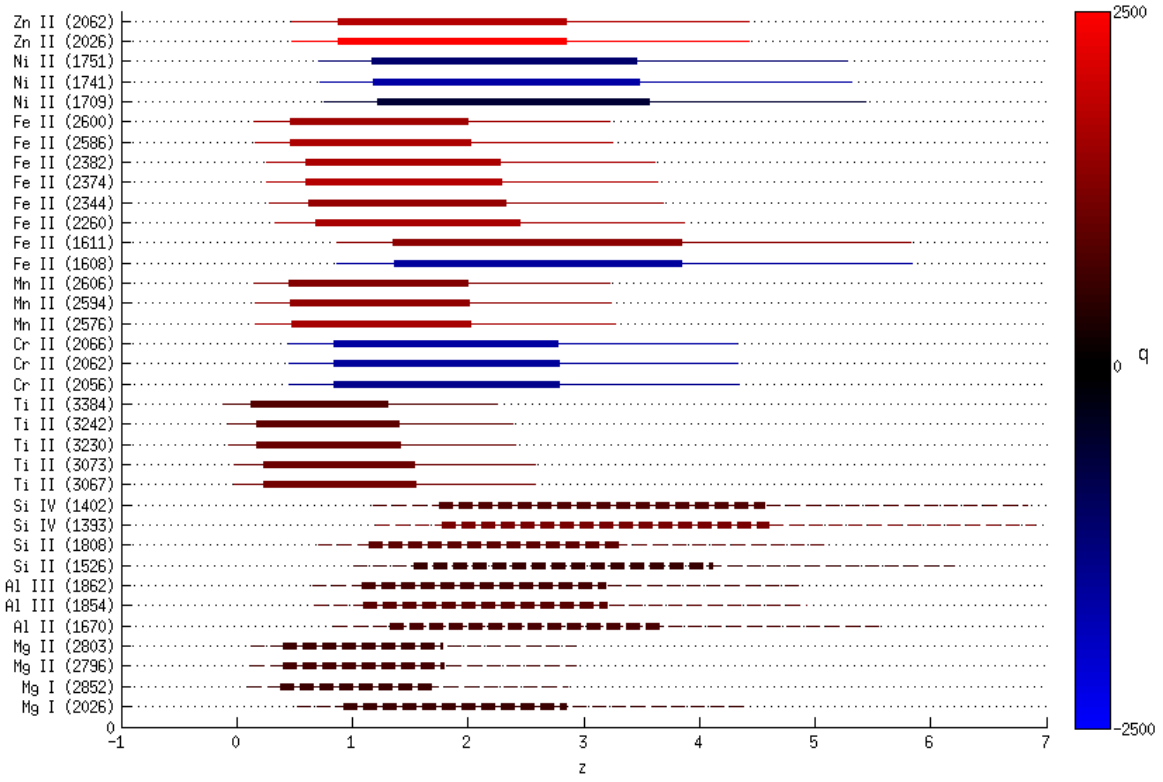

Figure 2.3: Redshift coverage of ESPRESSO and UVES of every common transition used to do measurements of the variation of α as indicated in B.1. Thinner part of the lines represent the coverage of UVES, the thicker part is representative of ESPRESSO. The colour code is indicative of the q sensitivity parameter, each transition has the colour cording to if they shift to the blue or red and by how much for an α variation. The dashed transitions correspond to *anchors*, transitions that don't shift much.

The High Resolution Spectrograph, HIRES, planed for E-ELT, will have a higher collecting power, which will lead to a higher signal-to-noise ratio (S/N) meaning that it will have the better chance of finding a new effect below the noise level of all other previous telescopes. See fig. 2.2. The wavelength coverage is expected to have a minimum about $330 - 370nm$ and a maximum $670 - 2400nm$, in the infrared, witch leads to an advantage over ESPRESSO concerning the IR coverage, which may allow precise measurements well beyond $z = 4$. The expectation for HIRES concerning the fundamental couplings observational programme will take into account ESPRESSO results. If ESPRESSO unambiguously confirms that α and/or μ vary, HIRES will be dedicated to map out the variation in redshifts and different environments; If no variations are

found, then the tighter bounds obtained can still be used to constrain the physics of the dark sector of the universe. (Liske et al. 2014)

Table 2.3: The potential coverage in redshift for ESPRESSO's(ESP) and HIRES/ELT's(HRS) measurements on μ, using H_2 molecules, and $T_{CMB}(z)$, using CO.

Molecule	Rest frame wavelength (Å)	ESP-z_{min}	ESP-z_{max}	HRS-z_{min}	HRS-z_{max}
H_2 (for μ)	$900 - 1150$	3.2	5.8	2.7	19.9
CO (for T_{CMB})	$1390 - 1550$	1.7	4.0	1.4	14.5

Chapter 3.

Observational Strategy

A fundamental step in order to improve the constrains on the variation of α, is not only to have better instrumentation but to understand how current datasets are limited. Studying previous data sets gives us information on the complexity of our target systems and not yet understood systematic effects.

A time normalization can in principle be derived from the present VLT performances, with the caveat that the present errors on α are dominated by systematics and not by photons. Nevertheless, we can assume a simple (idealized) observational formula,

$$\sigma^2_{sample} = \frac{C}{T}\,, \tag{3.1}$$

where C is a constant, T is the time of observation necessary to acquire a sample of spectra from which one will obtain N measurements of α at the relevant redshifts, and σ_{sample} is the relative uncertainty in the mean of the measurements (ie, the uncertainty in $\Delta\alpha/\alpha$) for the whole sample. This is expected to hold for a uniform sample, meaning a sample with N_α identical objects, each of which produces a measurement with the same uncertainty σ_α in a given observation time. Naturally any real-data sample will not be uniform, so there will be some corrections to this behaviour. The uncertainty of the sample will be given by

$$\sigma^2_{sample} = \frac{1}{\sum_{i=1}^{N} \sigma_i^{-2}}\,, \tag{3.2}$$

and for the above simulated case with N measurements all with the same α uncertainty we simply

have

$$\sigma^2_{sample} = \frac{\sigma^2_\alpha}{N} \,. \tag{3.3}$$

Clearly there are also other relevant observational factors that a simple formula like this does not take into account, in particular the structure of the absorber (the number and strength of the components, and how narrow they are) and the position of the lines in the CCD, which is connected to the redshift of the absorption system. The latter is also related to the wavelength range covered by each spectrograph. A further issue (which is easier to deal with) is the fact that a given line of sight often has several absorption systems, and thus yields several different measurements. Despite these caveats, this formula is adequate for this work's purposes, as will be further discussed.

3.1 UVES SAMPLE ANALYSIS

We have used the UVES data from (King's Ph.D. Thesis 2012), presented in table C.1 in appendix C, complemented by information on the observation time spent in each measurement provided by Murphy (private communication), to build a sample to calibrate the observational formula (3.1). In addition to these properties of the dataset, we also calculated the signal to noise per pixel with the following equation, parametrized by Michael Murphy using specifications of the UVES spectrograph:

$$SNR = K \left[\frac{T}{T_0} 10^{-0.4(M-M_0)} \right]^{1/2} \tag{3.4}$$

where T is the exposition time, M is the magnitude of the source and for $K = 20$, $T_0 = 3600s$ and $M_0 = 17.8$. However, note that this SNR is calculated for illustration purposes only, and is not used in our fitting analysis.

Figs. 3.1, 3.2 and 3.3 display some relevant properties of this set of absorption systems,

including the magnitude of the quasar, the redshift of the absorber, the observation time and the SNR of the spectrum. In all cases the circles denote the absorbers that lead to measurements with better than 10 parts per million statistical uncertainty, whereas crosses depict the rest of the absorbers. Note that several lines of sight contain multiple absorption systems, which is why several circles and crosses overlap in the magnitude-time panel of Fig. 3.1.

It is clear that this sample is far form ideal, as it does not display the types of correlations that one would expect from such a sample: better SNR or observation time do not necessarily lead to a better measurement of α. Undoubtedly this is a consequence of having a dataset put together from archival data. We did find the obvious correlation between SNR and the magnitude of the quasar (bottom panel of Fig. 3.1). Fig. 3.3 shows that higher redshift absorbers lead to proportionally better measurements. Moreover, in low-redshift absorbers brighter systems tend to give better measurements, while for higher redshift ones fainter systems can still yield good measurements. The reason for these differences stems form the different transitions available within the range of the spectrograph at the various redshifts.

We did find a strong correlation between the number of transitions used to make one measurement (N_λ) and the statistical uncertainty of the measurement, as can be observed in Fig. 3.4 where, for each N_λ, we plot the average uncertainty in the α measurements, $\sigma_{\Delta\alpha/\alpha}$, achieved as a function of that number of transitions. (Note that these transitions need not be the same is the various cases being averaged over.) We find that a simple parametrization shows the following approximate relation

$$\sigma_{\Delta\alpha/\alpha} = 139 N_\lambda^{-1.11}\,\mathrm{ppm}, \tag{3.5}$$

where again we expressed the uncertainty in parts per million. This best-fit parametrization is also plotted in Fig. 3.4.

In passing, we note that there is also a correlation between the sensitivity of the measurements and the (absolute) value of the q-coefficients of the transitions being used. This is unsurprising: transitions that shift the most for a given shift in α tend to yield better measurements. However, we shall not quantify this correlation, since it does not directly impact the phenomenological

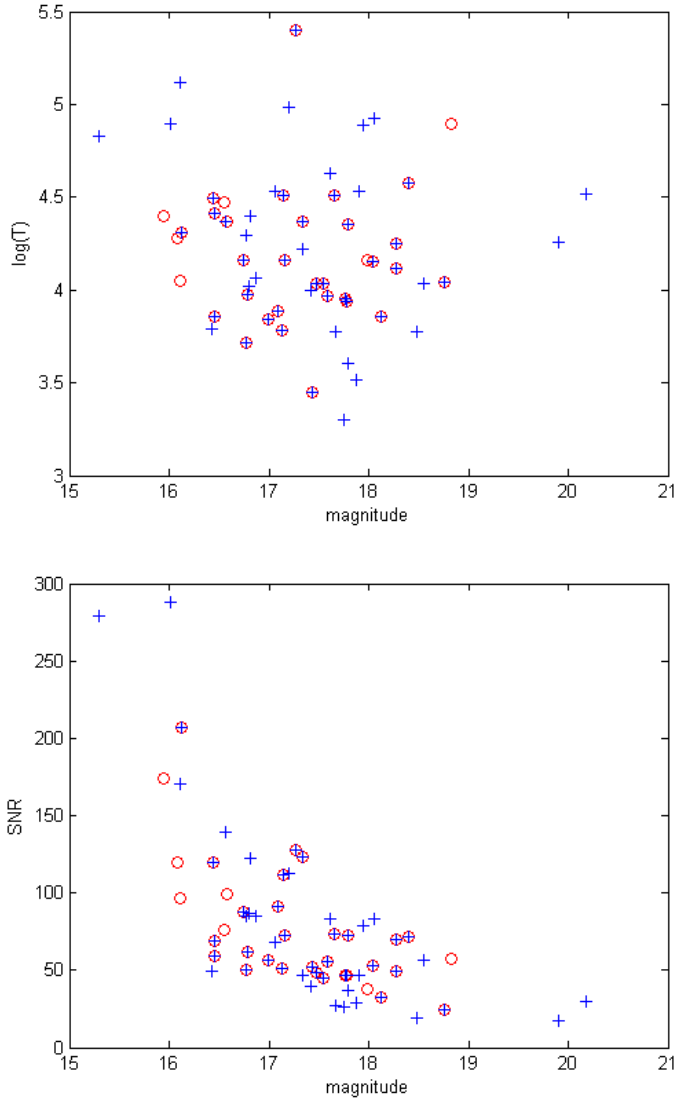

Figure 3.1: Observation time and SNR for the VLT absorbers of King's Ph.D. Thesis (2012), as a function of the quasar magnitude. Circles denote absorbers yielding measurements with better than 10 ppm statistical uncertainty, crosses denote the rest of the absorbers.

modelling of this work.

One consequence of these non-ideal properties of the sample is that the simple relation given by Eq. (3.1) will not strictly hold. Nevertheless, there is a simple way to correct it, which consists of allowing the former constant C to itself depend on the number of sources. This is easy to understand: in a small sample one typically will have the best available sources; by increasing our sample we will be adding sources which are not as good as the previous ones, and therefore the overall uncertainty in the α measurement will improve more slowly than in the ideal case—or alternatively one will need additional telescope time to do so.

Using standard Monte Carlo techniques we have generated several tens of thousands of sub-

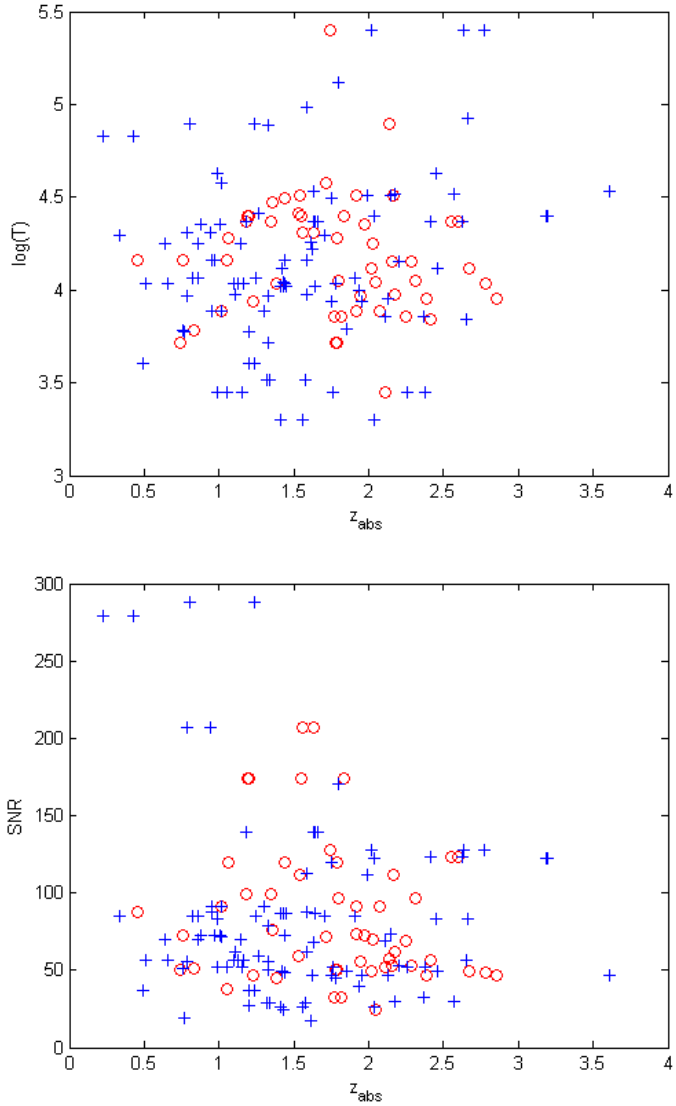

Figure 3.2: Observation time and SNR for the VLT absorbers of King's Ph.D. Thesis (2012), as a function of the redshift of the absorption system. Circles denote absorbers yielding measurements with better than 10 ppm statistical uncertainty, crosses denote the rest of the absorbers.

samples of the VLT sample, with various numbers of absorbers sources, for which we determined the overall uncertainty in the α measurement and the amount of telescope time needed to achieve it. From these distributions (an example of which, for the case $N = 20$, is shown in the top panel of Fig. 3.5) one can determine the corresponding mean values, and these then allow us to infer the behaviour for the empirical function $C(N)$. The results of this analysis are shown in Fig. 3.5. We find that a good fit is provided by the linear relation

$$C(N_\alpha) = 0.31\, N_\alpha + 5.02\,. \tag{3.6}$$

Here the constant has been normalised such that σ_{sample} is given in *parts per million* and T

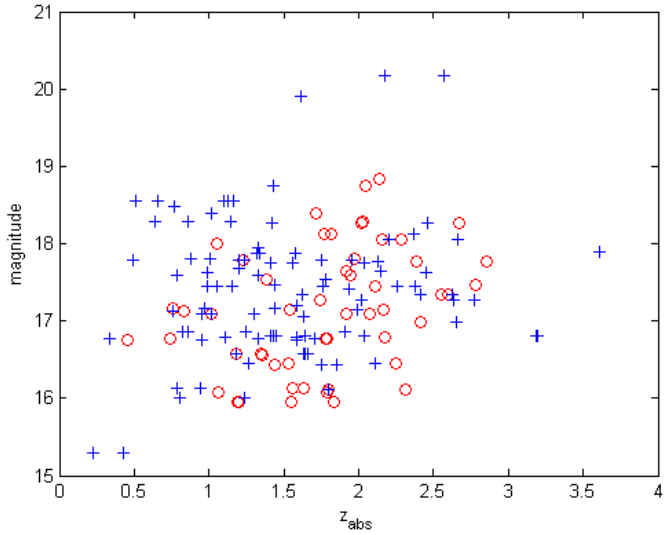

Figure 3.3: Uncertainty in the α measurements for the VLT absorbers of King's Ph.D. Thesis (2012), as a function of the magnitude of the quasar and the redshift of the absorbers. Circles denote absorbers yielding measurements with better than 10 ppm statistical uncertainty, crosses denote the rest of the absorbers.

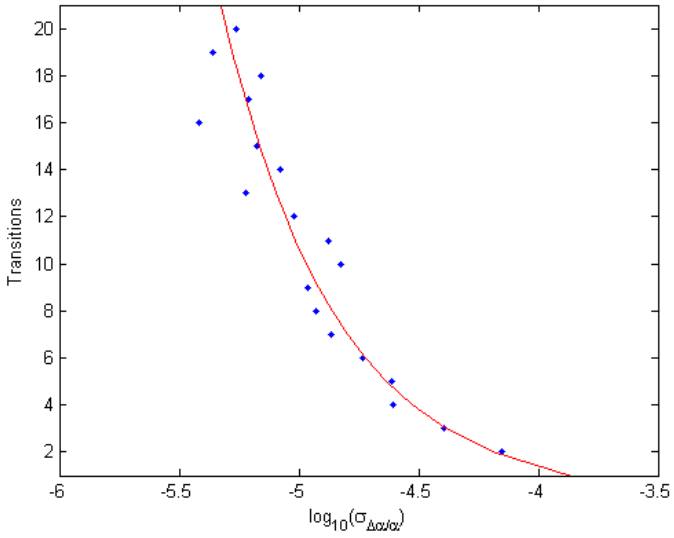

Figure 3.4: Correlation between statistical uncertainty of each of the α measurements and the number of transitions used to obtain them. Each point in the plot was obtained as an average of the various points in the dataset with each number of transitions used. The red line is the best power law, discussed in the text.

is in *nights*. As a simple check, for the UVES Large Program for Testing Fundamental Physics (Molaro et al. 2013, Rahmani et al. 2013), with about 40 nights and 16 sources, we infer from the fitting formula a value of 0.5 parts per million, consistent with the expectations of the collaboration (Bonifacio et al. 2014).

For future observational strategies implementations we can define:

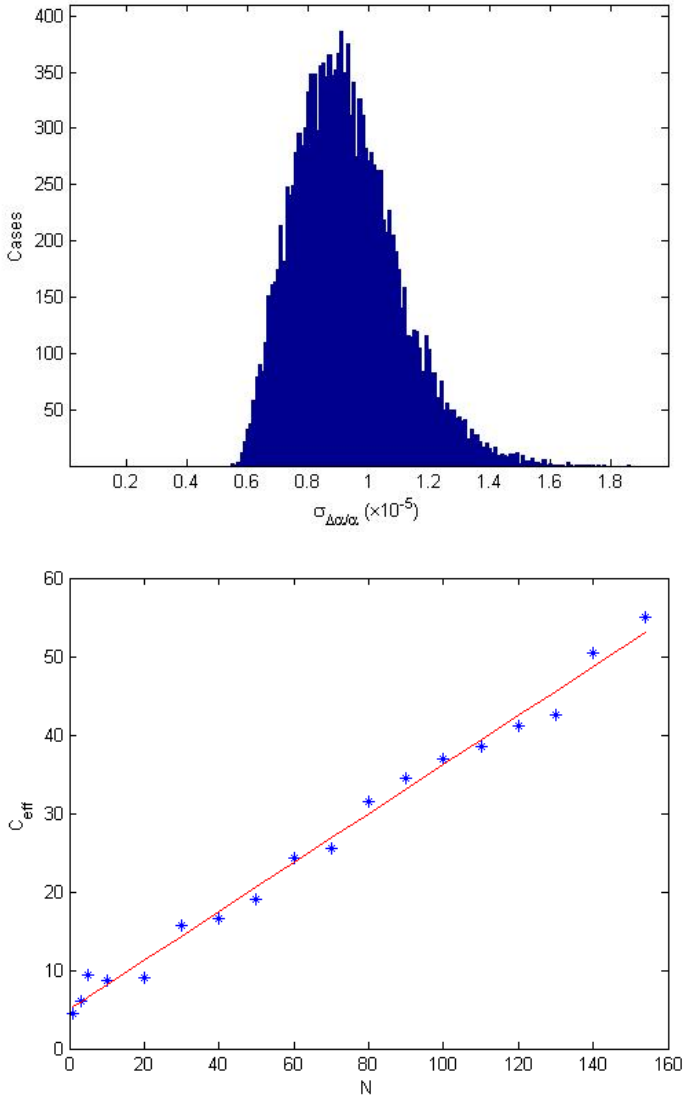

Figure 3.5: Top: Distribution of uncertainties in α for 20-source VLT subsamples, for a total of 15000 realizations. Bottom: Values of the effective parameter C as a function of the number of systems considered, for the parametrisation of the observational formula applied to the current UVES data. The red line is the best linear fit, discussed in the text.

- A baseline scenario, where there are essentially no improvements over UVES, that is

$$C(N_\alpha)_{BASE} = 0.31\, N_\alpha + 5.02\,; \tag{3.7}$$

this reflects the current situation, and therefore provides a benchmark against which future improvements can be discussed. Note that although this phenomenological fitting formula was obtained for UVES at the VLT, we expect it to also apply—at least qualitatively—to analogous contemporary spectrographs on other 8-meter class telescopes, such as HIRES-Keck or HDS-Subaru,

- An ESPRESSO scenario, where

$$C(N_\alpha)_{ESPRESSO} = \frac{5.02}{9}\,; \tag{3.8}$$

given realistic estimates of the available time (note that 27 GTO nights are foreseen) the observable samples are small enough to make a factor of 3 gain (on average) in sensitivity due to improved signal-to-noise and resolution, while eliminating the explicit dependence of C on the number of sources. These improvements arise from the fact that it will be, by design (Pepe et al. 2013), free of the systematics that are known to affect UVES, and in particular to the much more precise wavelength calibration, which will be done with a Laser Frequency Comb. Note that ESPRESSO does have a wavelength coverage that is substantially reduced compared to that of UVES, and this will certainly offset some of the above improvements.

- An ELT-HIRES scenario, where

$$C(N_\alpha)_{HIRES} = \frac{5.02}{300}\,; \tag{3.9}$$

here we similarly expect a constant C parameter (even allowing for the larger number of absorbers measured), and further gains in sensitivity have been factored in, including the five-fold increase in the telescope collecting area. Another key advantage of ELT-HIRES is its wide wavelength coverage, not only in the ultraviolet and optical but also in the infrared, as already pointed out in the previous section 2.2.

Finally, if we add a "systematics" term σ^2_{sys} to Eq. (3.1) and repeat the above procedure, the new parametrization indicates that values

$$\sigma_{sys} \sim 4 - 6\,ppm \tag{3.10}$$

provide a reasonable fit. It is interesting to note that this is not too distant from the value obtained in Webb et al. (2011), King's Ph.D. Thesis (2012),

$$\sigma_{Webb} = 9\,ppm\,; \tag{3.11}$$

naturally, their value was obtained with a much more sophisticated analysis. Nevertheless, this suggests that our simple toy modelling does capture the salient broad features of the datasets.

3.2 TARGET SELECTION

In the Guaranteed Time of Observation (GTO) of the ESPRESSO Consortium a limited time will be dedicated to test the stability of the fundamental constants. The primary goal will consist of establishing whether present hints of variability for α and μ are real or not. The goal is to reach 1 ppm accuracy, per target, or better, for both the constants. The new observations will either confirm the claimed variability or will place more stringent and robust bounds.

ESPRESSO will be able to operate in both the 1UT and 4UT modes. The 1 UT will be used to achieve the highest accuracy measurements by using the brightest suitable sources while leaving the 4UT mode to perform somewhat less accurate measurements but at slightly higher redshift.

In here I will focus mainly on the α target selection. The targets have to be selected from the whole known sample of absorbing systems (Tables: C.1, D.1, 2.1) that are reachable from the VLT site in Paranal. In Figure 3.6 the three datasets are represented and the measurements that have transitions outside the wavelegth range of the ESPRESSO are represented by red stars.

A list of criteria can be used to prioritize systems:

- QSO availability (Declination$< 30°$);
- QSO brightness;
- Number of transitions available in the system;
- A large Δq - Presence of positive and a negative sensitive transition;
- System with low temperature lines (narrow lines);
- System with strong but not saturated lines;
- Number of components forming the absorption system (low number means simpler cloud velocity structure);
- Systems with more than one anchor transition;

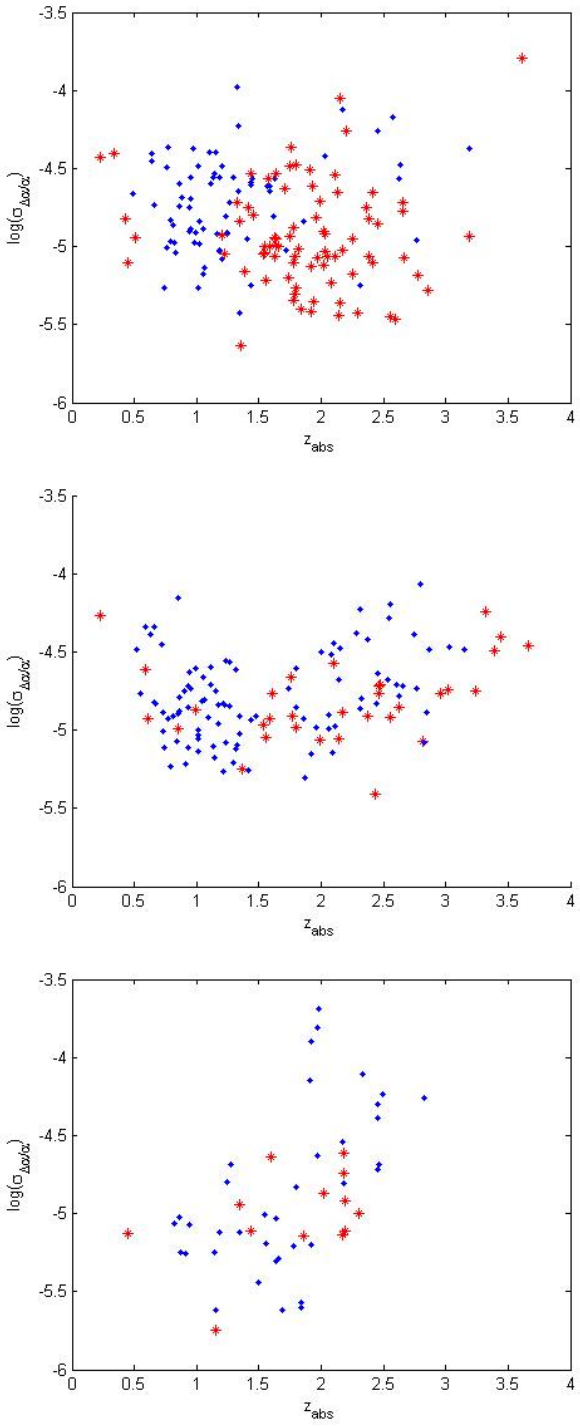

Figure 3.6: Uncertainty and redshift of absorption of the measurements distribution. The red stars represent measurements that rely on transitions outside of the ESPRESSO range, whilst the blue dots keep all information. From top to bottom: Dataset of UVES, Table C.1; Dataset of Keck, Table D.1; Dataset of the dedicated variation of α measurements, Table 2.1.

- Systems where the SIDAM method can be used;
- Ideal testers for the dipole model.

A good first indicator that a system is promising to perform a variation of α measurement is

that previous measurements of that system have achieved lower uncertainties, this means that the system should have several desirable features.

A sub-sample of the whole sample was built selecting the data with uncertainty lower than 5ppm. This sub-sample is based on a parameter that, for ESPRESSO, can be improved by the gains in resolution, but also deteriorated by the wavelength coverage compared with the spectrographs that made the measurements of the datasets.

Taking this into consideration, the automated part of the target selection needs to be based on an extra parameter Δq of the measurements. This parameter was adapted to ESPRESSO wavelength coverage. After a fine-tuning (to be explained bellow) in order to get a Target List with the best 10-15 systems, the measurements with uncertainty under 5ppm and a corrected Δq higher than 2000 were considered. The Target List is presented with details in Table 3.1, information is presented on: redshift; magnitude; values of the measurement; corrected Δq; details of the transitions available in the spectra for the ESPRESSO coverage range; and other measurements available in the same QSO target.

A division in four right ascension (RA) sectors was made to facilitate the prioritization of targets correlated with the time allocation that will be given to the GTO. In Table 3.1 this is represented by the lines separation.

The first system presented in Table 3.1 doesn't fulfil the uncertainty and Δq requirements, but is a system where μ and T_{CMB} measurements can also be made. This fact makes this an interesting target to investigate the nature of the fundamental constants variation testing different theories where a relation between these three constants are predicted. (Ferreira et al. 2014)

Note that the measured values of $\Delta\alpha/\alpha$ of the Table 3.1 are not consistent with the dipole predictions, which can be one more indicator that the systematics of the samples are currently not controlled.

Table 3.1: List of the best measurements of the variation of the fine structure constant considering the wavelength coverage of ESPRESSO. Column 1 gives the quasar name; the redshifts of the absorption system are given in Column 2; Column 3 gives the magnitudes of the emitting quasars. Column 4 and 5 give the value of measurement and the correspondent uncertainty. Column 6 gives the dipole model prediction from Webb et al. (2011) for the variation of α. Column 7 gives the ranges of sensitivity coefficients associated to the transitions of the absorption systems. Column 8 gives the number of transitions in each absorption system and Column 9 the elements that can be detected, colored differently if they are an anchor (black), a blue shifter (blue) and a red shifter (red). Column 10 gives the number of different α absorption systems measured so far in the line of sight of the QSO. Columns 11 and 12 indicate if there's a measurement of the variation of μ and/or T_{CMB}, respectively in the absorption system. The last Column gives the references for each measurement.

Name	z_{abs}	M	$\frac{\Delta\alpha}{\alpha}$ (10^{-6})	$\sigma_{\frac{\Delta\alpha}{\alpha}}(10^{-6})$	$\frac{\Delta\alpha}{\alpha}_{dip.}(10^{-6})$	Δq	# trans.	trans.	α syst	μ	T	Ref.
J034943-381031	3.02	17.3	-27.9	34.2	0.2	1350	2	SiII,FeII	1	x	x	[1]
J040718-441013	2.59	17.3	5.7	3.4*	0.9	2984	13	AlII,AlIII,SiII,CrII,FeII,FeII,NiII,ZnII	4	x'		[2]
J043037-485523	1.35	16.5	-4.0	2.3*	1.6	2990	17	MgI,AlII,SiII,CrII,MnII,FeII,NiII	1			[2]
J053007-250329	2.14	18.8	6.7	3.5*	-2.5	2990	7	AlII,CrII,FeII,FeII,NiII	1	x'		[2]
J110325-264515	1.84	15.9	6.1	3.9*	1.7	2890	4	SiII,FeII,FeII	4			[2]
J110325-264515	1.84	15.9	5.6	2.6	1.7	2760	3	FeII,FeII	4			[3]
J115944+011206	1.94	17.5	5.1	4.4*	-1.6	2990	12	SiII,CrII,MnII,FeII,FeII,NiII	3			[2]
J133335+164903	1.77	16.7	8.4	4.4	-1.9	2990	15	MgII,AlII,SiII,CrII,MnII,FeII,FeII,NiII,ZnII	4			[2]
HE1347-2457	1.43	16.3	-21.3	3.6	4.1	2790	3	FeII,FeII	1			[3]
J220852-194359	1.92	17.0	8.5	3.8	2.4	3879	16	AlII,SiII,CrII,MnII,FeII,FeII,NiII,ZnII	7			[2]
HE2217-2818	1.69	16.0	1.3	2.4	3.4	2890	6	AlIII,FeII,FeII	1			[4]
Q2230+0232	1.86	18.0	-9.9	4.9	-0.9	3879	14	SiII,CrII,FeII,FeII,NiII,ZnII	2			[1]
J233446-090812	2.15	18.0	5.2	4.3*	-0.5	3879	16	AlIII,CrII,FeII,FeII,NiII,ZnII	3			[2]
J233446-090812	2.28	18.0	7.5	3.7*	-0.5	2610	7	SiIV,CrII,FeII,FeII,NiII	3			[2]
Q2343+1232	2.43	17.5	-12.2	3.8*	-3.8	3879	11	AlII,SiII,CrII,FeII NiII,ZnII	4			[1]

* Measurements that lost transitions due to the wavelength range of ESPRESSO

' Measurements outside of the wavelength range of ESPRESSO

References: [1] - Murphy's Ph.D. Thesis (2002), [2] - King's Ph.D. Thesis (2012), [3] - Molaro et al. (2008), [4] - Bonifacio et al. (2014)

For the ultra-high resolution mode of observations with ESPRESSO (singleUHR in table 2.2) the preferred targets would be the ones with higher brightness. From the whole known sample of absorbing systems (Tables: C.1, D.1, 2.1) that are reachable from VLT, the systems from QSOs brighter than magnitude 16 were selected. In table 3.2 the measurements of the three QSOs with magnitude under 16 are presented as ideal targets for observations in this mode. Note that $J110325-264515$ is also in the ideal target list for ESPRESSO.

Table 3.2: List of measurements of the variation of the fine structure constant on QSO targets with magnitude less than 16, considering the wavelength coverage of ESPRESSO. Column 1 gives the quasar name; the redshifts of the absorption system are given in Column 2; Column 3 gives the magnitudes of the emitting quasars. Column 4 and 5 give the value of measurement and the correspondent uncertainty. Column 6 gives the ranges of sensitivity coefficients associated to the transitions of the absorption systems. Column 7 gives the number of transitions in each absorption system and Column 8 the elements that can be detected, colored differently if they are an anchor (black), a blue shifter (blue) and a red shifter (red). The last Column gives the references for each measurement.

Name	z_{abs}	M	$\frac{\Delta\alpha}{\alpha}$ (10^{-6})	$\sigma_{\frac{\Delta\alpha}{\alpha}}(10^{-6})$	Δq	# trans.	trans.	Ref.
HE0515-4414	0.22	15.3	12.6	37.0*	0	0	-	[1]
HE0515-4414	0.43	15.3	-31.5	15.0*	125	2	MgI, MgII	[1]
HE0515-4414	1.15	15.3	0.5	2.4	380	5	FeII	[2]
HE0515-4414	1.15	15.3	-0.1	1.8*	380	3	FeII	[3]
J110325-264515	1.19	15.9	-7.5	9.3	1504	8	MgI, MgII,FeII	[1]
J110325-264515	1.20	15.9	6.2	8.3	1370	6	MgII,FeII	[1]
J110325-264515	1.55	15.9	-6.7	10.0	1410	7	MgII,AlII,SiII,FeII	[1]
J110325-264515	1.84	15.9	6.1	3.9*	2890	4	SiII,FeII,FeII	[1]
J110325-264515	1.84	15.9	5.6	2.6	2760	3	FeII,FeII	[3]
HS1549+1919	1.14	15.8	8.8	5.6	1404	7	MgI, MgII,FeII	[4]
HS1549+1919	1.34	15.8	0.0	7.6	1504	8	MgI, MgII,FeII	[4]
HS1549+1919	1.80	15.8	6.6	14.7	1244	5	AlII,AlIII,FeII	[4]

* Measurements that lost transitions due to the wavelength range of ESPRESSO

References: [1] - King's Ph.D. Thesis (2012), [2] - Chand et al. (2006), [3] - Molaro et al. (2008), [4] - Evans et al. (2014)

The details on the μ targets are presented in Table 3.3. The $J034943-381031$ α target is also one of the two known measurements for μ in the wavelength range of ESPRESSO. Four extra targets where μ measurements can be preformed are presented in the second part of the table. Note that the magnitude of the extra targets is ~ 20. That may make them too faint to get the SNR necessary to perform a measurement.

Table 3.3: List of existing and possible measurements of the variation of proton to electron mass ratio for the wavelength coverage of ESPRESSO. All the measurements either have a measurement performed with transitions of H_2 or for the lower part of the table have a high column density of the same element. Column 1. gives the quasar name; the redshifts of the absorption system are given in Column 2.; Column 3. gives the magnitudes of the emitting quasars. Column 4. and 5. give the value of measurement and the correspondent uncertainty. Colums 6. and 7. indicate if there's a measurement of the variation of α and/or T_{CMB}, respectively in the absorption system. The last Column gives the references for each measurement.

Name	z_{abs}	M	$\frac{\Delta\mu}{\mu}$ (10^{-6})	$\sigma_{\frac{\Delta\mu}{\mu}}$ (10^{-6})	α	T	Ref.
J034943-381031	3.02	17.3	2.1	6.0	x	x	[5]
J1443+2724	4.22	19.3	-9.5	7.6			[6]
Q0201+113	3.39	19.5	-	-			[7]
J0816+1446	3.29	20.4	-	-			[8]
J1337+3152	3.17	19.0	-	-			[9]
J1456+1609	3.35	20.0	-	-			[10]

References: [5] - King et al. (2008); [6] - Ledoux et al. (2006); [7] - Guimarães et al. (2012);[8] - Noterdaeme et al. (2015); [9] - Srianand et al. (2012); [10] - Srianand et al. (2010).

The details on known measurements of the T_{CMB} that can be done within the ESPRESSO wavelength range are presented in Table 3.4.

Table 3.4: List of existing measurements of the T_{CMB} for the wavelength coverage of ESPRESSO. All the measurements either have a measurement performed with transitions of *CO*. Column 1. gives the quasar name; the redshifts of the absorption system are given in Column 2.; Column 3. gives the magnitudes of the emitting quasars. Column 4. and 5. give the value of measurement and the correspondent uncertainty. Columns 6. and 7. indicate if there's a measurement of the variation of α and/or μ, respectively in the absorption system. The last Column gives the references for each measurement.

Name	z_{abs}	M	T_{CMB} (K)	$\sigma_{T_{CMB}}$ (K)	α	μ	Ref.
J034943-381031	3.02	17.3	12.1	3.2	x	x	[11]
J085726+185524	1.72	17.4	7.5	1.6			[12]
J104705+205734	1.77	19.9	7.8	0.7			[12]
J123714+064759	2.69	19.2	10.5	0.8			[13]
J143912+111740	2.42	18.9	9.15	0.7		x'	[14]
J170542+354340	2.04	19.1	8.6	1.1			[12]

' Measurement outside of the wavelength range of ESPRESSO

References: [11] - Wendt & Reimers (2008); [12] - Noterdaeme et al. (2015); [13] - Noterdaeme et al. (2009); [14] - Srianand et al. (2008)

In order to build an observational strategy able to respond to the needs of the Consortium, the sky localization of each target has to be taken into account. Fig. 3.7 presents the information on Tables 3.1, 3.3 and 3.4, considering the coordinates of the targets and the redshift of the

sources. These plots facilitate a rapid visualization of the target position to test the dipole model, represented by the color map in the background, and the target distribution in redshift: 1.35 to 2.59 (3.02). In Figure 3.8 the details of the Figure 3.7 are presented, each line corresponding to a RA sector.

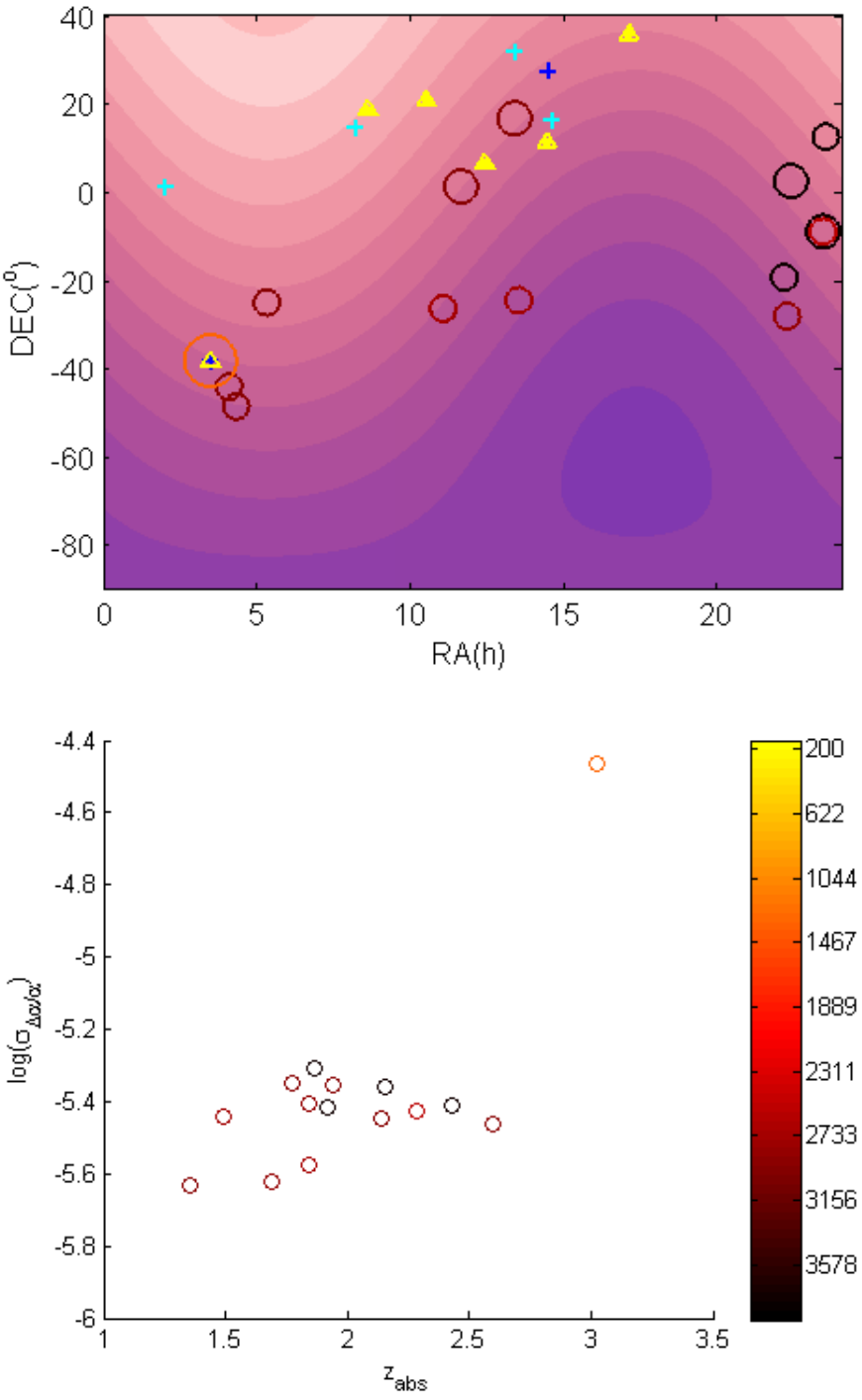

Figure 3.7: The Top figure shows the sky distribution for the list of the best measurement for ESPRESSO in Tables 1. 2. and 3. The circles represent the α measurements, their size is proportional to the uncertainty of the measurement and the color gives the value for Δq according to the color bar in the lower panel. The dark blue crosses represent the μ measurements, and cyan the possible targets of μ. The yellow triangle represents the T_{CMB} measurements. The color code behind the plot represents the dipole prediction for the values of α variation, with the purple representing a positive shift and the light pink a negative shift for the prediction. The Bottom figure represents the redshift and uncertainty for the α measurements, the color gives the value for Δq according to the values of the color bar.

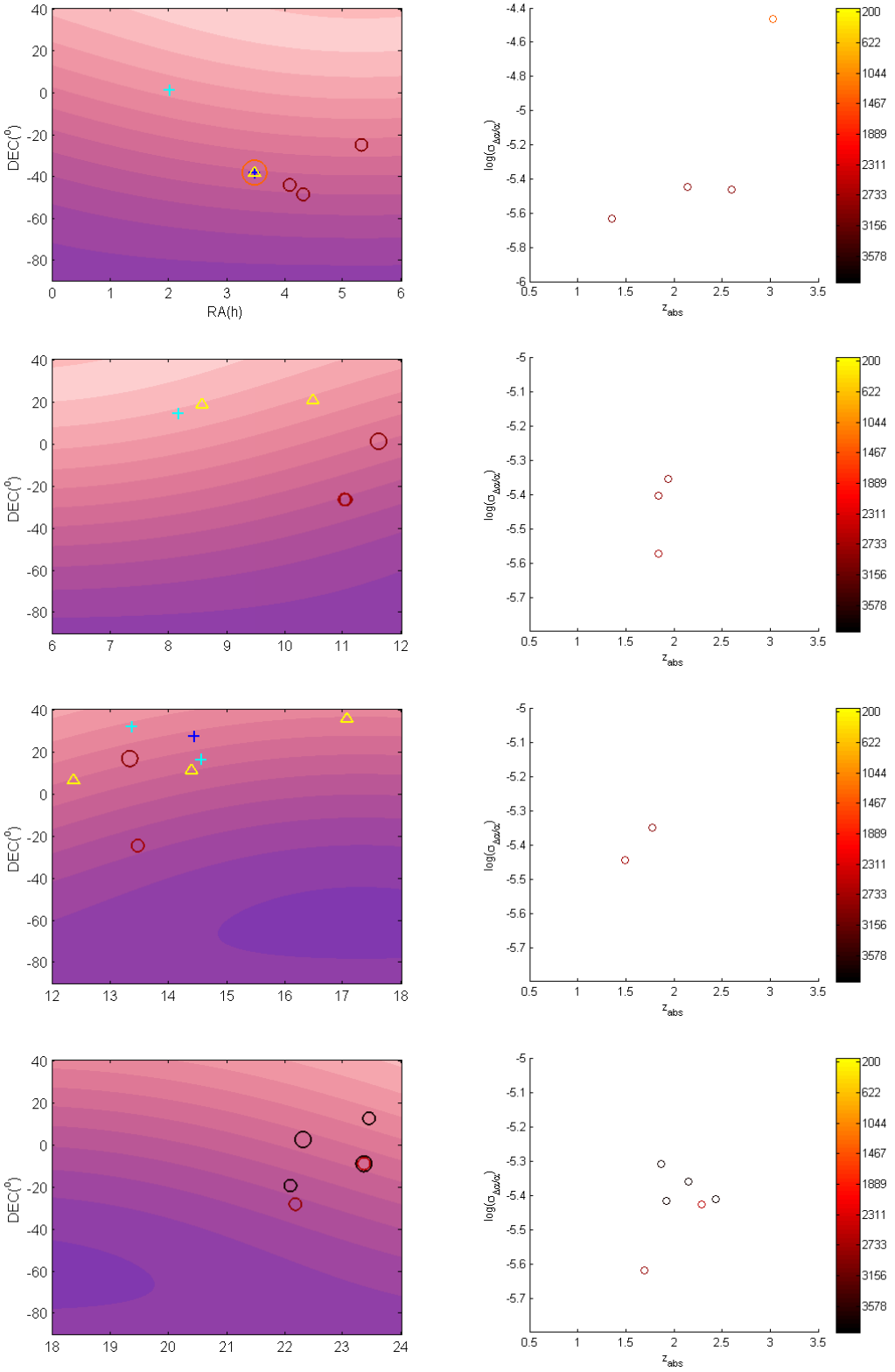

Figure 3.8: Panels on the left represent 4 separate sections (Right ascension: 0h to 6h; 6h to 12h; 12h to 18h; 18h to 24h) with the sky distribution for the list of the best targets for ESPRESSO in Tables 3.1, 3.3 and 3.4. The panels on the right represent the redshift and uncertainty for the α measurements corresponding to the panel on the left. The point and color representations are the same as Figure 3.7.

Comments on the Targets for ESPRESSO

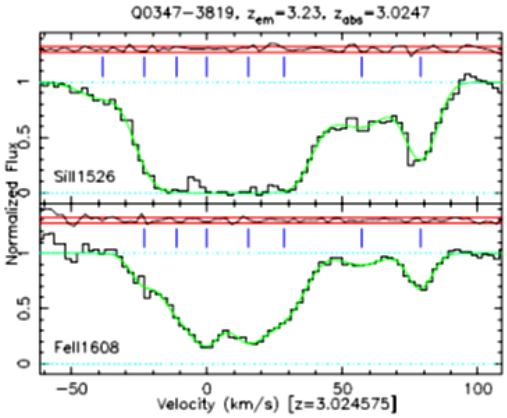

Figure 3.9: Spectra details from the QSO J034943-381031. Image from Murphy's Ph.D. Thesis (2002).

J034943-381031

This measurement did not pass the criteria in terms of Δq and uncertainty, but the same absorption system has μ and T_{CMB} measurements, that make this target an interesting target to constrain simultaneously three dimensionless parameters and test theories that predict their dependences at no more additional telescope time cost.

Only two transitions are available: one anchor that seems saturated (*SiII* 1526) and one blue shifter (*FeII* 1608). It's the measurement with the higher redshift from the list (3.02)

This measurement was preformed with Keck telescope but is achievable for the VLT, it should not give one of the better measurements when compared with the rest from the list.

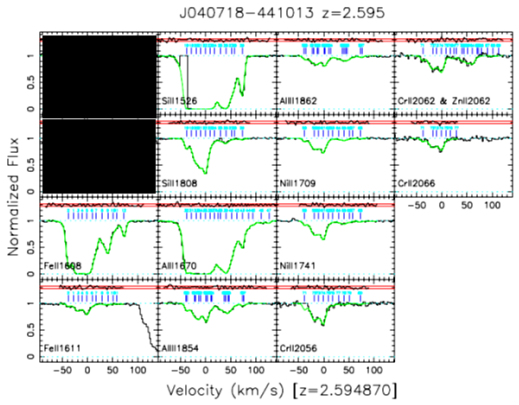

Figure 3.10: Spectra details from the QSO J040718-441013. Image from King's Ph.D. Thesis (2012). The black panels represent the transitions that can not be observed with ESPRESSO.

J040718-441013

This measurement, despite losing two transitions in the ESPRESSO wavelength range (*FeII* 2374 and 2586), still presents a high Δq and a high number of transitions available.

Two of the anchors are saturated (*SiII* 1526 and *AlII* 1670) but two non saturated anchors are still available. The measurement presents blue and red shifters, that are weak. Apart from the previous measurement this is highest redshift (2.59) from the target list.

The system presents a high number of components to the fitting procedure as can be seen on the figure by the blue stripes on top of each line.

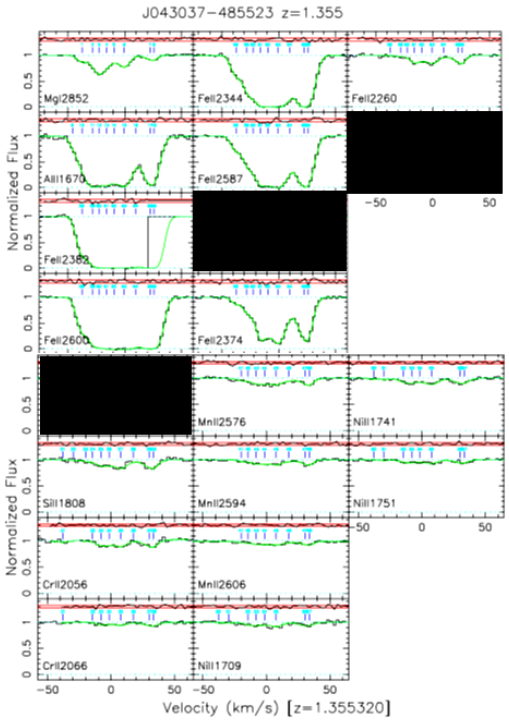

Figure 3.11: Spectra details from the QSO J043037-485523. Image from King's Ph.D. Thesis (2012). The black panels represent the transitions that can not be observed with ESPRESSO.

J043037-485523

This measurement loses three transitions in the ESPRESSO wavelength range (*FeII* 1608 1611, *SiII* 1526), and although it still presents a high Δq and a high number of transitions available, they appear either saturated or with very weak signal.

The lines that don't seem saturated and are stronger (example: *FeII* 2374) present large broadening.

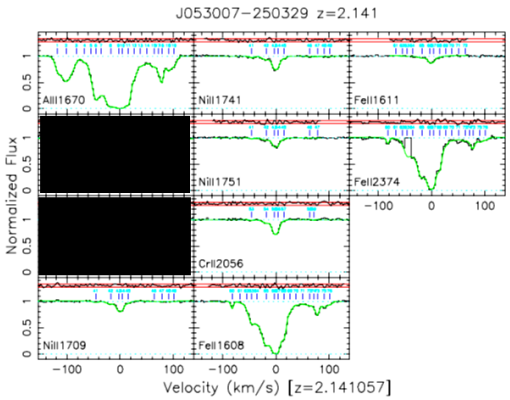

Figure 3.12: Spectra details from the QSO J053007-250329. Image from King's Ph.D. Thesis (2012). The black panels represent the transitions that can not be observed with ESPRESSO.

J053007-250329

This measurement loses two transitions in the ESPRESSO wavelength range (*MgII* 2796 and 2803), both of them are anchors, keeping only one anchor available (*AlII* 1670). This anchor appears slightly saturated.

The Δq is high and although some of the lines seem weaker we still have a blue (*FeII* 1608) and a red (*FeII* 2374) shifter with a stronger signal.

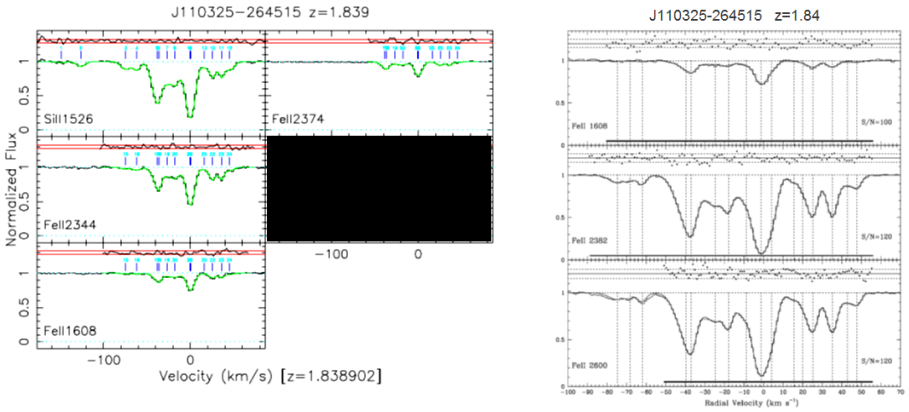

Figure 3.13: Spectra details from the QSO J110325-264515. Left image from King's Ph.D. Thesis (2012). Right image from Molaro et al. (2008). The black panel represents the transition that can not be observed with ESPRESSO.

J110325-264515 - Left image

The measurement loses one anchor transition (*MgI* 2852) in the ESPRESSO wavelength range.

The system still has available one anchor, a blue and two red shifters. The crucial blue shifter (*FeII* 1608) presents a weak signal.

The magnitude of the QSO is the lowest of the sample making it a good target for the single high resolution mode (1UT) mode or even the single ultra high resolution mode (1UT).

J110325-264515 - Right image

This target is the same as the previous one, and the same comment applies.

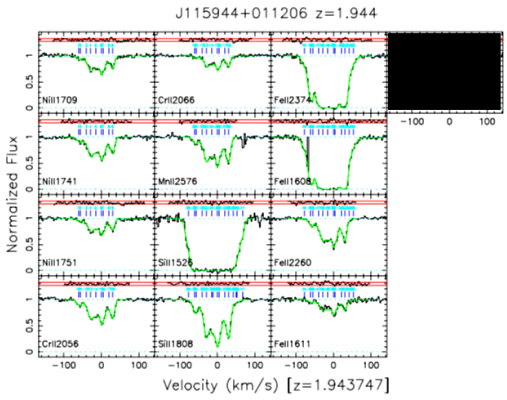

Figure 3.14: Spectra details from the QSO J115944+011206. Image from King's Ph.D. Thesis (2012). The black panel represents the transition that can not be observed with ESPRESSO.

J115944+011206

The target loses one anchor transition (*MgI* 2852) in the ESPRESSO wavelength range. The spectrum still has two more anchors (*SiII* 1526 1808). Three of the transitions are saturated (*SiII* 1526, *FeII* 2374, 1608), the last one of them is the most important blue shifter of the sample.

The spectrum is noisy, and presents a high number of components to produce the fit, as noted by the blue stripes above each transition.

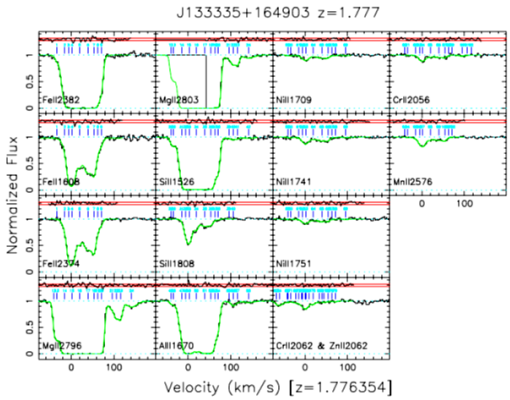

Figure 3.15: Spectra details from the QSO J133335+164903. Image from King's Ph.D. Thesis (2012). The black panel represent the transition that can not be observed with ESPRESSO.

J133335+164903

None of the transitions are lost. This fact denotes that the uncertainty of the measurement can only improve when performed with ESPRESSO.

Most of the anchor transitions are saturated (*MgII* 2796, 2803, *SiII* 1526, *AlII* 1670), but *SiII* 1808 is not. One of the *FeII* transitions is saturated, but blue and red shifters are still clear and available.

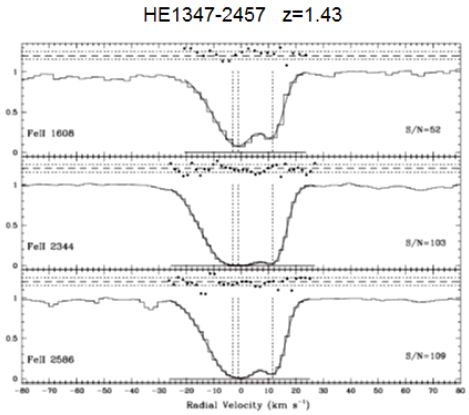

Figure 3.16: Spectra details from thee QSO HE1347-2457. Image from Molaro et al. (2008).

HE1347-2457

None of the transitions are lost. This fact denotes that the uncertainty of the measurement can only improve when performed with ESPRESSO.

The existing measurement was not preformed with the use of any anchor transition, and it was done with *FeII* transitions only (1608 blue shifter, 2344 and 2586 red shifters). Hence this is a target where a competitive SIDAM measurement can be preformed.

The prediction of the dipole model (Webb et al. 2011) for this target is the one with the largest positive deviation from the standard α.

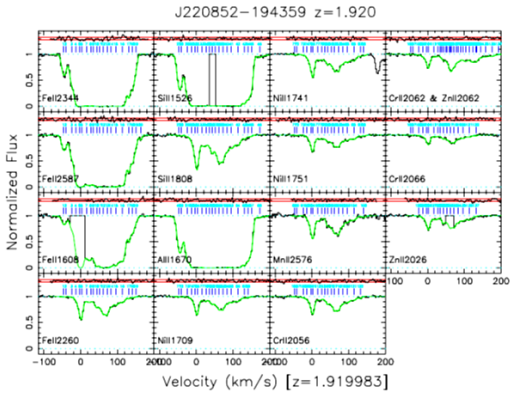

Figure 3.17: Spectra details from the J220852-194359. Image from King's Ph.D. Thesis (2012).

J220852-194359

None of the transitions are lost. This fact denotes that the uncertainty of the measurement can only improve when performed with ESPRESSO.

Two of the three anchor transitions are saturated (*SiII* 1526, *AlII* 1670). Most *FeII* transitions are saturated (the exception being *FeII* 2260), but transitions from other species as blue and red shifters are still clear and available. The spectrum requires a high number of components to produce the fit, as noted by the blue stripes above each transition.

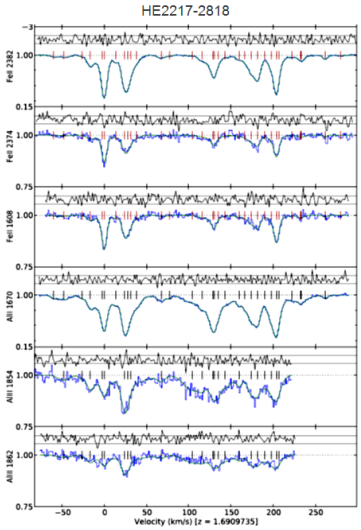

Figure 3.18: Spectra details from the HE2217-2818. Image from Bonifacio et al. (2014).

HE2217-2818

None of the transitions are lost. This fact denotes that the uncertainty of the measurement can only improve when performed with ESPRESSO. The lines are not saturated and the spectrum presents three *AlIII* anchors, and *FeII* blue and red shifters.

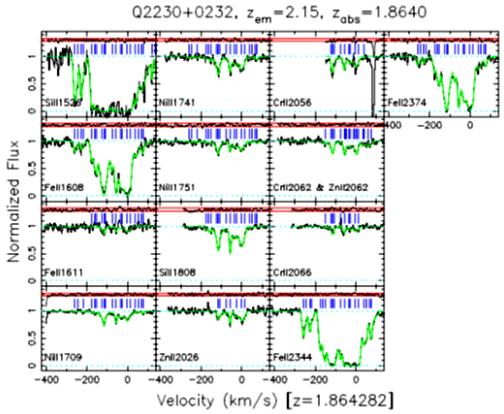

Figure 3.19: Spectra details from the QSO Q2230+0232. Image from Murphy's Ph.D. Thesis (2002).

Q2230+0232

None of the transitions are lost. This fact denotes that the uncertainty of the measurement can only improve when performed with ESPRESSO.

One of the two anchors available is saturated (*SiII* 1526).

The spectrum is noisy, and presents a high number of components to produce the fit, as noted by the blue stripes above each transition.

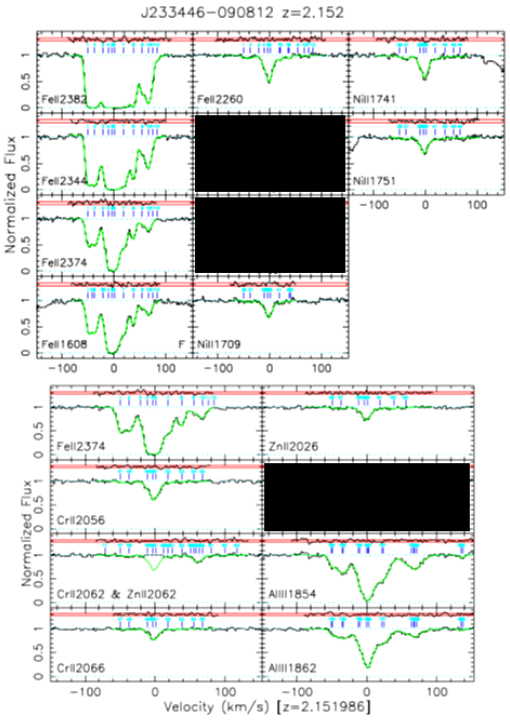

Figure 3.20: Spectra details from the QSO J233446-090812. Image from King's Ph.D. Thesis (2012). The black panel represent the transition that can not be observed with ESPRESSO.

J233446-090812 - $z_{abs} = 2.15$

The measurement loses two anchor transitions (*MgII* 2796 2803), and a red shifter (*MnII* 2576) in the ESPRESSO wavelength range. The spectrum still has two more anchors (*AlIII* 1854 1862).

Some of the *FeII* transitions are saturated. But this system is composed of a large number of measurements with blue and red shifts not displaying a high broadening.

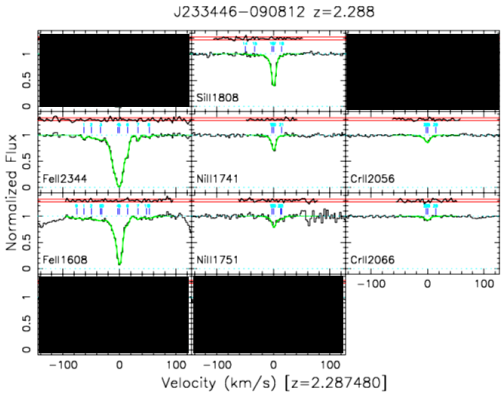

Figure 3.21: Spectra details from the QSO J233446-090812. Image from King's Ph.D. Thesis (2012). The black panel represent the transition that can not be observed with ESPRESSO.

J233446-090812 - $z_{abs} = 2.28$

The target is in the same QSO as the previous one at a different redshift. The spectrum of the system loses four red shifter transitions (*MnII* 2594 2606, *FeII* 2600 2374) in the ESPRESSO wavelength range.

In the spectrum we still have one anchor (*SiII* 1808), and blue and red shifters. The transitions don't show saturation.

Q2343+1232

The spectrum details of this target has not been published, so we don't have the details of these transitions. We know that the measurement loses three red shifter transitions (*FeII* 2600 2586 2344) in the ESPRESSO wavelength range.

The prediction of the dipole model (Webb et al. 2011) for this target is the one with the largest negative deviation from the standard α.

Chapter 4.

Forecasts for Dark Energy

4.1 PRINCIPAL COMPONENT ANALYSIS: REPRESENTATIVE SCENARIO RESULTS

When one needs to parametrize functions for which we have no prior knowledge, the function should be determined by the data rather than be influenced by our beliefs. With that in mind using Principal Component Analysis (PCA) allows us to constrain models of dark energy using different observables. A detailed description of PCA and how it works is presented in Appendix A.

We assume a class of models that allows "simple" relations between the variation of the fine-structure constant and the equation of state of the dark energy, Eq.(1.37). The class of models being considered for this study was presented in detail in 1.2.2.

Knowing the relation between the observable and the function to reconstruct, one can calculate the Fisher matrix using standard techniques, as discussed in Appendix A. Recall from subsection 1.2.2 the three fiducial equations of state:

$$\omega_c(z) = -0.9, \tag{4.1}$$

$$\omega_s(z) = -0.5 + 0.5\tanh\left(z - 1.5\right), \tag{4.2}$$

$$\omega_b(z) = -0.9 + 1.3\exp\left[-\tfrac{(z-1.5)^2}{0.1}\right]. \tag{4.3}$$

At a phenomenological level, these describe the three qualitatively different interesting scenarios as discussed in subsection 1.2.2. We will refer to them, in what follows, as the *constant*, *step* and *bump* fiducial models.

For the PCA analyses we assume a flat universe, and further simplify the analysis by fixing $\Omega_m = 0.3$. This specific choice of Ω_m has a negligible effect on the main result of the analysis, which is the uncertainty in the best determined modes. For each fiducial model we choose the coupling such that it leads to a few parts-per-million variation of α at redshift $z \sim 4$, consistently with Webb et al. (2011).

In Amendola et al. (2012) different datasets for alpha measurements were explored in combination with supernovae type Ia. For the fine-structure constant measurements we focused on the ESPRESSO spectrograph for the VLT and ELT-HIRES for the E-ELT; Specifically we consider the following two scenarios

- A **Baseline** scenario, in which we assumed measurements in 30 systems with uncertainty $\sigma_{\Delta\alpha/\alpha} = 6 \times 10^{-7}$ for ESPRESSO and 100 systems with $\sigma_{\Delta\alpha/\alpha} = 1 \times 10^{-7}$ for ELT-HIRES, uniformly distributed in the redshift range $0.5 < z < 4$. This is meant to represent what we can confidently expect to achieve from each spectrograph (e.g., from Guaranteed Time Observations), given their expected sensitivity, and it will therefore provide the basis for most of our discussion.

- An **Ideal** scenario, in which we assumed 100 systems with $\sigma_{\Delta\alpha/\alpha} = 2\times10^{-7}$ for ESPRESSO and 150 systems with $\sigma_{\Delta\alpha/\alpha} = 3 \times 10^{-8}$ for ELT-HIRES. This is optimistic both in the uncertainty of individual measurements and in the number of measurements. Putting together such a dataset would at the very least require a very long time and almost certainly a dedicated program. Our goal in considering this ideal case was to obtain an indication for the dependence of our results on the uncertainty and number of the measurements.

We are now in a position to start a forecast analysis of the dark energy equation of state for our three fiducial forms of $\omega^F(z)$. We take a total number of bins between redshift 0 and 4 to be 30. We assume a sample of 3000 supernovae distributed between redshift 0 and 1.7 (with 13 bins) with an uncertainty on the magnitude of $\sigma_m = 0.11$. These numbers are typical of future supernovae datasets. (Huterer and Starkman 2003)

The different fiducial model scenarios for α measurements in combination with the Supernovae dataset were tested in the two different truncation methods presented in Appendix A: Minimization of the risk method and Normalization of the error method. These truncation methods choose the

"ideal" number of components to keep in order to achieve a "better" reconstruction. More modes generally means higher error bars (less precise), which up to a certain point allows a better accuracy.

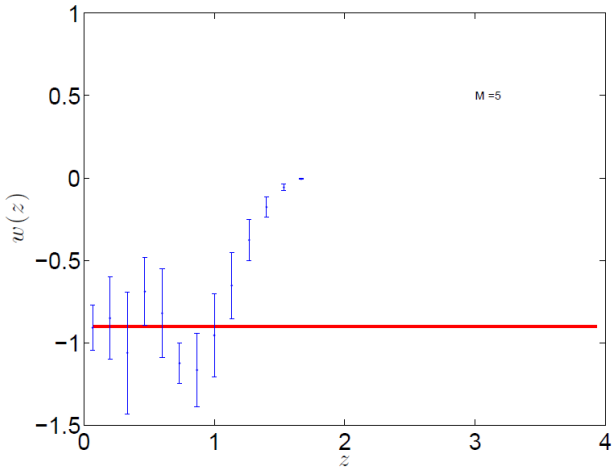

Figure 4.1: Reconstruction of the equation of state parameter using only supernovae with the minimization of the risk method. Here and in the following plots, M represent the number of PCA modes used in the reconstruction.

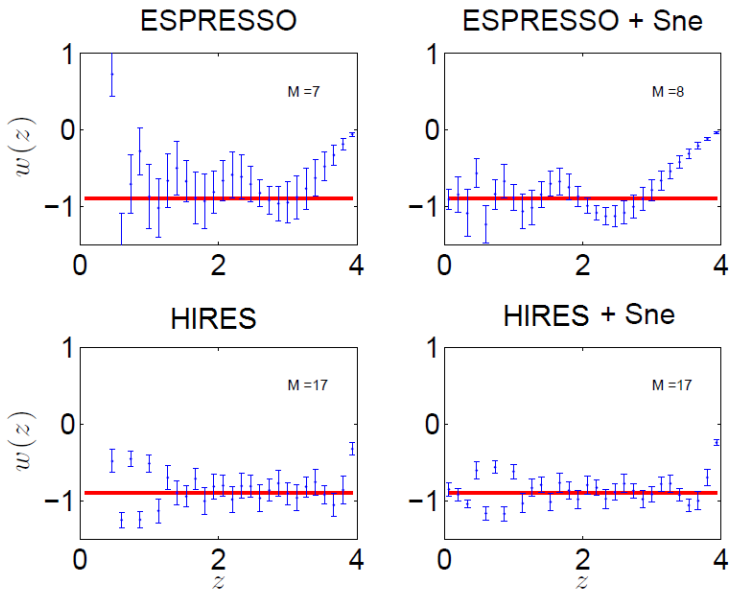

Figure 4.2: Reconstruction of the equation of state parameter in the baseline scenario with the minimization of the risk method, for a constant fiducial equation of state.

In Fig. 4.1 we illustrate the reconstruction using only supernovae for our fiducial model and in Figs. 4.2 and 4.3 we show the result of the reconstruction for the two spectrographs and the two methods for the selection of the number of components. We can observe that, for this fixed number of bins, the reconstruction obtained using supernovae is only accurate up to $z \sim 1$. In particular, because we neglect the poorly determined modes which are the ones with high

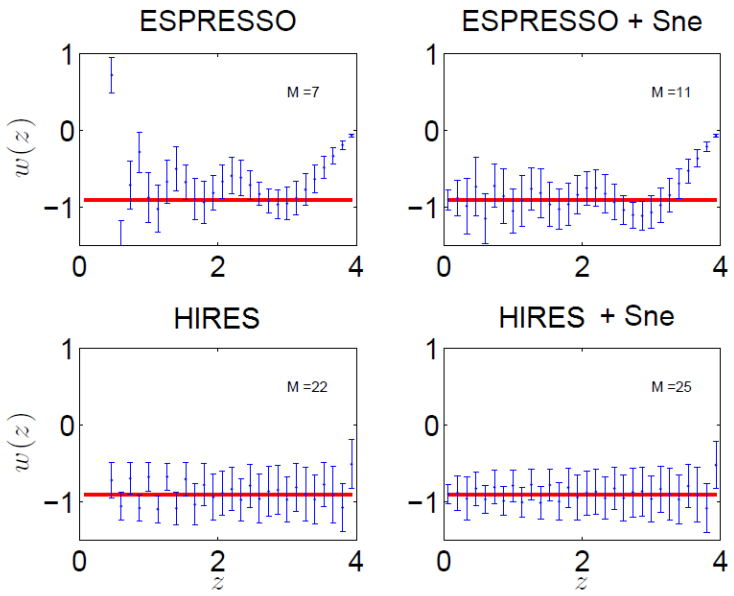

Figure 4.3: Reconstruction of the equation of state parameter in the baseline scenario with the normalization of the error on the modes method.

amplitudes for bins of large redshift, the reconstructed equation of state parameter tends to zero for large redshift. This unavoidable feature of the PCA truncation method can be confused with a real increase in the equation of state at high redshift.

Measurements from the quasar absorption lines, which are available for a larger redshift range, provide in general a more reliable reconstruction. For our fiducial parametrizations of $\omega(z)$, these datasets can give a qualitatively accurate account of the evolution of the equation of state parameter to higher redshifts.

Comparing the various fiducial models for the same observational dataset shows that (as one would expect) the redshift up to which the reconstruction remains accurate depends in part on the correct underlying model, specifically on whether its equation of state remains close to a cosmological constant or not. However, comparing the HIRES and ESPRESSO cases shows that one can go deeper in redshift by increasing the sensitivity of the measurements, since that allows one to add components to the reconstruction.

The combination of supernovae with quasar absorption lines data further improves the determination of the equation of state parameter. In particular, we can now obtain information on $\omega(z)$ all the way from $z \sim 0$ up to $z \sim 3$. The reconstruction using HIRES, benefiting from an almost one order of magnitude improvement in the sensitivity of the QSO data points, is substantially better than the one obtained with ESPRESSO.

Model	A ($N_{\rm b} = 20$)	B ($N_{\rm b} = 20$)	A ($N_{\rm b} = 30$)	B ($N_{\rm b} = 30$)
Constant	1.14	0.52	1.39	0.63
Step	2.10	0.96	2.53	1.16
Bump	1.65	0.75	2.00	0.91

Table 4.1: The coefficients A and B in the fitting formula 4.4, assuming $N_{\rm b} = 20$ (left side of the table) and $N_{\rm b} = 30$ (right side) PCA bins in the redshift range $0 < z < 4$ and uncertainties σ_α expressed in parts per million.

We can also compare the two methods of determining the optimal value of modes to keep in the reconstruction. We observe, from comparing Fig. 4.2 to Fig. 4.3, corresponding to different methods, that the latter method picks more modes, which leads to a more accurate reconstruction. Since we are including additional modes with progressively larger errors, the reconstructed equation of state in this case also has larger error bars. In other words, the normalization method provides a more conservative and accurate approach, while the risk method provides (appropriately) a more aggressive approach.

If now we further extend this work to a systematic study of possible observational strategies, it is of interest to find an analytic expression for the behaviour of the uncertainties of the best determined PCA modes described above. For this one needs to explore the range of parameters such as the number of α measurements (N_α) and the uncertainty in each measurement (σ_α). For simplicity we assume that this uncertainty is the same for each of the measurements in a given sample, and also that the measurements are uniformly distributed in the redshift range under consideration.

By exploring numbers of measurements N_α between 20 and 200, uniformly distributed in redshift up to $z = 4$, and individual measurement uncertainties between 10^{-5} and 10^{-8} we find the following fitting formula for the uncertainty σ_n for the n-th best determined PCA mode

$$\sigma_n = A \frac{\sigma_\alpha}{N_\alpha^{0.5}} [1 + B(n-1)] \,. \tag{4.4}$$

The coefficients A and B will depend on the choice of the fiducial model, and also on the number of PCA bins assumed for the redshift range under consideration. Table 4.1 lists these coefficients for choices of 20 and 30 bins. Notice that it is useful to provide the uncertainly σ_α in the fitting formula in parts per million, since in that case the coefficients A and B are of order unity.

Model	Average Error	Max. Error
Constant	29%	38%
Step	37%	48%
Bump	26%	37%
Average	51%	67%

Table 4.2: The average and maximal errors of our fitting formula 4.4, compared to the correct PCA result. We have assumed $N_{\rm b} = 20$. The first three lines show the results for each of the three fiducial models, while the fourth line shows the result of trying to describe all three models with a single "average" fitting formula, where the values of coefficients A and B are the averages of those for the individual models.

A comparison between the numerically determined values and our fitting formula indicates that for $N_\alpha > 50$ the present expression is reasonably accurate for all values up to and including $n = 6$, while for a smaller number of measurements the number of accurately determined modes is less than 6. For example for $N_\alpha = 20$ only the first two modes obey the above relation, with the uncertainty in next two being slightly higher than suggested by the formula—and that of the next two significantly so. Specifically, Table 4.2 shows the average and maximal relative error obtained by sampling the above parameter space of $(\sigma_\alpha, N_\alpha, n)$, for a fixed number of redshift bins $N_{\rm b} = 20$. The maximal errors always occur for high n and low N_α, while in the opposite corner of parameter space they are below 10%. By sampling uniformly in N_α and in the logarithm of σ_α one obtains average uncertainties around 30%, which are adequate considering the simplifying assumptions in our modelling.

Overall, the fitting formulae show some dependence on the specific model being considered. One may ask if by taking say the arithmetic mean of the values of the coefficients A and B for the three models one will obtain a generic fitting formula that will be reasonable for all three. The last line of Table 4.2 shows that this is not the case, as the uncertainties worsen considerably: the average values of A and B are quite close to those of the bump fiducial model, but these coefficients do not perform as well for the other models. This model-dependence should therefore be taken into consideration if we want to establish a simple optimization pipeline, since the correct redshift evolution of the dark energy equation of state is not known *a priori* (certainly not at the high redshifts that can be probed thorough this method). There is also a dependence on the number of bins, which is to be expected: as we increase the number of bins the uncertainties in each bin will increase. Despite these caveats, the fitting formulas, once further calibrated using

actual data allow us to quantify the ability of a particular spectrograph to distinguish between different models.

We can now put together the results of the two equations (3.6) and (4.4) to obtain a UVES-calibrated PCA formula

$$\sigma_n = A[1 + B(n-1)]\frac{\sigma_\alpha}{\sqrt{N_\alpha}} = A[1 + B(n-1)]\left[\frac{C(N_\alpha)}{T}\right]^{1/2} , \tag{4.5}$$

where the UVES $C(N)$ formula is given by Eq. (3.6). The most striking feature of this result is the explicit (and strong) dependence on the number of sources. Future improvements will come from a better sample selection and optimized acquisition/calibration methods and both of these are expected to significantly reduce this dependence, even eliminating it for moderately sized samples of absorbers. In the case of the ELT-HIRES, a further improvement will come from the larger collecting power.

With simple but reasonable extrapolations of the $C(N)$ we can forecast the expected changes to the UVES formula, and from this carry out an assessment of the impact of these measurements for constraining dark energy. We shall consider the three scenarios presented before in equations:

- $C(N_\alpha)_{BASE} = 0.31\, N_\alpha + 5.02$ - equation (3.7);
- $C(N_\alpha)_{ESPRESSO} = 5.02/9$ - equation (3.8);
- $C(N_\alpha)_{HIRES} = 5.02/300$ - equation (3.9).

Figures 4.4 and 4.5 depict the uncertainty in the best-determined PCA mode, for the three observational scenarios discussed above and the three fiducial models considered (the constant, step and bump models). In these, and throughout the discussion in this section, we assumed 20 PCA bins ($N_b = 20$, cf. Table 4.1). The former figure highlights the dependence on the number of sources in the baseline scenario, while the latter figure highlights the gains to be expected from ESPRESSO and ELT-HIRES. For the baseline scenario in this latter plot we assumed a number of sources equal to half the number of nights, which is a typical number for current observations.

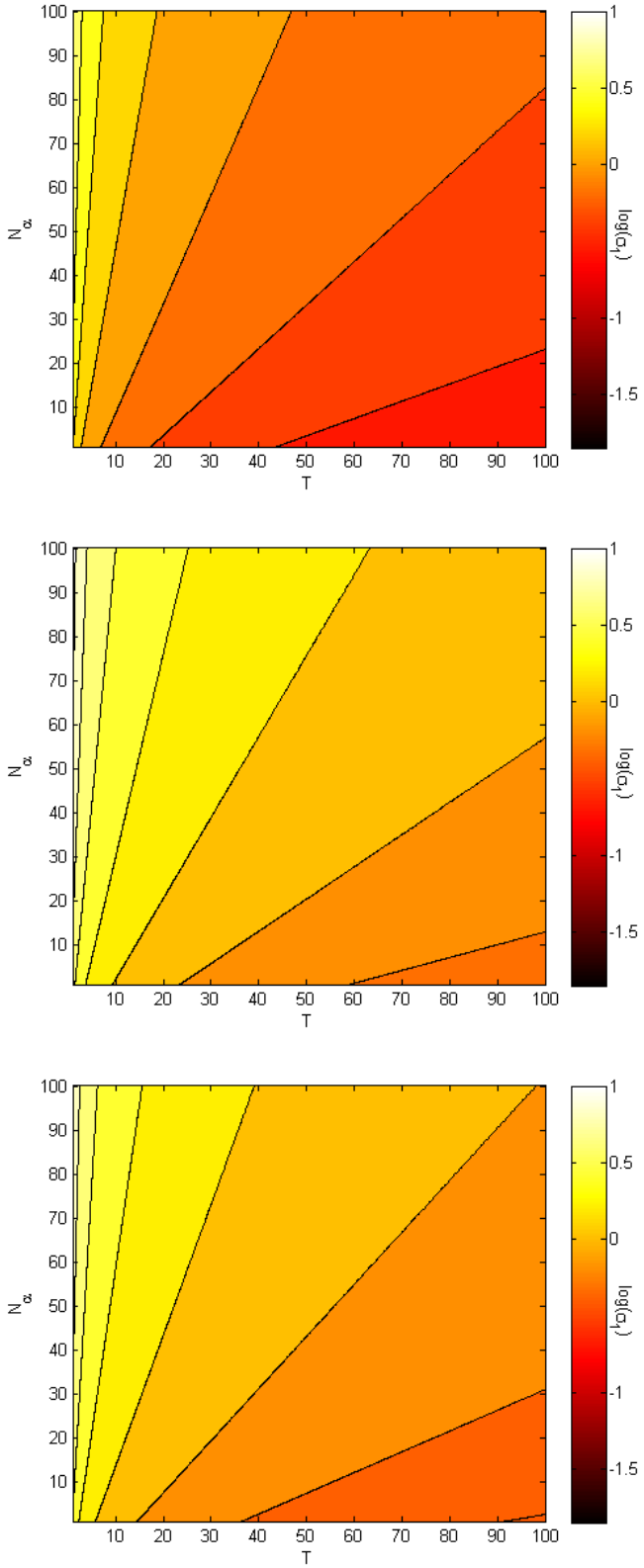

Figure 4.4: The uncertainty in the best-determined PCA mode in baseline scenario described in the main text, as a function of the number of nights of observation and absorbers measured, respectively for the constant, step and bump fiducial models (top to bottom). In each case the colormap indicates the logarithm of the uncertainty.

An alternative way to quantify the expected improvements with ESPRESSO and ELT-HIRES

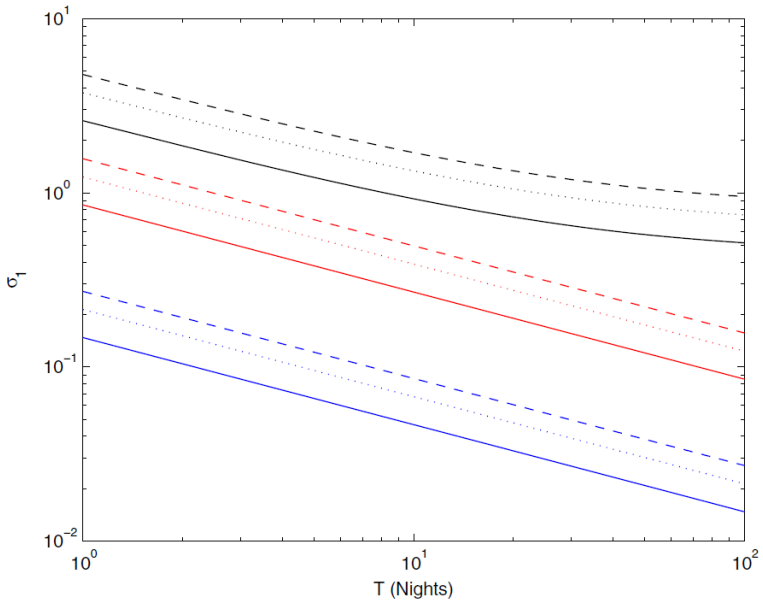

Figure 4.5: The uncertainty in the best-determined PCA mode in the three scenarios discussed in the main text, for each of the fiducial models considered. The top (black), middle (red) and bottom (blue) sets of three lines correspond to the baseline, ESPRESSO and ELT-HIRES cases respectively. In each set the solid, dashed and dotted lines respectively correspond to the constant, step and bump fiducial models.

Model	Baseline	ESPRESSO	ELT-HIRES
Constant	8.2	0.7	0.02
Step	70.0	2.5	0.07
Bump	23.6	1.5	0.05

Table 4.3: Number of nights needed to achieve an uncertainty of unity in the best-determined PCA mode, $\sigma_1 = 1$, for the various scenarios and fiducial models considered. For the baseline scenario $N_\alpha = T/2$ was assumed.

is to estimate the number of observation nights needed to obtain an uncertainty in the best-determined PCA mode of $\sigma_1 = 1$. This is shown in Table 4.3, where we again assumed $N_\alpha = T/2$ for the baseline scenario, and the gains are obvious. Note that here the model-dependence is enhanced, since the observation time will depend on the square of the coefficent A.

For a more ambitious goal, we can instead estimate the number of nights needed to reach the same sensitivity on the first PCA mode with a 'SNAP-like' dataset of 3000 supernovas. This turns out to be $\sigma_{1,SNAP} \sim 0.033$, with the model dependence appearing at the next decimal place (Amendola et al. 2012). In this case we find that this level of sensitivity is not achievable at all with current facilities, while our estimates for ESPRESSO and ELT-HIRES are listed in Table 4.4. It's important to note that a few tens of nights are sufficient for ELT-HIRES, further highlighting the key role that the ELT will be able to play on fundamental cosmology.

Model	ESPRESSO	ELT-HIRES
Constant	649.8	19.5
Step	2231.6	66.9
Bump	1420.1	42.6

Table 4.4: Number of nights needed to achieve, with α measurements uniformly spaced in redshift, an uncertainty in the best-determined PCA mode equal to that expected from a SNAP-like dataset of 3000 Type Ia supernovas, for the ESPRESSO and ELT-HIRES scenarios and the various fiducial models considered. Note that this is not possible at all in the baseline UVES-like scenario

We also note that a uniform redshift cover is important in obtaining these results. Moreover the range of redshifts considered will also play a role, as it will determine how many useful transitions will fall within the range of the spectrograph.

Future Supernovae tipe Ia Surveys

We will add to the PCA analyses further expected data for future Type Ia supernova surveys. We will consider the following datasets:

- A low-redshift sample, henceforth denoted **LOW**, of 3000 supernovas uniformly distributed in the redshift range $0 < z < 1.7$, with an uncertainty on the magnitude of $\sigma_m = 0.11$. These numbers are typical of "SNAP-like" future supernova datasets and were also used in Huterer and Starkman (2003) (thus providing a useful point of comparison).

- An intermediate redshift sample, henceforth denoted **MID**, of 1700 supernovas uniformly distributed in the redshift range $0.75 < z < 1.5$ and with the same σ_m as before. This is representative of recent proposals such as DESIRE Astier et al. (2014).

- A high-redshift sample of supernovas identified by JWST NIRcam imaging Riess & Livio (2006) and then characterized by extremely large telescopes on the ground such as the E-ELT and the TMT. Based on their respective Phase A studies we assume a sample of 50 supernovas in the range $1 < z < 5$ for the E-ELT Thatte et al. (2010) and a sample of 250 supernovas in the range $1 < z < 3$ for the TMT Silva et al. (2007). These will be denoted **ELT** and **TMT** respectively, and they will provide a useful proxy for studying the importance of the redshift lever arm versus the size of the sample. The redshift distribution of these supernovas is not easy to extrapolate, since even the most detailed current studies such as

those of the SNLS Perrett et al. (2012) only reach $z \sim 1$, but in the absence of more detailed information we again assume a uniform distribution in the respective redshift ranges and the same σ_m as before.

For the fine-structure constant measurements we will maintain the Baseline and Ideal scenarios, on the ESPRESSO spectrograph for the VLT and ELT-HIRES for the E-ELT as used before; in the tables that follow we will denote them **ESP** and **HRS** respectively. Specifically we consider the following two scenarios.

For our PCA analysis we assume 30 redshift bins in the range $0 \leq z \leq 4$. In the case where ELT supernovas are used, the last bin is extended until $z = 5$.

For comparison purposes we also briefly consider a case with only 20 bins. This serves to provide an illustration of the effects of redshift resolution on the reconstruction. Using too few bins is likely to erase useful information (especially if the behaviour of the dark energy equation of state is non-trivial), while using too many will lead to very little observational information in some (or all) bins, which runs the risk of misinterpreting noise as non-trivial information. To a large extent the choice of the optimal number of bins will depend on the available datasets themselves; while we won't address this issue explicitly here, we nevertheless quote the results with the two choices of bins to provide the reader with an illustration of the importance of an adequate choice.

In order to quantify gains in sensitivity we used two different diagnostics. The simplest one is the number of PCA modes with uncertainties below $\sigma_{PCA} = 0.3$;

Tables 4.5 and 4.6 display these numbers, respectively for the Constant and Step fiducial models, assuming the Baseline scenario for α measurements, and for various combinations of supernova datasets. Considering supernova data only, the MID sample adds one mode, and the further inclusion of ELT supernovas may add an additional one. When combining supernova and α measurements, ESPRESSO may add up to two modes while ELT-HIRES adds many more. For the combined datasets, whether the TMT sample (more supernovas at lower redshifts) or the E-ELT one (fewer supernovas at higher median redshift) is the more informative one is model-dependent. The reason why more modes are well characterized in the Constant than in the Step case is that, with our choice of high-redshift normalization for the α variations, a uniform distribution of the measurements in redshift turns out to be an optimal observational strategy for

the Constant case, but is far from optimal for the Step case; this is further discussed in Leite et al. (2014). Here we have chosen to keep the assumption of uniform redshift sampling precisely to highlight this model-dependence.

A somewhat more informative diagnostic is "figure of merit" defined as the inverse of the product of the uncertainties of the two best determined modes, $FoM = 1/(\sigma_1\sigma_2)$.

Table 4.5: Number of PCA modes with uncertainties below $\sigma_{PCA} = 0.3$, assuming the "Constant" fiducial model, the "Baseline" scenario for α measurements, and 30 redshift bins.

	Sne only	Sne + ESP	Sn + HRS
LOW	3	5	17
LOW + MID	4	5	18
LOW + ELT	4	5	16
LOW + MID + ELT	4	6	16
LOW + TMT	4	5	17
LOW + MID + TMT	4	5	18

Table 4.6: Number of PCA modes with uncertainties below $\sigma_{PCA} = 0.3$, assuming the 'Step' fiducial model, the 'Baseline' scenario for α measurements, and 30 redshift bins.

	Sne only	Sne + ESP	Sne + HRS
LOW	3	4	9
LOW + MID	4	4	10
LOW + ELT	4	4	10
LOW + MID + ELT	5	5	10
LOW + TMT	4	4	9
LOW + MID + TMT	5	5	11

The figures of merit for the baseline case of α measurements are shown in Tables 4.7 and 4.8, respectively for the Constant and Step fiducial models. In both cases we compare the results obtained with 20 or 30 bins. Table 4.9 shows the results for the Ideal α datasets and 30 redshift bins, comparing the results for the two fiducial models.

We note that the gains in sensitivity to the dark energy equation of state due to ESPRESSO measurements are relatively modest in the Baseline case, but significant (up to about a factor of 2) in the Ideal case. ELT-HIRES, on the other hand, will lead to dramatic improvements (sometimes more than a factor of 50).

It's also noteworthy that judging by this figure of merit diagnostic the impact of the E-ELT supernovas is always greater than that of the TMT supernovas. This is the case whether one is using supernova data only or a combination of supernovas and α measurements. Note that for the case of supernovas only, the 50 ELT supernovas (uniformly distributed in the range $1 < z < 5$) would not only be more constraining than the 250 TMT supernovas (in the range $1 < z < 3$) but also more constraining than the 1700 MID supernovas (in the range $0.75 < z < 1.5$).

There are some obvious caveats to this comparison. Firstly, finding very high redshift supernovas will be difficult, and current estimates of expected rates are at best uncertain. Moreover, the E-ELT or TMT time required to characterize them will certainly be costly, and we are taking for granted a temporal overlap between JWST and the relevant E-ELT and TMT instruments. Nevertheless, the results of this comparison do highlight the importance of the redshift lever arm in characterizing dynamical dark energy.

Table 4.7: Figures of merit for the dark energy equation of state, assuming the 'Constant' fiducial model and the 'Baseline' scenario for α measurements. For each pair of entries the top and bottom lines respectively assume 20 and 30 redshift bins.

	Sne only	Sne + ESP	Sne + HRS
LOW (20)	539	546	5215
LOW (30)	409	412	3574
LOW + MID (20)	1090	1096	5331
LOW + MID (30)	839	843	3655
LOW + ELT (20)	1194	1215	8055
LOW + ELT (30)	881	888	4947
LOW + MID + ELT (20)	2371	2392	8493
LOW + MID + ELT (30)	1973	1980	5286
LOW + TMT (20)	808	814	5302
LOW + TMT (30)	631	634	3642
LOW + MID + TMT (20)	1581	1586	5520
LOW + MID + TMT (30)	1253	1256	3814

As explained in Appendix A, one expects that the error normalization method will generically select more modes than risk minimization. This will therefore lead to a more accurate reconstruction (ie, closer to the correct fiducial model), though correspondingly also one with larger error bars. The normalization method is therefore the more conservative one, while the risk method is

Table 4.8: Figures of merit for the dark energy equation of state, assuming the 'Step' fiducial model and the 'Baseline' scenario for α measurements. For each pair of entries the top and bottom lines respectively assume 20 and 30 redshift bins.

	Sne only	Sne + ESP	Sne + HRS
LOW (20)	536	541	1358
LOW (30)	404	407	982
LOW + MID (20)	1084	1089	2003
LOW + MID (30)	831	834	1462
LOW + ELT (20)	1225	1243	3206
LOW + ELT (30)	881	885	1738
LOW + MID + ELT (20)	2432	2450	2561
LOW + MID + ELT (30)	2175	2176	2356
LOW + TMT (20)	821	824	1453
LOW + TMT (30)	634	636	1055
LOW + MID + TMT (20)	1605	1608	2209
LOW + MID + TMT (30)	1260	1262	1636

Table 4.9: Figures of merit for the dark energy equation of state, assuming the 'Ideal' scenario for α measurements and 30 redshift bins. For each pair of entries the top and bottom lines respectively correspond to the Constant and Step fiducial models.

	Sne only	Sne + ESP	Sne + HRS
LOW (c)	409	996	58684
LOW (s)	404	554	11228
LOW + MID (c)	839	1352	58737
LOW + MID (s)	831	955	11295
LOW + ELT (c)	881	1515	79431
LOW + ELT (s)	881	1064	18176
LOW + MID + ELT (c)	1973	2357	79639
LOW + MID + ELT (s)	1971	2133	18652
LOW + TMT (c)	631	1089	58740
LOW + TMT (s)	634	712	11335
LOW + MID + TMT (c)	1253	1443	58846
LOW + MID + TMT (s)	1260	1328	11514

more aggressive. We will further quantify this below.

Importantly, because we truncate the above sum (neglecting the poorly determined modes with high amplitudes at larger redshift) the reconstructed equation of state necessarily tends to zero for sufficiently large redshift Huterer and Starkman (2003). This unavoidable feature of the

PCA truncation method can be confused with a real increase in the equation of state at high redshift. This is another reason for wanting to extend the redshift range and the sensitivity of the measurements: they will lead to more reliable reconstructions at higher redshifts.

Figure 4.6 shows examples of reconstructions, for various choices of datasets, for the *Step* model, using either method to truncate the series; these correspond, respectively, to the top and bottom set of 9 panels. In both cases we assumed the Baseline scenario for α measurements. Note that in this and subsequent plots we always plot the reconstructed equation of state until redshift $z = 4$, even though for the E-ELT supernova case there will be measurements until $z = 5$. (In a given figure the same mocks have been used for all panels, but different mocks were used for different figures; this choice of mocks does not significantly affect our results.)

Naturally the step model provides a best-case scenario, since the correct fiducial equation does approach zero at high redshifts. This comparison makes it clear that the risk minimization method leads to a reconstruction with nominally very small error bars, but also one that may be somewhat biased. It is clear from the plots that this bias can be decreased either by extending the redshift lever arm (compare the left-most column, for reconstructions with supernovas only) or by increasing their sensitivity (compare the middle and right-most set of plots, which respectively include ESPRESSO and ELT-HIRES α measurements). On the other hand the normalization method in this case yields very conservative error bars and an almost perfect reconstruction, as long as one has a sufficient amount of data deep in the matter era.

Conversely the case of the *Constant* equation of state provides a worst-case scenario, as shown in Fig. 4.7. Here the reconstruction will necessarily be biased at sufficiently high redshifts. In other words, the reliability of the reconstruction at high redshift will be model-dependent. This much is of course expected, but these plots again make it clear that the reliability can always be increased (all else being equal) by extending the redshift range where data is available and improving their sensitivity—compare the reconstructions using ESPRESSO and ELT-HIRES in this figure. Since one does not a priori know the high-redshift behavior of the equation of state, going as deep in redshift as possible is a mandatory aspect of any observational strategy optimization. Tests of the stability of the fine-structure constant can therefore play a key role in this endeavor. It remains true in this case that the normalization method to truncate the series leads to a more

robust reconstruction. In Fig. 4.8 it's shown the case of the *Bump* equation of state that shows the same bias at sufficiently high redshifts.

In order to further quantify the impact of some of our assumptions on the above results, Fig. 4.9 shows the results of two other reconstructions for the constant fiducial model case, where we now assumed the Ideal scenario for α measurements. This comparison (which will only affect the cases with α measurements) clearly shows that with the increased sensitivity and number of measurements of the Ideal scenario the reliability of the reconstruction is significantly improved, both in terms of error bars in the various redshift bins and in terms of the maximum value of the redshift where the reconstruction is not significantly biased. The panels corresponding to the *Constant* model are particularly illuminating in illustrating the relative contributions of the supernova and α datasets: the difference between the E-ELT and TMT supernovas are clearly visible, and indeed even enhanced in this case by the presence of similarly sensitive E-ELT α measurements.

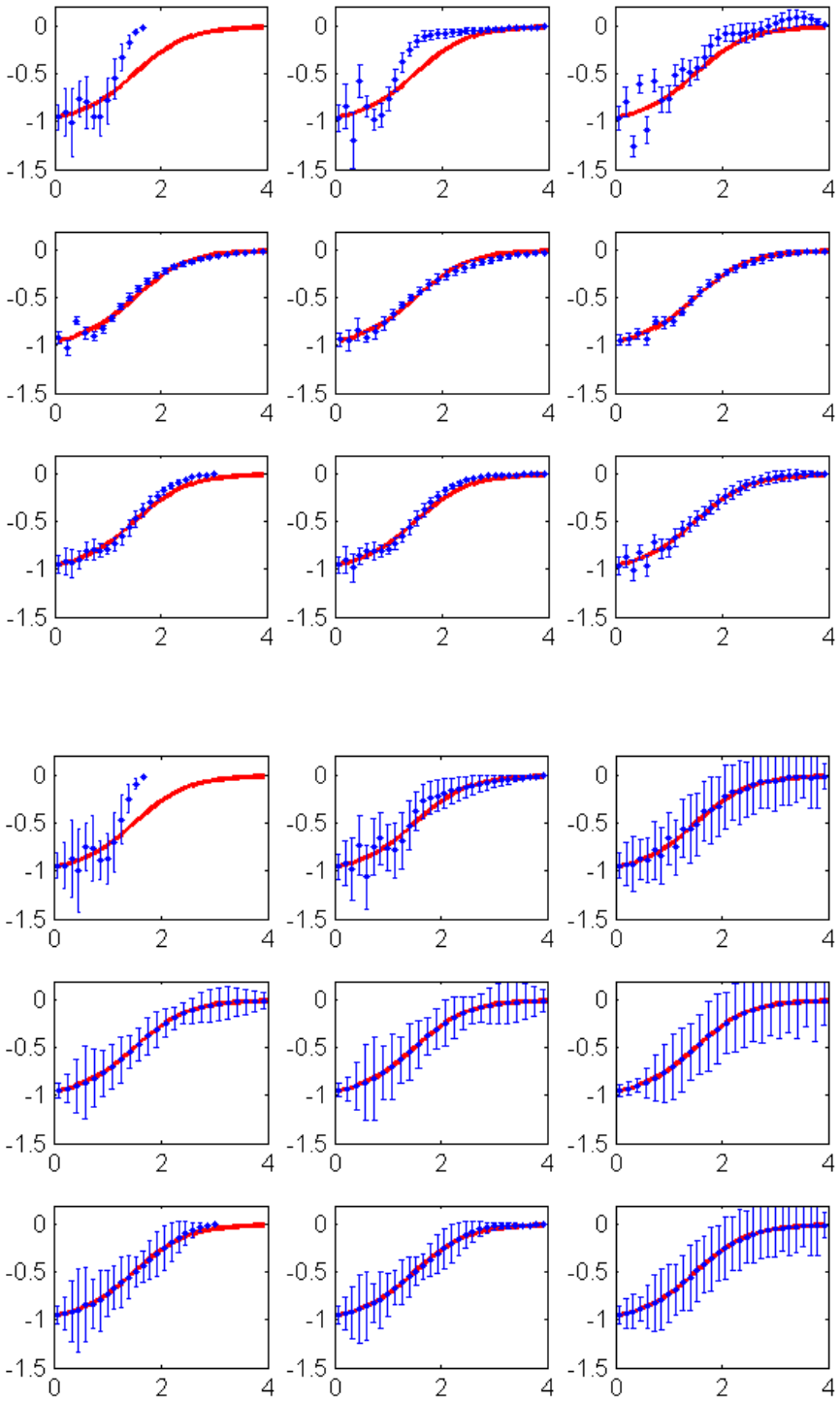

Figure 4.6: Examples of dark energy equation of state reconstructions for the *Step* fiducial model, using the risk minimization and normalization methods (top and bottom set of plots, respectively. All panels show the equation of state $\omega(z)$ plotted as a function of redshift. In each set of plots the left panels correspond to supernova data only, the middle ones to the combined supernova and ESPRESSO data, and the right ones to the combined supernova and ELT-HIRES data, while the three lines correspond to LOW+MID, LOW+MID+ELT and LOW+MID+TMT. In all cases we assumed the Baseline scenario for α measurements.

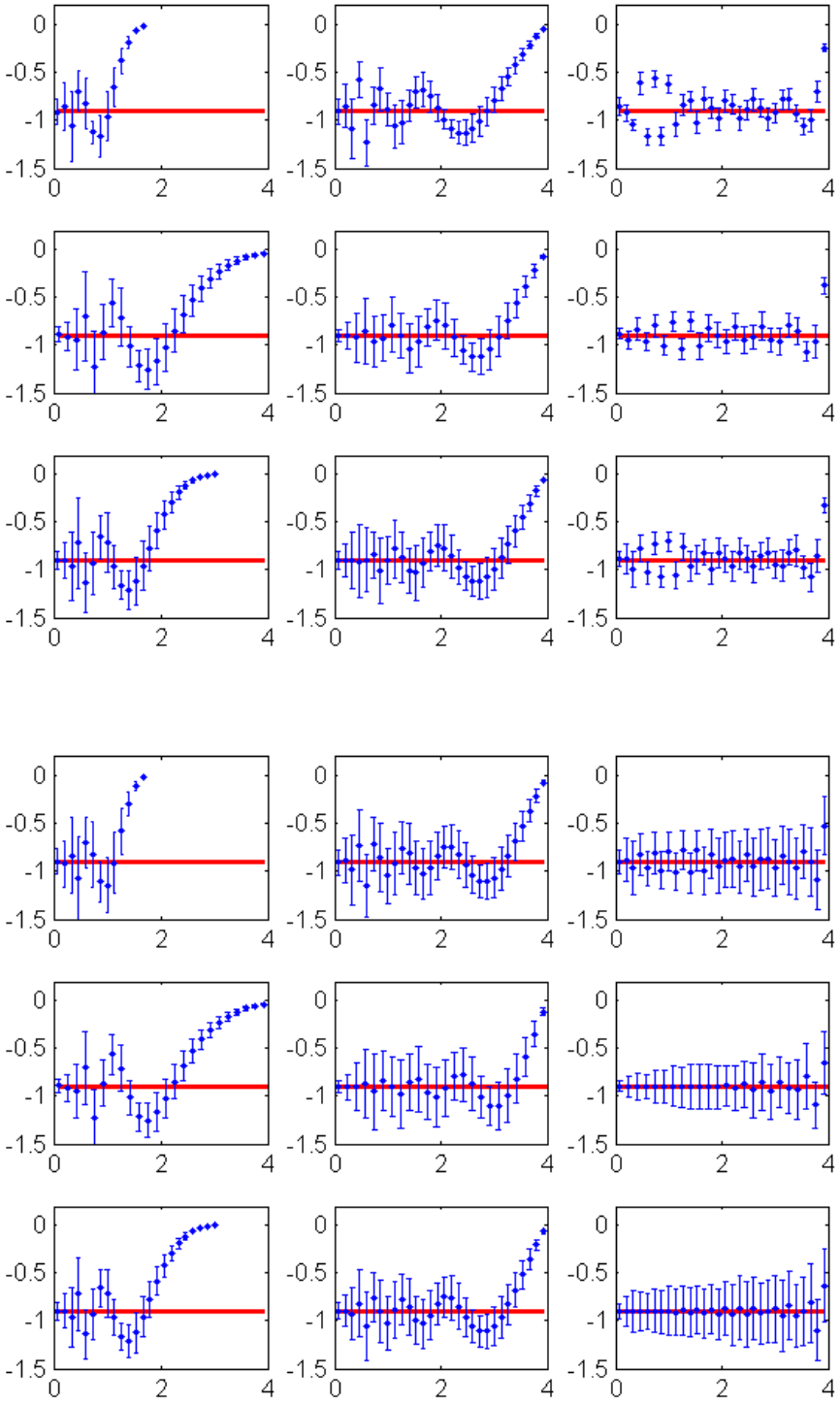

Figure 4.7: Examples of dark energy equation of state reconstructions for the *Constant* fiducial model, using the risk minimization and normalization methods (top and bottom set of plots, respectively. All panels show the equation of state $\omega(z)$ plotted as a function of redshift. In each set of plots the left panels correspond to supernova data only, the middle ones to the combined supernova and ESPRESSO data, and the right ones to the combined supernova and ELT-HIRES data, while the three lines correspond to LOW+MID, LOW+MID+ELT and LOW+MID+TMT. In all cases we assumed the Baseline scenario for α measurements.

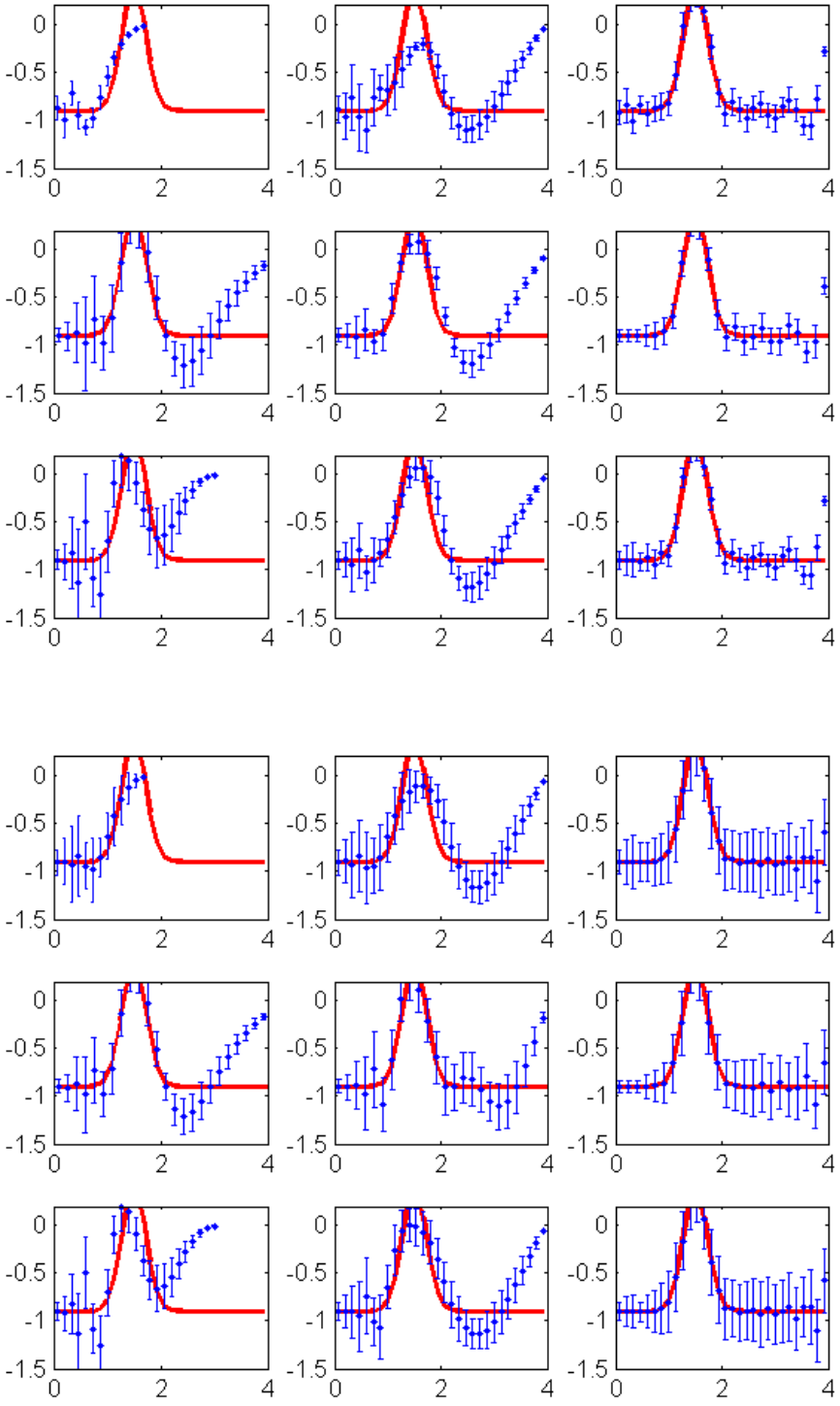

Figure 4.8: Examples of dark energy equation of state reconstructions for the *Bump* fiducial model, using the risk minimization and normalization methods (top and bottom set of plots, respectively. All panels show the equation of state $\omega(z)$ plotted as a function of redshift. In each set of plots the left panels correspond to supernova data only, the middle ones to the combined supernova and ESPRESSO data, and the right ones to the combined supernova and ELT-HIRES data, while the three lines correspond to LOW+MID, LOW+MID+ELT and LOW+MID+TMT. In all cases we assumed the Baseline scenario for α measurements.

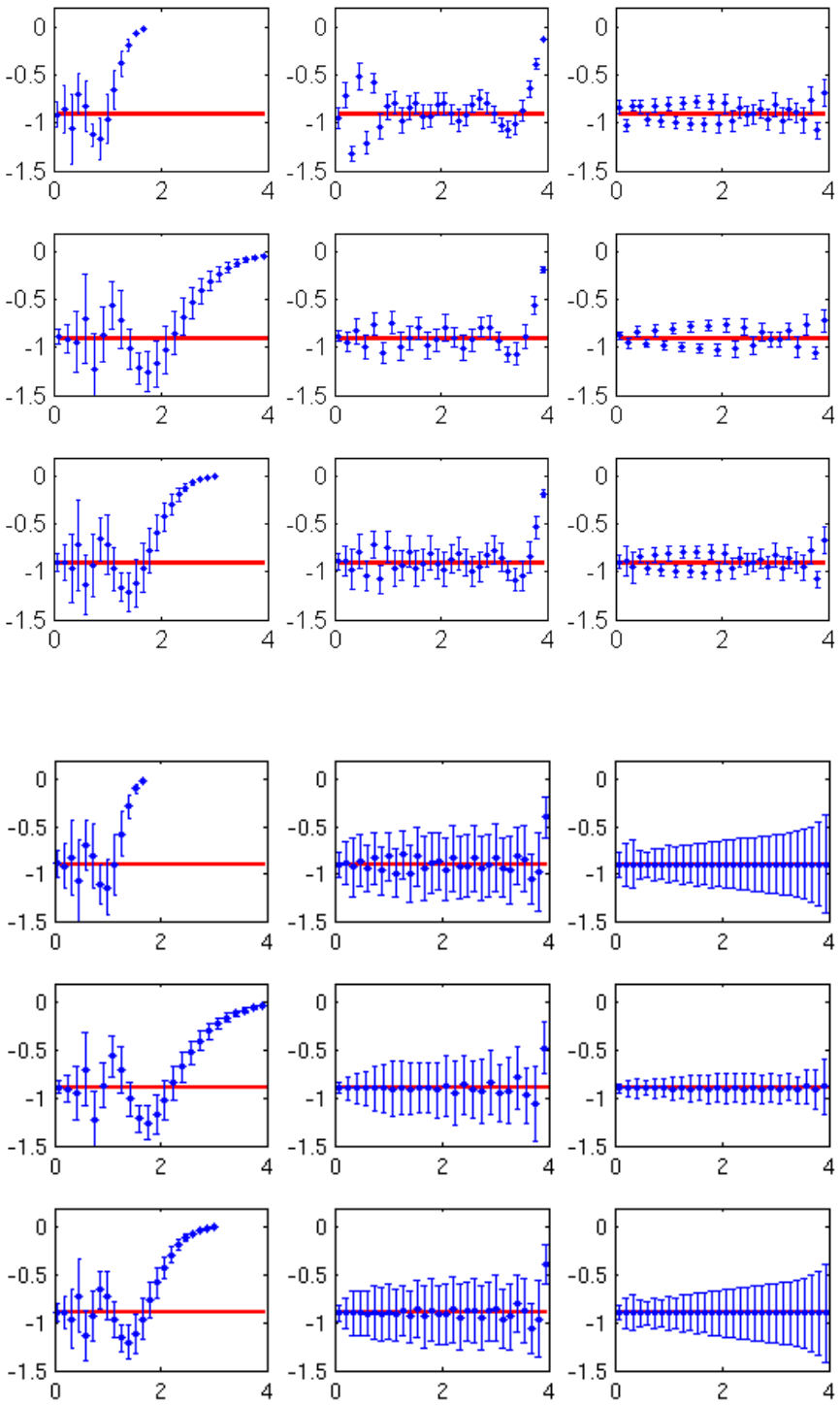

Figure 4.9: Further examples of dark energy equation of state reconstructions for the *Constant* fiducial model. Parameter choices are identical to those of Fig. 4.7, except that we now assumed the Ideal scenario for α measurements.

4.2 FORECAST RESULTS FOR THE TARGET LIST OF ESPRESSO

We will try to apply the PCA analysis to the target list for $\Delta\alpha/\alpha$ measurements, of ESPRESSO, table 3.1. We will test the potential of the 15 measurements in terms of constraints on the equation of state of dark energy by themselves.

The number of measurement assumed are lower than the ones from PCA analyses in the previous section 4.1, and because of that the results are expected to be worse.

The data will not be equally spaced in redshift, but follow the redshifts given by the target list (3.1). The uncertainty will be constant in every target and defined as before for the baseline and ideal scenarios (section 4.1).

We assume the number of bins to be such that it allows that each bin has two measurements (7 bins). We assumed the two measurements on $J110325 - 264515$ as one entry only. In total we get 14 measurements, from redshift 1.35 to 3.02 distributed accordingly with the real values of the target list.

Using the uncertainties of a baseline scenario for ESPRESSO we weren't able to perform the reconstruction, since the numbers of modes chosen by the risk and normalization methods were both 0. When using the ideal scenario with better expected uncertainties in each measurement we were able to do the reconstruction of the equation of state of dark energy for the three different fiducial functions, as can be seen in the top panel of figure 4.10 for the Risk truncation method, and in the bottom panel of figure 4.10 for the normalization method.

Although the reconstruction is not accurate at every point and for the three fiducial models, for the normalization method we get a consistent reconstruction for most of the bins.

The potential of ESPRESSO to distinguish these different 3 toy models is difficult to quantify. In principle, assuming that the minimization methods is the one that gives the accurate results, we can infer that the models are not distinguishable in the whole redshift range, but for some bins the step equation of state reconstruction can be separated from the other two.

In conclusion the 14 measurement will not be able to reconstruct the equation of state and distinguish models in a convincing manner by themselves. However, improvements can be achieved by adding measurements, improving the uncertainties, or combining these measurements with

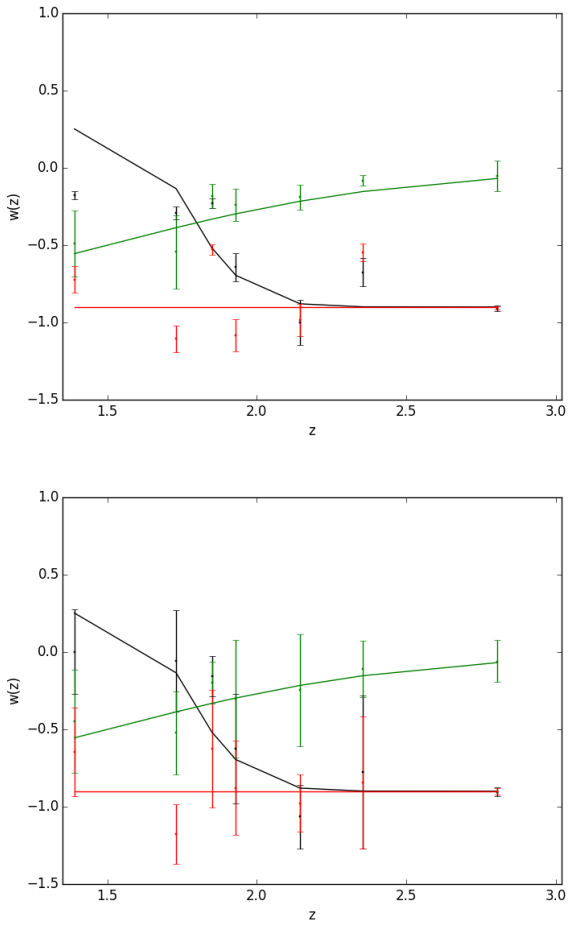

Figure 4.10: Reconstruction of the equation of state parameter for an ideal scenario for the target list of ESPRESSO, presented in section 3.2. The top panel represents the reconstruction using the risk truncation method. The bottom panel represents the reconstruction using the normalization truncation method.
The fiducial equation of state and its reconstruction are red for the **constant** one, green for the **step** and black for the **bump** one.

supernova data.

Chapter 5.

Conclusions

The goal of this Master thesis was to collect and to understand the existing tests of the stability of the fine-structure constant, and with that choose the targets for the ESPRESSO spectrograph guaranteed time of observation of the Consortium. As type Ia Supernovae data these measurements can be used to constrain the equation of state of dark energy as a function of the look-back time. We used that fact to further study the impact of future instrumentation on dark energy.

I will summarize the principal conclusions of the ESPRESSO observational strategy on fundamental constants:

- We built a list of targets that have the optimal characteristics for providing a low uncertainty measurement of $\Delta\alpha/\alpha$. Depending on the needs of the Consortium the priority targets within the list can be changed and adapted. Some of the theoretical priorities can be pointed as the time allocation given for the observations; the test of the dipole model; systems with more than one fundamental constant.

- As not many targets of μ are known for the wavelength of ESPRESSO, the existing ones are a priority for the part of the science goals on μ measurements.

- The temperature of CMB measurements were not foreseen as a main scientific goal, but ESPRESSO GTO is able to preform this measurements if a system for α and/or μ has certain *CO* molecules transitions.

- When compared with its VLT predecessor spectrograph, UVES, ESPRESSO has a smaller redshift coverage, which implies that some transitions already observed for some targets will no longer be observed. And as shown before the number of transitions plays a role in the uncertainty of measurements.

- The study of existing datasets, such as the UVES one, gives us a useful way to validate our observational intuition. With that study we were able to infer the observational time dependences on other parameters.

In the final chapter of this work (chapter 4) we presented results for the use of measurements of the fine-structure constant and measurements of Type Ia Supernovae to constrain Dark Energy, modelling future programs and instruments with a Principal Component Analyses approach. The main results are presented below:

- Type Ia Supernovas are a classical way of constraining dark energy, but the usual redshift coverage only goes till $z \sim 1.7$. Complementing these constrains with fine structure constant measurements improves the precision and allow a larger redshift lever arm.
- ESPRESSO and ELT fundamental coupling stability tests will be able to improve our knowledge of the evolution of dark energy and be competitive, at least in the case of ELT, when compared with a satellite mission Supernova survey.
- The future planed Supernova surveys, should be able to detect some higher-z Supernovas, possibly up to $z \sim 5$. These will help to improve the equation of state constrains.
- When comparing scenarios to quantify the gains connected with this new Supernovae data, increasing the redshift lever arm is generally better than increasing the number of measurements.

In the last subsection we applied this PCA analysis to the ESPRESSO target list. We found that the target list alone in an ideal scenario can start to distinguish between models. On a 27 night GTO program we can not expect much more on the information of Dark Energy. The results are not a surprise due to the predictions on the previous ESPRESSO scenarios studies. (section 4.1)

One can be optimistic and say that with a few more measurements or lower uncertainties, the α variation measurements will start to be able to constrain dark energy by themselves. The first option can be achieved with an extended dedicated program beyond the GTO time . The second one will be possible with the start of operation of the HIRES for E-ELT.

As future work:

- The next step concerning the measurements of α, the plan and prediction of the ESPRESSO observation would be to further quantify the uncertainties of the measurement of the target list. This can be done simulating spectra with the known transitions in each one of them, and then adding the observational limitations of ESPRESSO. The resulting spectra would be used to do independent measurements as real spectra.
- Concerning the implications of these measurements for dark energy, we will further explore the part of quantifying the gains of having the GTO target list, by themselves and considering combinations with Supernova type Ia data.

The next years will certainly bring us closer to the answer to: Do constants vary or not?

Bibliography

G. Aad et al. (ATLAS Collaboration), *Phys. Lett. B* 716, 1 (2012).

A. Albrecht and G. Bernstein, *Phys. Rev. D*75, 103003 (2007).

A. Albrecht, A., L. Amendola, G. Bernstein, et al. (2009), arXiv:0901.0721.

M. Aldenius, S. Johansson, M. T. Murphy, *MNRAS* 370, 444-452 (2006).

L. Amendola, A. C. O. Leite, C. J. A. P. Martins, N. J. Nunes, P. O. J. Pedrosa, and A. Seganti, *Phys. Rev. D*86, 063515 (2012).

L. Anchordoqui and H. Goldberg, *Phys. Rev. D*68, 083513 (2003).

P. Astier, C. Balland, M. Brescia, E. Cappellaro, R. Carlberg, et al., *A&A* 572, A80 (2014).

V. Batteiger, S. Knünz, M. Herrmann, G. Saathoff, H. A. Schüssler, B. Bernhardt, T. Wilken, R. Holzwarth, T. W. Hänsch, T. Udem, *Phys. Rev. A*80, 022503 (2009).

J. Bagdonaitė, Ph.D. Thesis, Vrije Universiteit Amsterdam (2015).

J. C. Berengut, V. A. Dzuba, V. V. Flambaum, M. V. Marchenko, *Phys. Rev. A*70 064101 (2004b).

J. C. Berengut, V. A. Dzuba, V. V. Flambaum, M. G. Kozlov, M. V. Marchenko, M. T. Murphy, J. K. Webb, arXiv:physics/0408017 (2004a).

H. A. Bethe, E. E. Salpeter, *Quantum Mechanics of One- and Two-Electron Atoms* , Plenum, New York, NY, USA (1977).

P. Bonifacio, H. Rahmani, J. B. Whitmore, M. Wendt, M. Centurion, P. Molaro, R. Srianand, M. T. Murphy, P. Petitjean, I. I. Agafonova, S. D'Odorico, T. M. Evans, S. A. Levshakov, S. Lopez, C. J. A. P. Martins, D. Reimers, and G. Vladilo, *Astronomische Nachrichten* 335, No. 1, 83-91 (2014).

R. R. Caldwell and E. V. Linder, *Phys. Rev. Lett.* 95, 141301(2005).

H. Chand, R. Srianand, P. Petitjean, and B. Aracil, *A&A* 417, 853-871 (2004).

H. Chand, P. Petitjean, R. Srianand, and B. Aracil, *A&A* 430, 47-58 (2005).

H. Chand, R. Srianand, P. Petitjean, B. Aracil, R. Quast, and D. Reimers, *A&A* 451, 45-56 (2006).

S. Chatrchyan et al. (CMS Collaboration), *Phys. Lett. B* 716, 30 (2012).

T. Chiba and K. *Kohri, Prog. Theor. Phys.* 107, 631 (2002).

E. J. Copeland, N. J. Nunes, and M. Pospelov, *Phys. Rev. D*69, 023501 (2004).

T. Dent, S. Stern, and C. Wetterich, *J. Cosmol. Astropart. Phys.* 01, 038 (2009).

R. H. Dicke, *Phys. Rev.* 125, 2163 (1962).

G. R. Dvali and M. Zaldarriaga, *Phys. Rev. Lett.* 88, 091303 (2002).

V. A. Dzuba, V. V. Flambaum, J. K. Webb, *Phys. Rev. A*59 230237 (1999a).

V. A. Dzuba, V. V. Flambaum, J. K. Webb, *Phys. Rev. Lett.* 82 888891 (1999b).

V. A. Dzuba, V. V. Flambaum, M. T. Murphy, J. K. Webb, *Phys. Rev. A*63 042509 (2001).

V. A. Dzuba, V. V. Flambaum, M. G. Kozlov, M. Marchenko, *Phys. Rev. A*66 022501 (2002).

T. M. Evans, M. T. Murphy, J. B. Whitmore, T. Misawa, M. Centurion, S. D'Odorico, S. Lopez, C. J. A. P. Martins, P. Molaro, P. Petitjean, H. Rahmani, R. Srianand, *MNRAS* 445, 128 (2014).

M. C. Ferreira, O. Frigola, C. J. A. P. Martins, A. M. R. V. L. Monteiro, J. Solà, *Phys. Rev. D*89, 083011 (2014).

U. Griesmann and R. Kling, *ApJ* 536, L113-L115 (2000).

R. Guimarães, P. Noterdaeme, P. Petitjean, C. Ledoux, R. Srianand, S. Lopez, H. Rahmani, *ApJ* 143, 147 (2012).

S. Hannemann, E. J. Salumbides, S. Witte, R. T. Zinkstok, E. van Duijn, K. S. E. Eikema, W. Ubachs, *Phys. Rev. A*74, 012505 (2006).

D. Huterer and G. Starkman, *Phys. Rev. Lett.* 90, 031301(2003).

J. A. King, J. K. Webb, M. T. Murphy, and R. F. Carswell, *Phys. Rev. Lett.* 101, 251304 (2008).

J. A. King, Ph.D. Thesis, University of New South Wales (2012), arXiv:1202.6365.

C. Ledoux, P. Petitjean, and R. Srianand, *Astroph. J. Lett.* 640, L25/L28 (2006).

A. C. O. Leite, C. J. A. P. Martins, P. O. J. Pedrosa, and N. Nunes, *Phys.Rev. D*90, 063519 (2014).

A. C. O. Leite, and C. J. A. P. Martins, *Phys. Rev. D*91, 103519 (2015).

S. A. Levshakov, P. Molaro, S. Lopez, S. D'Odorico, M. Centurión, P. Bonifacio, I. I. Agafonova1, and D. Reimers, *A&A* 466, 1077-1082 (2007).

A. Liddle, *An Introduction to Modern Cosmology, Second Edition*, pp. 188. ISBN 0-470-84834-0. Wiley-VCH , (2003).

J. Liske et al., Top Level Requirements For ELT-HIRES (2014), Document ESO 204697 Version 1.

R. Maiolino, M. Haehnelt, M. T. Murphy, et al. (2013), arXiv:1310.3163 .

V. Marra and F. Rosati, *J. Cosmol. Astropart. Phys.* 05, 011(2005).

C. J. A. P. Martins, *General Relativity and Gravitation*, 47, 1843 (2015).

J. C. Mather, D. J. Fixsen, R. A. Shafer, C. Mosier, and D. T. Wilkinson, *ApJ* 512, 511 (1999).

P. J. Mohr, D. B. Newell, and B. N. Taylor (2015), arXiv:1507.07956.

H. Mo, F. C. van den Bosch, and S. White, *Galaxy formation and evolution*, UK: Cambridge University Press (2010).

P. Molaro, D. Reimers, I. I. Agafonova, and S. A. Levshakov, *Eur. Phys. J. Spec. Top.* 163, 173-189 (2008).

P. Molaro, M. Centurion, J. B. Whitmore, T. M. Evans, M. T. Murphy, I. I. Agafonova, P. Bonifacio, S. D'Odorico, S. A. Levshakov, S. Lopez, C. J. A. P. Martins, P. Petitjean, H. Rahmani, D. Reimers, R. Srianand, G. Vladilo, M. Wendt, *A&A* 555, A68 (2013).

M. Mortonson, W. Hu, and D. Huterer, *Phys. Rev. D*80, 067301 (2009).

M. T. Murphy, Ph.D. Thesis, University of New South Wales (2002).

M. T. Murphy, J. K. Webb, and V. V. Flambaum, *MNRAS* 384, 1053-1062 (2008).

M. T. Murphy (private communication).

M. T. Murphy and J. C. Berengut, *MNRAS* 438, 388 (2014).

P. Noterdaeme, C. Ledoux, R. Srianand, P. Petitjean and S. Lopez, *A&A* 503, 765 (2009)

P. Noterdaeme, P. Petitjean, R. Srianand, C. Ledoux, and S. López, *A&A* 526, L7 (2011).

P. Noterdaeme, P. Petitjean and R. Srianand, *A&A* 578, L5 (2015)

F. Pepe, S. Cristiani, R. Rebolo, et al. *The Messenger*, 153, 6 (2013).

K. Perrett, M. Sullivan, A. Conley, S. GonzalezGaitan, R. Carlberg, et al., *ApJ* 144, 59 (2012).

J. C. Pickering, A. P. Thorne, J. E. Murray, U. Litzén, S. Johansson, V. Zilio, J. K. Webb, *MNRAS* 319, 163-167 (2000).

Planck Collaboration, P. A. R. Ade, N. Aghanim, et al., *A&A* 571, A16 (2014).

H. Rahmani, M. Wendt, R. Srianand, P. Noterdaeme, P. Petitjean, P. Molaro, J. B. Whitmore, M. T. Murphy, M. Centurion, H. Fathivavsari, S. D'Odorico, T. M. Evans, S. A. Levshakov, S. Lopez, C. J. A. P. Martins, D. Reimers, G. Vladilo, *MNRAS* 435, 861 (2013).

A. G. Riess and M. Livio, *ApJ* 648, 884 (2006).

E. J. Salumbides, S. Hannemann, K. S. Eikema, W. Ubachs, *MNRAS* 373, L41-L44 (2006).

D. Silva et al., TMT Detailed Science Case , Document TMT.PSC.TEC.07.003 Release 01 (2007).

R. Srianand, P. Noterdaeme, C. Ledoux and P. Petitjean, *A&A* 482, L39 (2008).

R. Srianand, N. Gupta, P. Petitjean, P. Noterdaeme and C. Ledoux, *MNRAS* 405, 1888/1900 (2010).

R. Srianand, N. Gupta, P. Petitjean, P. Noterdaeme, C. Ledoux, C. J. Salter, D. J. Saikia, *MNRAS* 421, 651/665 (2012).

N. Thatte, et al., SPIE Conference Series 7735, 77352 (2010).

J.-P. Uzan, *Living Rev. Relativity* 14, 2 (2011).

J. Webb, J. King, M. Murphy, V. Flambaum, R. Carswell, and M. Bainbridge, *Phys. Rev. Lett.* 107, 191101 (2011).

M. Wendt and D. Reimers, *Eur. Phys. J. Spec. Top.* 163, 197 (2008).

Appendix A.

Principal Component Analysis

PCA is a nonparametric method that is used in this work in order to constrain the dark energy equation of state $\omega(z)$. Its performance should not be compared with parametric methods, since the two are addressing different questions. Instead one should compare it with another nonparametric reconstruction, this is useful, for example, in order to compare the impact of the different datasets for a certain parametrization.

An advantage of PCA techniques is that they allow one to infer which and how many parameters can be most accurately determined with a given experiment. Instead of assuming a parametrization for the relevant observable (variable) with a set of parameters born of our theoretical prejudices, the PCA method leaves the issue of finding the best parametrization to be decided by the data itself.

In Huterer and Starkman (2003) and Albrecht and Bernstein (2007) the PCA approach was applied to the use of supernova data to constrain the dark energy equation of state, $\omega(z)$. Further work, in Amendola et al. (2012), used this same technique in combination with fine structure constant measurements. Here I will summarize formalism of PCA applied to the use of observables, at different redshifts (z), to constrain the dark energy equation of state, $\omega(z)$. The results of applying this method to different datasets are presented in chapter 4.

One can divide the relevant redshift range into N bins such that in bin i the equation of state parameter takes the value ω_i,

$$\omega(z) = \sum_{i=1}^{N} \omega_i \theta_i(z)\,. \tag{A.1}$$

Another way of saying this is that $\omega(z)$ is expanded in the basis θ_i, with $\theta_1 = (1, 0, 0, ...)$, $\theta_2 = (0, 1, 0, ...)$, etc.

In order to find the uncertainty of the parameters ω_i, we have to build a Fisher information matrix. For that the first step is to construct the Likelihood function for a generic observable $m(z_i, \omega_i, c) = \mu(z_i, \omega_i) + c$. For the purposes of this work this can be the apparent magnitude of a supernova, in which case

$$\mu = 5\log(H_0 d_L)\,, \qquad c = M + 25 - 5\log H_0 \tag{A.2}$$

or it can be connected to the relative variation of α obtained with quasar absorption spectra, for which

$$\mu = \ln[\kappa(\phi - \phi_0)]\,, \qquad c = \ln\zeta\,. \tag{A.3}$$

Then we find

$$L(w^i, M) \propto \exp\left[-\frac{1}{2}\sum_{i,j=1}^{N}(m - m_F)_i C_{ij}^{-1}(m - m_F)_j\right]. \tag{A.4}$$

where m_F means m evaluated at the fiducial values of the parameters, $m_F = m_F(z_i, \omega_i^F, c^F)$ and C^{-1} is the inverse of the correlation matrix of the data.

Defining $\beta = c - c^F$, and integrating the likelihood in β, we obtain the marginalized likelihood

$$L(\omega_i) \equiv \int_{-\infty}^{\infty} L(\omega_i, \beta)d\beta = \sqrt{\frac{2\pi}{A}}\exp\left[-\frac{1}{2}\sum_{i,j=1}^{N}(\mu - \mu_F)_i D_{ij}^{-1}(\mu - \mu_F)_j\right]$$

where $A = \sum_{i,j} C_{i,j}^{-1}$ and

$$D_{ij}^{-1} = C_{ij}^{-1} - \frac{1}{A}\sum_{k,l=1}^{N} C_{kj}^{-1}C_{li}^{-1}. \tag{A.5}$$

The Fisher matrix can be obtained by approximating $L(\omega_i)$ as a Gaussian in the theoretical parameters ω_i (the equation of state in each bin) centered around the fiducial model, and taking the inverse of the resulting correlation function. The Fisher matrix turns out to be

$$F_{kl} \equiv -\frac{\partial^2 \ln L}{\partial\omega_k \partial\omega_l}\bigg|_{w^F} = \sum_{i,j=1}^{N} \frac{\partial\mu(z_i)}{\partial\omega_k}\bigg|_{w^F} D_{ij}^{-1} \frac{\partial\mu(z_j)}{\partial\omega_l}\bigg|_{w^F},$$

where the derivatives are evaluated at the fiducial values of the parameters.

The precision on the measurement of ω_i can be inferred from the Fisher matrix of the parameters ω_i, specifically from $\sqrt{(F^{-1})_{ii}}$, and increases for larger redshift. One can however find a basis in which all the parameters are uncorrelated. This can be done by diagonalizing the Fisher matrix such that $F = W^T \Lambda W$ where Λ is diagonal and the rows of W are the eigenvectors $e_i(z)$ or the principal components. These define the new basis in which the new coefficients α_i are uncorrelated and now we can write

$$\omega(z) = \sum_{i=1}^{N} \alpha_i e_i(z)\,. \tag{A.6}$$

The diagonal elements of Λ are the eigenvalues λ_i (ordered from largest to smallest) and they define the variance of the new parameters, $\sigma^2(\alpha_i) = 1/\lambda_i$.

In Fig. A.1, we show the 3 best determined and 2 of the worst-determined eigenvectors for $\omega(z)$ for a reconstruction of the fiducial model $\omega(z) = -1$, with supernova type Ia and variation of α measurements. The best-determined modes peak at relatively low redshifts, while the higher modes (worst determined) have high frequencies and more information at higher redshits. A way to interpret this parametrization (Huterer and Starkman 2003)is to realize that the Mth best-determined eigenvector has precisely $M - 1$ nodes, leading to the interpretation that the first eigenvector corresponds to the "average of $\omega(z)$", the second one to the "first derivative of ω", the third one to the second derivative of ω", etc.

Folowing Huterer and Starkman (2003) and Albrecht and Bernstein (2007) one can now attempt a reconstruction $\omega(z)$ by keeping only the most accurately determined modes (the ones with largest eigenvalues). To do this, we need to decide how many components to keep. We must point out that the weak point of this procedure consists in neglecting the high frequency modes.

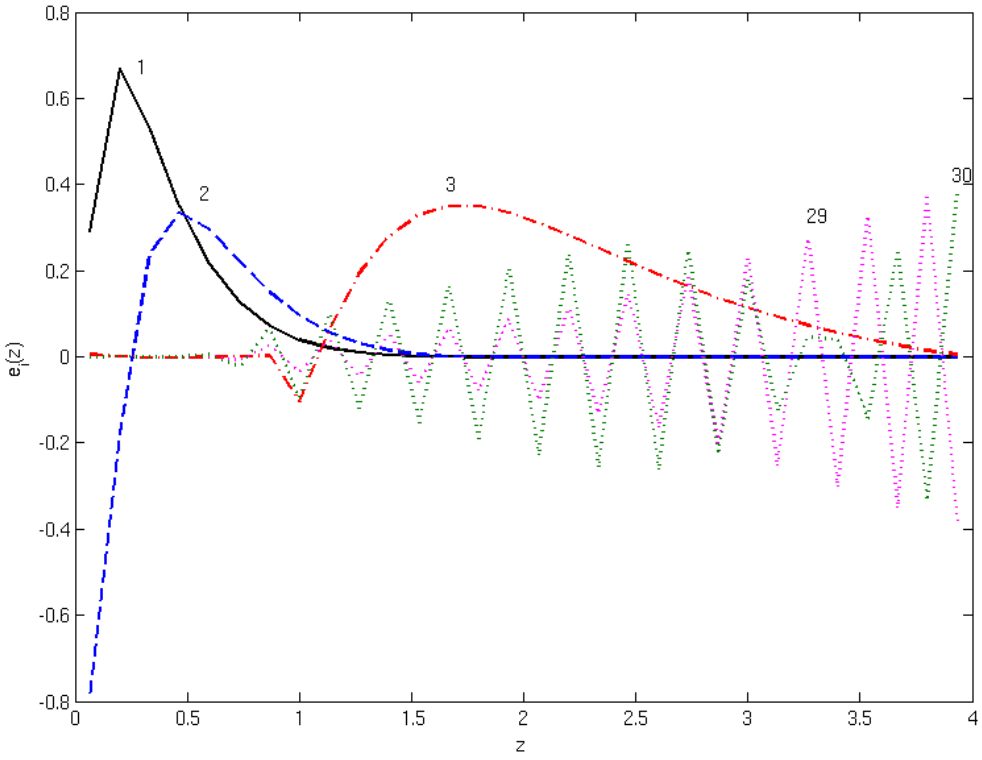

Figure A.1: The principal components of $\omega(z)$ for a reconstruction of the fiducial model $\omega(z) = -1$, with supernova type Ia and variation of α measurements. The three best determined and two worst determined eigenvectors are shown and labeled for clarity.

One may argue that the optimal value of modes M to be kept corresponds to the value that minimizes the risk, defined as Huterer and Starkman (2003)

$$risk = bias^2 + variance, \tag{A.7}$$

with

$$bias^2(M) = \sum_{i=1}^{N} \left(\tilde{\omega}(z_i) - w^F(z_i)\right)^2, \tag{A.8}$$

where the notation $\tilde{w}$ means that the sum in (A.6) runs from 1 to M, and

$$variance = \sum_{i=1}^{N} \sum_{j=1}^{M} \sigma^2(\alpha_j) e_j(z_i). \tag{A.9}$$

The bias measures how much the reconstructed equation of state, $\omega_{\rm rec}(z)$, differs from the true one by neglecting the high and noisy modes, and therefore typically decreases as we increase

M. The variance of $\omega(z)$, however, will increase as we increase M, since we will be including modes that are less accurately determined.

An alternative way to decide on the number of optimal modes is to choose the largest value for which the error is below unity, or equivalently, the RMS fluctuations of the equation of state parameter in such mode are

$$\langle (1+\omega(z))^2 \rangle = \sigma_i^2 \lesssim 1\,. \tag{A.10}$$

Having thus determined the optimal number of modes, we proceed with the normalization of the error following Albrecht et al. (2009) such that $\sigma^2 = 1$ for the worst determined mode and normalize the error on the remaining modes by taking

$$\sigma^2(\alpha_i) \rightarrow \sigma_n^2(\alpha_i) = \frac{\sigma^2(\alpha_i)}{1+\sigma^2(\alpha_i)}. \tag{A.11}$$

A comparison of the impact of the two truncation methods (risk method vs. normalization of the error) is presented in Amendola et al. (2012). The main difference is the effect on the size of the error bars of the reconstruction: the normalization of the error method appears to give more accurate (closer to the fiducial value) but less precise (more conservative errors) reconstructions when compared with the risk minimization procedure.

Appendix B.

Atomic Data for use in Many Multiplet Analyses

In table B.1 we list the atomic data and q-coefficients which were used in in the determination of the $\Delta\alpha/\alpha$ in tables C.1 and D.1. This version of the table is adapted from King's Ph.D. Thesis (2012), but an up-to-date table is maintained on-line, and can be consulted in https://researchdata.ands.org.au/laboratory-atomic-transition-absorption-spectroscopy/258554

Table B.1: Atomic data for transitions usable in many-multiplet or alkali-doublet analyses, i.e. transitions with precise laboratory wavelengths. Columns 1 and 2 show the common names used for the transitions. Column 3 shows the mass number for each ionic species. Column 4 gives the wavenumber of the transition. Column 5 gives the reference for the wavenumber measurement and/or calculations (specified below the table). Vacuum laboratory wavelengths, λ_0, are derived from the wavenumbers(column 6). The ID letters in column 7 offer a simple shorthand for labelling transitions used to fit absorption systems. The q coefficients and their uncertainties are from Dzuba et al. (1999a,b, 2001, 2002) and Berengut et al. (2004a,b).

Ion	Tran.	A	ω_0 [cm^{-1}]	Ref.	λ_0 [Å]	ID	q [cm^{-1}]
Mg I	2026	24.31	49346.772611(36)	a	2026.4749792(15)	a_1	87(7)
	2852	24.31	35051.28076(19)	b	2852.962797(15)	a_2	86(10)
Mg II	2796	24.31	35760.85409(20)	c	2796.353794(16)	b_1	211(10)
	2803	24.31	35669.30439(20)	c	2803.530983(16)	b_2	120(2)
Al II	1670	26.98	59851.976(4)	d	1670.78861(11)	c_1	270(30)
Al III	1854	26.98	53916.554(1)	d	1854.717941(34)	d_1	464(30)
	1862	26.98	53682.884(2)	d	1862.791127(69)	d_2	216(30)
Si II	1526	28.09	65500.4538(7)	d	1526.706980(16)	e_1	50(30)
	1808	28.09	55309.3404(4)	d	1808.012883(13)	e_2	520(30)
Si IV	1393	28.09	71748.355(2)	d	1393.760177(39)	f_1	862(20)
	1402	28.09	71287.376(2)	d	1402.772912(39)	f_2	346(20)
Ti II	3067	47.87	32602.627(2)	g	3067.23750(19)	g_1	791(50)
	3073	47.87	32532.355(1)	g	3073.86293(9)	g_2	677(50)
	3230	47.87	30958.586(1)	g	3230.12169(10)	g_3	673(50)
	3242	47.87	30836.426(1)	g	3242.91797(11)	g_4	541(50)
	3384	47.87	29544.454(1)	g	3384.73001(11)	g_5	396(50)
Cr II	2056	52.00	48632.058(2)	g	2056.256801(85)	h_1	1110(150)

Continued on next page

Table B.1 – continued from previous page

Ion	Tran.	A	ω_0 [cm^{-1}]	Ref.	λ_0 [Å]	ID	q [cm^{-1}]
	2062	52.00	48491.057(2)	g	2062.235929(85)	h_2	$-1280(150)$
	2066	52.00	48398.871(2)	g	2066.163899(85)	h_3	$-1360(150)$
Mn II	2576	54.94	38806.689(3)	g	2576.87534(20)	i_1	$1420(150)$
	2594	54.94	38543.121(3)	g	2594.49669(20)	i_2	$1148(150)$
	2606	54.94	38366.230(3)	g	2606.45886(20)	i_3	$986(150)$
Fe II	1608	55.85	62171.629(3)	l	1608.450697(78)	j_1	$-1300(300)$
	1611	55.85	62065.532(3)	l	1611.200239(78)	j_2	$1100(300)$
	2260	55.85	44232.534(6)	g	2260.77936(31)	j_3	$1435(150)$
	2344	55.85	42658.243(2)	g	2344.21282(11)	j_4	$1210(150)$
	2374	55.85	42114.836(2)	g	2374.46015(11)	j_5	$1590(150)$
	2382	55.85	41968.065(2)	g	2382.76413(11)	j_6	$1460(150)$
	2586	55.85	38660.052(2)	g	2586.64939(13)	j_7	$1490(150)$
	2600	55.85	38458.991(2)	g	2600.17222(14)	j_8	$1330(150)$
Ni II	1709	58.69	58493.075(4)	m	1709.60409(12)	k_1	$-20(250)$
	1741	58.69	57420.017(4)	m	1741.55295(12)	k_2	$-1400(250)$
	1751	58.69	57080.377(4)	m	1751.91555(12)	k_3	$-700(250)$
Zn II	2026	65.41	49355.005(2)	g	2026.136964(82)	l_1	$2479(25)$
	2062	65.41	48481.081(2)	g	2062.660278(85)	l_2	$1584(25)$

[a] Hannemann et al. (2006); [b] Salumbides et al. (2006); [c] Batteiger et al. (2009); [d] Griesmann & Kling (2000); [g] Aldenius et al. (2006); [l] King's Ph.D. Thesis (2012); [m] Pickering et al. (2000);

Appendix C.

$\Delta\alpha/\alpha$ values from UVES/VLT

The $\Delta\alpha/\alpha$ values from the MM analysis of the 154 VLT absorbers in King's Ph.D. Thesis (2012) are presented in table C.1. (An ASCII version of this table is available at http://astronomy.swin.edu.au/~mmurphy/pub.html).

Table C.1: Results for $\Delta\alpha/\alpha$ derived from MM absorbers for the UVES/VLT dataset in King's Ph.D. Thesis (2012). Errors given are purely statistical. The emission redshift of the quasar and absorption redshift are given by $z_{\rm em}$ and $z_{\rm abs}$ respectively. $z_{\rm abs}$ is given as the redshift of the highest column density component in the fit. The value of $\Delta\alpha/\alpha$ and its 1σ statistical uncertainty is given in the last column. The key for the transition labels is given in table B.1.

Quasar name	$z_{\rm em}$	$z_{\rm abs}$	Transitions	$\Delta\alpha/\alpha\,(10^{-5})$
J000344−232355	2.28	0.4521	$a_2b_1b_2j_4j_5j_6j_7j_8$	-0.459 ± 0.787
J000344−232355	2.28	0.9491	$a_2b_1b_2j_4j_6j_8$	-1.534 ± 2.788
J000344−232355	2.28	1.5864	$a_2j_1j_4j_5j_6j_7j_8c_1e_1$	-0.410 ± 1.003
J000448−415728	2.76	1.5419	$b_1b_2j_4j_5j_6j_7j_8$	-5.270 ± 0.906
J000448−415728	2.76	1.9886	$j_4j_6j_7j_8c_1d_1d_2$	0.266 ± 1.945
J000448−415728	2.76	2.1679	$b_1j_1j_4j_5j_6c_1e_1$	1.381 ± 0.944
J001210−012207	2.00	1.2030	$b_1b_2j_4j_6j_7j_8c_1$	0.772 ± 1.190
J001602−001225	2.09	0.6351	$b_1b_2j_4j_6j_8$	-0.673 ± 3.545
J001602−001225	2.09	0.6363	$b_1b_2j_4j_6j_8$	-1.561 ± 3.914
J001602−001225	2.09	0.8575	$b_1b_2j_7j_8$	1.266 ± 1.826
J001602−001225	2.09	1.1468	$b_1b_2j_6j_8$	-1.581 ± 2.922
J001602−001225	2.09	2.0292	$a_2j_1j_4j_6j_7j_8d_1d_2e_1$	-0.909 ± 0.934
J004131−493611	3.24	2.1095	$b_1b_2j_7j_8c_1d_1d_2$	0.386 ± 2.856
J004131−493611	3.24	2.2485	$j_1j_2j_3j_6j_7j_8c_1d_1d_2e_2h_1h_2h_3l_1l_2k_1i_1i_2$	-1.230 ± 0.672
J005758−264314	3.65	1.2679	$a_2b_1b_2j_6j_7j_8$	1.076 ± 1.931
J005758−264314	3.65	1.5336	$b_2j_3j_4j_5j_6j_7h_1i_1i_2$	-0.456 ± 0.903
J010311+131617	2.68	1.7975	$a_2j_1j_4j_5j_6e_2$	0.443 ± 0.548
J010311+131617	2.68	2.3092	$j_1j_2c_1e_1e_2h_1h_2h_3l_1l_2k_1k_2$	-0.082 ± 0.563
J011143−350300	2.41	1.1827	$a_2b_1b_2j_4j_6j_7j_8$	0.142 ± 0.950
J011143−350300	2.41	1.3499	$b_1b_2j_4j_5j_6j_7j_8$	0.084 ± 0.378
J012417−374423	2.20	0.8221	$a_2b_1b_2j_4j_6j_7j_8$	0.702 ± 1.050

Continued on next page

Table C.1 – continued from previous page

Quasar name	$z_{\rm em}$	$z_{\rm abs}$	Transitions	$\Delta\alpha/\alpha\,(10^{-5})$
J012417−374423	2.20	0.8593	$a_2b_1b_2j_5j_6j_7j_8$	-0.677 ± 2.516
J012417−374423	2.20	1.2433	$a_2b_1b_2j_4j_5j_6h_2k_2k_3$	1.838 ± 1.221
J012417−374423	2.20	1.9102	$j_4j_8c_1d_1d_2e_1$	-3.872 ± 3.111
J013105−213446	1.90	1.8566	$j_3j_4j_5j_6d_1d_2e_2h_1k_1k_2k_3$	0.236 ± 1.445
J014333−391700	1.81	0.3400	$b_1b_2j_7j_8$	-6.748 ± 3.914
J014333−391700	1.81	1.7101	$b_1j_4j_6j_8c_1d_1d_2e_1$	-1.465 ± 2.357
J015733−004824	1.55	0.7693	$b_1b_2j_6$	2.647 ± 4.288
J010821+062327	1.96	1.9328	j_7e_1	2.184 ± 2.454
J024008−230915	2.22	1.1846	$a_2b_1b_2j_6j_8$	-1.513 ± 2.754
J024008−230915	2.22	1.6359	$a_2b_1b_2j_1j_4j_7j_8d_1d_2e_1$	1.000 ± 1.110
J024008−230915	2.22	1.6373	$a_2b_1b_2j_1j_4j_7j_8$	-0.187 ± 1.020
J024008−230915	2.22	1.6574	$b_1b_2j_4j_6c_1e_1$	-0.137 ± 1.010
J033106−382404	2.42	0.7627	$a_2b_1b_2j_5j_6j_7j_8$	0.440 ± 0.988
J033106−382404	2.42	0.9709	$b_1b_2j_8$	-4.485 ± 4.216
J033106−382404	2.42	1.4380	$b_1b_2j_4j_8$	-4.323 ± 2.571
J033108−252443	2.69	0.9925	$b_1b_2j_4j_8$	0.513 ± 1.232
J033108−252443	2.69	2.4547	j_1e_1	-2.122 ± 5.496
J033244−445557	2.60	2.4112	$j_1j_4j_6j_7c_1e_1e_2$	-1.000 ± 0.793
J033244−445557	2.60	2.6563	$j_1j_4j_5j_6c_1e_1$	1.079 ± 1.689
J040718−441013	3.00	2.4126	$j_5j_6j_8c_1d_1d_2$	2.420 ± 2.220
J040718−441013	3.00	2.5499	$j_1j_4j_6c_1e_1e_2k_1k_2$	0.895 ± 0.353
J040718−441013	3.00	2.5948	$j_1j_2j_5j_6c_1d_1d_2e_1e_2h_1h_2h_3l_2k_1k_2$	0.574 ± 0.345
J040718−441013	3.00	2.6214	$j_1c_1e_1$	4.264 ± 2.744
J042707−130253	2.16	1.4080	$b_1b_2j_1j_4j_5j_6j_7j_8c_1$	-2.551 ± 1.110
J042707−130253	2.16	1.5632	$j_4j_6j_8c_1e_1$	-2.967 ± 2.449
J042707−130253	2.16	2.0351	$j_1c_1e_2$	8.057 ± 3.830
J043037−485523	1.94	1.3556	$a_2j_1j_2j_3j_4j_5j_6j_7j_8c_1e_1e_2h_1h_3k_1k_2k_3i_1i_2i_3$	-0.405 ± 0.232
J044017−433308	2.86	1.4335	$b_1b_2j_4j_7j_8$	0.139 ± 2.500
J044017−433308	2.86	2.0482	$j_1j_2j_4c_1e_2h_1h_2h_3l_2k_1k_2k_3i_2i_3$	1.400 ± 0.864
J051707−441055	1.71	0.2223	$a_2b_1b_2j_8$	1.262 ± 3.703
J051707−441055	1.71	0.4291	$a_2b_1j_4j_6j_7j_8$	-3.153 ± 1.502
J053007−250329	2.81	2.1412	$b_1b_2j_1j_2j_5c_1h_1k_1k_2k_3$	0.676 ± 0.359
J055246−363727	2.32	1.2252	$a_2b_1b_2j_4j_5j_6j_7c_1e_1$	0.269 ± 0.895
J055246−363727	2.32	1.7475	$a_2j_1j_4j_5j_6j_7j_8e_1$	-0.936 ± 1.155
J055246−363727	2.32	1.9565	$j_1j_4j_6c_1d_1d_2e_1$	1.740 ± 1.530
J064326−504112	3.09	2.6592	$j_4j_5j_6c_1d_1d_2e_2l_1k_1k_2$	-1.530 ± 1.920

Continued on next page

Table C.1 – continued from previous page

Quasar name	$z_{\rm em}$	$z_{\rm abs}$	Transitions	$\Delta\alpha/\alpha\,(10^{-5})$
J091613+070224	2.77	1.3324	$a_2b_1b_2j_4j_6j_7j_8$	8.233 ± 5.915
J094253−110426	3.05	1.0595	$a_2b_1j_4j_7j_8$	0.372 ± 0.737
J094253−110426	3.05	1.7891	$b_1b_2j_4j_5j_6$	-2.330 ± 0.495
J103909−231326	3.13	1.4429	$b_1j_7j_8$	-1.980 ± 2.720
J103909−231326	3.13	2.7778	$j_1j_2j_4c_1h_1h_2h_3l_2k_1k_2k_3$	-1.130 ± 0.660
J103921−271916	2.23	0.8771	$a_2b_2j_6j_8$	2.159 ± 2.071
J103921−271916	2.23	1.0093	$b_1b_2j_8$	-0.643 ± 3.280
J103921−271916	2.23	1.9721	$j_4j_5j_6j_7c_1e_1$	2.980 ± 0.847
J104032−272749	2.32	1.3861	$a_2b_1b_2j_3j_5j_6j_7j_8e_1h_1h_3k_1k_2k_3i_1i_2g_4g_5$	0.446 ± 0.693
J104032−272749	2.32	1.7761	$b_1b_2j_1j_4j_5j_6c_1e_1$	0.262 ± 1.320
J110325−264515	2.15	1.1868	$a_2b_1b_2j_4j_5j_6j_7j_8$	-0.745 ± 0.925
J110325−264515	2.15	1.2029	$b_1b_2j_4j_6j_7j_8$	0.623 ± 0.830
J110325−264515	2.15	1.5515	$b_1b_2j_4j_6j_8c_1e_1$	-0.669 ± 0.998
J110325−264515	2.15	1.8389	$a_2j_1j_4j_5e_1$	0.612 ± 0.395
J111113−080401	3.92	3.6077	j_1e_1	22.962 ± 16.134
J112010−134625	3.96	1.6283	$b_2j_4j_5j_6$	0.886 ± 1.130
J112442−170517	2.40	0.8062	$b_1b_2j_4j_5j_6j_7j_8$	1.738 ± 1.373
J112442−170517	2.40	1.2342	$a_2b_1b_2j_4j_6j_8d_1d_2$	2.271 ± 1.571
J115411+063426	2.76	1.7739	$j_4j_5j_6e_2h_1h_2h_3l_1l_2k_1k_2k_3i_1i_3$	-0.739 ± 0.784
J115411+063426	2.76	1.8197	$b_1b_2j_1j_6j_7j_8c_1$	-0.948 ± 0.974
J115411+063426	2.76	2.3660	$j_1j_7j_8c_1e_1$	3.090 ± 1.780
J115944+011206	2.00	0.7908	$b_1b_2j_4j_6j_8$	1.561 ± 1.080
J115944+011206	2.00	1.3305	$b_1b_2j_4j_6j_7j_8c_1$	2.137 ± 2.249
J115944+011206	2.00	1.9438	$a_2j_1j_2j_3j_5e_1e_2h_1h_3k_1k_2k_3i_1$	0.518 ± 0.442
J120342+102831	1.89	1.3224	$a_2b_1b_2j_4j_6j_7j_8c_1e_1$	-0.965 ± 1.930
J120342+102831	1.89	1.3422	$a_2b_1b_2j_1j_6j_7j_8e_1$	-2.006 ± 1.443
J120342+102831	1.89	1.5789	$a_2j_4j_6j_7j_8e_1$	1.743 ± 2.716
J121140+103002	2.19	1.0496	$a_2b_1b_2j_4j_5j_6j_7j_8$	-1.538 ± 0.672
J123200−022404	1.04	0.7569	$a_2b_1b_2j_4j_6$	2.253 ± 3.219
J123200−022404	1.04	0.8308	$a_2b_1b_2j_4j_6j_7j_8$	1.672 ± 0.911
J123437+075843	2.57	1.0201	$a_2j_4j_6j_7j_8$	-2.213 ± 1.442
J123437+075843	2.57	1.7194	$j_1j_4j_5j_6d_1d_2e_2$	0.485 ± 0.943
J133335+164903	2.08	0.7446	$a_2b_1b_2j_4j_5j_6j_7$	-0.828 ± 0.542
J133335+164903	2.08	1.3253	$a_2b_1j_6j_8c_1$	4.962 ± 10.607
J133335+164903	2.08	1.7765	$b_1b_2j_1j_5j_6c_1e_1e_2h_1h_2l_2k_1k_2k_3i_1$	0.843 ± 0.448
J133335+164903	2.08	1.7863	$a_2b_1j_6c_1d_1d_2e_1e_2$	-0.489 ± 0.860

Continued on next page

Table C.1 – continued from previous page

Quasar name	$z_{\rm em}$	$z_{\rm abs}$	Transitions	$\Delta\alpha/\alpha\,(10^{-5})$
J134427−103541	2.13	1.9155	$j_1 j_4 j_5 j_6 j_7 j_8 e_1 e_2$	0.015 ± 0.744
J134427−103541	2.13	2.1474	$b_1 b_2 c_1$	6.448 ± 8.831
J135038−251216	2.53	1.4393	$a_1 b_1 b_2 j_1 j_3 j_8 d_1 d_2 h_2 h_3 l_1 l_2 k_2 k_3 i_1 i_2 i_3$	-0.987 ± 0.568
J135038−251216	2.53	1.7529	$b_2 j_6 j_8 c_1 d_1 d_2$	6.396 ± 3.258
J141217+091624	2.86	1.4187	$b_2 j_4 j_5 j_7 j_8$	-2.919 ± 1.771
J141217+091624	2.86	2.0188	$j_1 j_3 j_4 c_1 d_1 d_2 e_2 h_1 h_2 h_3 k_1 k_2 k_3$	0.849 ± 0.755
J141217+091624	2.86	2.4564	$j_1 j_4 j_7 e_1$	-0.903 ± 1.390
J141217+091624	2.86	2.6682	$j_1 j_5 j_6 c_1 e_1$	0.199 ± 0.849
J143040+014939	2.11	0.4878	$a_2 b_2 j_7 j_8 i_2 i_3$	3.580 ± 2.170
J143040+014939	2.11	1.2030	$b_1 b_2 j_7 j_8$	-0.812 ± 3.290
J143040+014939	2.11	1.2411	$a_2 b_1 b_2 j_7 j_8 e_2 h_1 h_2 h_3 l_2 k_2 k_3 i_1 i_2 i_3$	-2.660 ± 1.200
J144653+011356	2.21	0.5097	$b_1 b_2 j_4 j_8$	-0.567 ± 1.142
J144653+011356	2.21	0.6602	$a_2 b_1 b_2 j_6 j_7 j_8$	-0.073 ± 1.831
J144653+011356	2.21	1.1020	$b_1 b_2 j_6 j_8$	1.395 ± 4.030
J144653+011356	2.21	1.1292	$a_2 b_2 j_4 j_6 j_8$	2.278 ± 2.760
J144653+011356	2.21	1.1595	$a_2 b_1 b_2 j_4 j_5 j_6 j_7$	-2.557 ± 1.205
J145102−232930	2.21	1.5855	$j_6 j_8 c_1 d_1 d_2 e_1$	-4.500 ± 2.456
J200324−325144	3.77	2.0329	$a_2 b_1 b_2 j_6 j_7 j_8$	2.440 ± 1.200
J200324−325144	3.77	3.1878	$j_1 j_4 c_1 e_1 e_2$	3.411 ± 1.153
J200324−325144	3.77	3.1917	$j_1 e_1$	2.238 ± 4.217
J212912−153841	3.27	1.7380	$a_2 j_4 j_5 j_6 j_7 j_8 e_1$	1.310 ± 0.636
J212912−153841	3.27	2.0225	$b_2 j_4 j_7 j_8 e_1$	-1.628 ± 1.244
J212912−153841	3.27	2.6378	$c_1 e_1 e_2 k_1 k_2 k_3$	1.320 ± 3.330
J212912−153841	3.27	2.7686	$j_1 e_1 e_2$	-0.206 ± 1.090
J213314−464030	2.20	1.6148	$j_1 j_4 j_5 j_6 c_1 e_1$	4.320 ± 1.568
J214159−441325	3.17	2.1329	$b_1 b_2 j_4 j_6 e_1$	-0.470 ± 2.222
J214159−441325	3.17	2.3828	$j_4 j_5 j_7 j_8 c_1 h_1 h_2 l_1 l_2 k_1 k_3 i_1 i_3$	1.170 ± 0.858
J214159−441325	3.17	2.8523	$j_1 j_2 j_3 j_5 c_1 e_1 e_2 h_1 h_3 k_1 k_2 k_3$	2.089 ± 0.524
J214225−442018	3.23	0.9865	$b_1 b_2 j_8$	-0.093 ± 1.050
J214225−442018	3.23	1.0529	$a_2 b_1 b_2 j_8$	1.500 ± 1.290
J214225−442018	3.23	1.1543	$a_2 b_1 b_2 j_7 j_8$	-6.250 ± 4.000
J214225−442018	3.23	1.7569	$b_1 b_2 j_4 j_6 j_8$	-6.183 ± 4.308
J214225−442018	3.23	2.1126	$a_1 a_2 b_1 b_2 j_3 j_4 j_5 j_7 j_8 e_2 h_1 h_2 h_3 l_1 l_2 k_1 k_2 k_3 i_1 i_3$	1.177 ± 0.858
J214225−442018	3.23	2.2533	$j_4 j_5 j_6 j_7 j_8 c_1 e_1 e_2$	2.220 ± 1.120
J214225−442018	3.23	2.3798	$j_1 j_4 j_5 j_6 j_7 j_8 c_1 e_1 e_2$	0.747 ± 1.510
J220734−403655	3.15	1.6270	$j_4 j_6 j_7 c_1$	6.091 ± 2.709

Continued on next page

Table C.1 – continued from previous page

Quasar name	$z_{\rm em}$	$z_{\rm abs}$	Transitions	$\Delta\alpha/\alpha\,(10^{-5})$
J220852−194359	2.56	0.9478	$a_2b_1b_2j_6j_7j_8$	0.151 ± 1.305
J220852−194359	2.56	0.9483	$b_1b_2j_6j_7j_8$	-2.686 ± 2.009
J220852−194359	2.56	1.0172	$a_2b_1j_4j_5j_6j_7j_8$	-0.525 ± 0.546
J220852−194359	2.56	1.0182	$b_1b_2j_4j_6j_7j_8$	-0.412 ± 1.040
J220852−194359	2.56	1.2970	$a_2b_1b_2j_6j_8$	-1.435 ± 2.763
J220852−194359	2.56	1.9206	$j_1j_3j_4j_7c_1e_1e_2h_1h_2h_3l_1l_2k_1k_2k_3i_1$	0.857 ± 0.385
J220852−194359	2.56	2.0762	$j_1j_4j_5j_6c_1k_1k_2k_3$	0.942 ± 0.584
J222006−280323	2.41	0.7866	$b_1b_2j_4j_6j_8$	-0.557 ± 1.479
J222006−280323	2.41	0.9408	$b_1b_2j_4j_6j_8$	1.691 ± 1.762
J222006−280323	2.41	0.9424	$a_2b_1b_2j_4j_6j_7j_8$	0.988 ± 1.250
J222006−280323	2.41	1.5554	$b_1j_4j_6j_7j_8c_1$	0.945 ± 0.604
J222006−280323	2.41	1.6279	$a_2b_1j_1j_4j_6j_7j_8c_1$	2.300 ± 0.861
J222756−224302	1.89	1.4129	$b_1b_2j_4j_5j_6j_7j_8c_1d_1d_2e_1e_2$	-1.649 ± 1.785
J222756−224302	1.89	1.4334	$b_1b_2j_4j_8c_1d_1d_2e_1$	-4.507 ± 2.935
J222756−224302	1.89	1.4518	$b_1j_4j_6j_7j_8c_1e_1$	1.024 ± 1.586
J222756−224302	1.89	1.6398	$a_2b_1b_2j_4j_5j_7j_8c_1d_1d_2e_1$	-1.484 ± 2.957
J233446−090812	3.32	2.1522	$a_1b_1b_2j_1j_3j_4j_5j_6d_1d_2h_1h_2h_3l_1l_2k_1k_2k_3i_1$	0.525 ± 0.437
J233446−090812	3.32	2.2015	$j_4c_1e_2$	-0.058 ± 5.494
J233446−090812	3.32	2.2875	$j_1j_4j_5j_8e_2h_1h_3k_2k_3i_2i_3$	0.758 ± 0.376
J234625+124743	2.58	2.1733	$j_1c_1e_1$	4.160 ± 7.517
J234625+124743	2.58	2.5718	$j_1e_1e_2$	-17.274 ± 6.799
J234628+124858	2.52	1.1084	$b_2j_4j_8$	-1.536 ± 2.527
J234628+124858	2.52	1.5899	$j_6j_7e_1$	3.051 ± 2.268
J234628+124858	2.52	2.1713	$b_2j_1j_4j_6c_1d_1d_2$	-0.794 ± 0.951
J235034−432559	2.88	1.7962	$b_1j_6d_1d_2e_1$	0.942 ± 3.357

Appendix D.

$\Delta\alpha/\alpha$ values from HIRES/Keck

The $\Delta\alpha/\alpha$ values from the MM analysis of the 128 Keck absorbers in Murphy's Ph.D. Thesis (2002) are presented in table D.1. (An ASCII version of this table is available at http://astronomy.swin.edu.au/~mmurphy/pub.html).

Table D.1: Results for $\Delta\alpha/\alpha$ derived from MM absorbers for the HIRES/Keck dataset in Murphy's Ph.D. Thesis (2002). Errors given are purely statistical. The emission redshift of the quasar and absorption redshift are given by $z_{\rm em}$ and $z_{\rm abs}$ respectively. $z_{\rm abs}$ is given as the redshift of the highest column density component in the fit. The value of $\Delta\alpha/\alpha$ and its 1σ statistical uncertainty is given in the last column. The key for the transition labels is given in table B.1.

Quasar name	$z_{\rm em}$	$z_{\rm abs}$	Transitions	$\Delta\alpha/\alpha\,(10^{-5})$
J000520+052410	1.9	0.85118	$b_1b_2j_4j_5j_6j_7j_8$	-0.346 ± 1.279
J012017+213346	1.49	0.72913	$a_2b_1b_2j_7j_8$	0.084 ± 1.297
J012017+213346	1.49	1.0479	$b_1b_2j_4j_6j_8$	-0.223 ± 2.2
J012017+213346	1.49	1.3246	$b_1b_2j_6j_7j_8$	0.695 ± 0.803
J012017+213346	1.49	1.3428	$b_2j_4j_6j_7$	-1.29 ± 0.948
J042315−012033	0.915	0.63308	$a_2b_1b_2j_8$	4.211 ± 4.076
J045312−130546	2.25	1.1743	$b_1j_4j_5j_6j_8$	-3.07 ± 1.098
J045312−130546	2.25	1.2294	$b_1b_2j_4j_6j_7j_8$	-1.472 ± 0.836
J045312−130546	2.25	1.2324	$b_1b_2j_6$	1.017 ± 2.752
J045647+040052	1.34	0.85929	$a_2b_2j_4j_5j_6j_8j_7$	0.405 ± 1.325
J045647+040052	1.34	1.1534	$b_1b_2j_4j_7j_8$	-0.749 ± 1.782
J082601−223027	0.91	0.91059	$b_1b_2j_4j_6j_7j_8$	-0.394 ± 0.609
J115129+382552	1.3	0.55339	$b_1b_2j_7j_8$	-1.861 ± 1.716
J120858+454035	1.16	0.92741	$b_1b_2j_4j_5j_6j_7j_8$	-0.218 ± 1.389
J121549−003432	2.69	1.3196	$a_2b_1b_2j_4j_5j_6j_7j_8$	-0.738 ± 0.76
J121549−003432	2.69	1.5541	$b_1b_2j_4j_5j_6j_7j_8$	-1.268 ± 0.892
J122527+223512	2.05	0.66802	$b_1b_2j_4j_6j_8$	0.067 ± 1.474
J122824+312837	2.22	1.7954	$a_2b_1b_2j_4j_5j_6j_8$	-1.296 ± 1.049
J125048+395139	1.03	0.77292	$b_1b_2j_4j_5j_6j_7j_8$	2.165 ± 1.191
J125048+395139	1.03	0.85452	$b_1b_2j_4j_6j_7j_8$	-0.021 ± 1.268
J125659+042734	1.02	0.51934	$a_2b_1b_2j_7j_8$	-3.371 ± 3.247

Continued on next page

Table D.1 – continued from previous page

Quasar name	$z_{\rm em}$	$z_{\rm abs}$	Transitions	$\Delta\alpha/\alpha\,(10^{-5})$
J125659+042734	1.02	0.93426	$b_1b_2j_4j_6j_7j_8$	1.485 ± 1.908
J131956+272808	1.01	0.66004	$b_1b_2j_4j_6j_7j_8$	0.59 ± 1.515
J142326+325220	1.91	0.84324	$b_1b_2j_4j_5j_6j_7j_8$	0.099 ± 0.847
J142326+325220	1.91	0.90301	$b_1b_2j_4j_5j_6j_7j_8$	-0.998 ± 1.783
J142326+325220	1.91	1.1726	$b_1b_2j_4j_6j_8$	-2.844 ± 1.448
J163429+703132	1.34	0.9901	$b_1b_2j_4j_6j_7j_8$	1.094 ± 2.459
J002208−150538	4.53	3.4388	$e_1e_2j_1$	0.925 ± 3.958
J010311+131617	2.68	2.3095	$d_1d_2e_1h_2h_3j_1j_2l_1l_2$	-3.941 ± 1.368
J015234+335033	2.43	2.1408	$c_1d_1d_2e_1e_2h_1h_2h_3j_1j_2k_1k_2k_3$	-5.112 ± 2.118
J020455+364917	2.49	1.4761	$b_2j_4j_5j_7j_8$	-0.647 ± 1.219
J020455+364917	2.49	1.955	$d_1e_2h_1j_1$	1.989 ± 1.048
J020455+364917	2.49	2.324	$c_1d_1e_1e_2j_1$	0.758 ± 1.592
J020455+364917	2.49	2.4563	$c_1e_1j_1$	-3.731 ± 2.285
J020455+364917	2.49	2.4628	$e_1e_2h_1j_1k_2k_3$	0.572 ± 1.719
J034943−381031	3.23	3.0247	e_1j_1	-2.795 ± 3.429
J084424+124548	2.55	2.3742	$c_1e_1e_2h_1h_2k_2k_3l_1l_2$	2.277 ± 3.816
J084424+124548	2.55	2.4761	$c_1e_1e_2h_1h_2h_3j_1j_2k_2k_3$	-4.304 ± 1.944
J121732+330538	2.61	1.999	$c_1d_1d_2e_1e_2h_1h_2j_1j_2k_2k_3l_1l_2$	5.648 ± 3.131
J175746+753916	3.05	2.6253	$d_1e_1e_2h_3j_1j_2k_1k_2k_3$	-0.75 ± 1.387
J175746+753916	3.05	2.6253	$c_1e_1j_1j_2k_1k_2k_3$	-0.492 ± 1.645
J220852−194359	2.56	0.94841	$b_1b_2j_4j_6j_7j_8$	-3.659 ± 1.855
J220852−194359	2.56	1.0172	$a_2b_1b_2j_4j_5j_6j_7j_8$	-0.322 ± 0.732
J220852−194359	2.56	1.9204	$c_1e_1e_2h_1h_2h_3j_1j_2k_1k_2k_3l_1l_2$	1.878 ± 0.702
J223235+024755	2.15	1.8585	$c_1e_1e_2h_2j_1j_4j_6k_1k_2k_3$	-5.407 ± 1.179
J223235+024755	2.15	1.864	$e_1e_2h_1h_2h_3j_1j_2j_4j_5k_1k_2k_3l_1l_2$	-0.998 ± 0.492
J223408+000001	3.02	2.0653	$e_1e_2h_2h_3j_1j_2k_2k_3l_1l_2$	-2.604 ± 1.015
J235129−142748	2.94	2.2794	$e_1e_2j_1$	1.346 ± 4.18
J000149−015940	2.31	2.0951	$c_1e_1e_2h_1h_2h_3j_1k_1k_2k_3l_1l_2$	-0.068 ± 0.722
J000149−015940	2.31	2.1539	$c_1d_2e_1j_1$	4.346 ± 3.338
J000322−260316	4.11	1.4342	$b_1b_2j_6j_8$	-1.256 ± 1.167
J000322−260316	4.11	3.3897	$c_1e_1j_1j_2$	-7.666 ± 3.231
J000520+052410	1.9	0.59137	$b_1b_2j_4j_6j_7j_8$	-3.1 ± 2.428
J000520+052410	1.9	0.85118	$d_1d_2j_4j_5j_6j_7j_8$	0.494 ± 1.021
J005757−264314	3.66	1.2679	$a_2b_1b_2j_6j_7j_8$	1.669 ± 2.745
J005757−264314	3.66	1.3192	$b_1b_2j_6j_7j_8$	-2.642 ± 2.457
J005757−264314	3.66	1.5337	$a_2b_1b_2j_4j_5j_6j_7j_8$	-1.319 ± 1.072

Continued on next page

Table D.1 – continued from previous page

Quasar name	$z_{\rm em}$	$z_{\rm abs}$	Transitions	$\Delta\alpha/\alpha\,(10^{-5})$
J010054+021136	1.96	0.61256	$b_1b_2j_4j_5j_6j_7j_8$	0.374 ± 1.189
J010054+021136	1.96	0.72508	$b_1b_2j_4j_6j_7j_8$	-2.637 ± 3.522
J012227−042127	1.95	0.65741	$b_1b_2j_4j_5j_6j_7j_8$	7.123 ± 4.599
J015734+744243	2.33	0.7455	$b_1b_2j_4j_6j_7j_8$	-2.168 ± 0.778
J020944+051714	4.19	3.6663	$c_1e_1j_1$	-0.748 ± 3.468
J021857+081727	2.99	1.768	$d_1d_2j_1j_4j_5j_6j_7j_8$	0.044 ± 1.235
J024008−230915	2.23	1.365	$c_1d_1e_1e_2j_1j_4j_5j_6$	-0.197 ± 0.565
J024401−013402	4.04	2.0994	$c_1j_4j_5j_6$	-0.739 ± 2.675
J030450−221157	1.41	1.0092	$a_2b_1b_2j_4j_5j_6j_7j_8$	-0.189 ± 1.008
J045142−132032	3.09	1.2667	$a_2b_1b_2j_4j_5j_6j_7$	-1.212 ± 1.43
J053007−250329	2.77	0.94398	$b_1b_2j_8$	0.759 ± 2.335
J053007−250329	2.77	2.1406	$c_1e_1e_2h_1h_2h_3j_1j_4j_6k_1k_2k_3$	-0.853 ± 0.88
J053007−250329	2.77	2.8114	$c_1d_1d_2e_1h_1h_2h_3j_1j_2k_1k_2k_3l_1l_2$	0.85 ± 0.846
J064204+675835	3.17	1.2938	$b_1b_2j_6j_7j_8$	-1.392 ± 0.623
J074521+473436	3.21	1.6112	$a_2b_1b_2j_4j_6j_7$	-1.299 ± 1.726
J074521+473436	3.21	3.0173	$c_1e_1e_2j_1$	0.794 ± 1.796
J080117+521034	3.24	2.6021	$c_1d_1d_2j_1$	-1.396 ± 1.955
J080117+521034	3.24	2.8677	$c_1e_1j_1$	3.837 ± 3.288
J084424+124548	2.55	1.0981	$b_1j_4j_5j_6j_8$	-3.589 ± 1.203
J084424+124548	2.55	1.1314	$a_2b_1b_2j_4j_6j_7j_8$	0.562 ± 0.787
J084424+124548	2.55	1.2189	$a_2b_1b_2j_4j_5j_6j_7j_8l_1l_2$	-0.522 ± 0.542
J084424+124548	2.55	2.3742	$c_1d_1e_1e_2h_1h_2h_3j_4j_7j_8k_2k_3l_1l_2$	1.435 ± 1.227
J093337+284532	3.42	3.2351	$c_1e_1j_1$	0.867 ± 1.777
J094253−110425	3.05	1.0598	$a_2b_1b_2j_4j_6j_7j_8$	-0.453 ± 1.572
J095852+120245	3.31	2.3103	$c_1d_1d_2j_1$	-2.161 ± 5.977
J101155+294141	2.62	1.1117	$b_1b_2j_4j_6j_7j_8$	-5.461 ± 2.518
J101447+430030	3.1	1.4162	$b_1b_2j_4j_5j_6j_7j_8$	-0.892 ± 0.552
J101447+430030	3.1	2.9587	$c_1d_1e_1e_2j_1j_2k_1k_3$	2.475 ± 1.706
J105756+455553	4.12	3.3172	$c_1e_1j_1$	2.706 ± 5.677
J111038+483115	2.97	0.80757	$a_2b_1b_2j_6j_7$	1.199 ± 1.222
J111038+483115	2.97	0.86182	$a_2b_1b_2j_7j_8$	-2.03 ± 1.632
J111038+483115	2.97	1.0158	$a_2b_1b_2j_6$	-2.086 ± 0.934
J113508+222715	2.88	2.1053	$c_1d_1d_2e_1j_1$	6.323 ± 3.622
J120523−074232	4.7	1.7549	$b_1b_2j_7j_8$	-1.465 ± 2.182
J120858+454035	1.16	0.92741	$a_2b_1b_2j_4j_5j_6j_7j_8$	-0.275 ± 0.776
J122607+173649	2.94	2.4653	$e_2h_1h_2h_3j_2k_1k_3l_1l_2$	1.635 ± 1.919

Continued on next page

Table D.1 – continued from previous page

Quasar name	$z_{\rm em}$	$z_{\rm abs}$	Transitions	$\Delta\alpha/\alpha\,(10^{-5})$
J122607+173649	2.94	2.5577	$c_1e_1j_1j_4j_6$	0.546 ± 1.199
J122824+312837	2.22	1.7954	$c_1d_1d_2e_1e_2j_1$	1.352 ± 1.388
J124714+312641	2.95	0.85048	$b_1b_2j_6j_8$	-6.897 ± 7.012
J124714+312641	2.95	2.7504	$c_1e_1j_1$	2.414 ± 4.11
J131011+460124	2.13	0.22909	$a_2b_1b_2j_8$	2.551 ± 5.392
J134002+110630	2.97	2.7955	$c_1e_2j_1$	4.103 ± 8.538
J142656+602550	3.2	2.7698	$c_1e_1j_1$	-0.688 ± 1.843
J142656+602550	3.2	2.8268	$c_1e_1j_1$	0.433 ± 0.827
J143912+295448	3	1.2259	$a_2b_1b_2j_4j_5j_6j_7j_8$	0.308 ± 1.46
J144453+291905	2.76	2.4389	$c_1e_1j_1$	-0.882 ± 1.473
J155152+191104	2.83	1.1425	$b_2d_2j_4j_6j_7j_8$	-0.076 ± 0.671
J155152+191104	2.83	1.3422	$j_4j_5j_6j_7$	-0.74 ± 1.232
J155152+191104	2.83	1.8024	$c_1d_1d_2$	-3.05 ± 2.473
J162645+642655	2.32	0.58596	$b_1b_2j_8$	-1.977 ± 4.529
J162645+642655	2.32	2.1102	$c_1d_1d_2e_1j_1$	-0.705 ± 1.068
J163429+703132	1.34	0.9901	$a_2b_1b_2c_1j_4j_5j_6j_7j_8$	-2.194 ± 1.343
J185230+401906	2.12	1.99	$e_1e_2h_1h_2h_3j_1j_2j_4j_5j_6j_7j_8l_1l_2$	-1.663 ± 0.859
J194454+770552	3.02	1.7385	$d_1d_2e_2h_1h_2j_2j_4k_2k_3$	-0.212 ± 1.857
J194454+770552	3.02	2.8433	$c_1e_1j_1$	-4.743 ± 1.289
J214805+065738	1	0.79026	$b_1b_2j_4j_5j_6j_7j_8$	0.087 ± 0.589
J220852−194359	2.56	1.0172	$a_2b_1b_2j_7j_8$	1.354 ± 0.883
J220852−194359	2.56	2.0762	c_1j_1	1.429 ± 3.022
J223408+000001	3.02	1.2128	$a_2b_1b_2j_5j_6j_7j_8$	1.223 ± 1.465
J223408+000001	3.02	2.0653	$d_1d_2e_1e_2h_1h_2h_3j_1j_2k_1k_2k_3l_1l_2$	1.707 ± 1.249
J223408+000001	3.02	2.6532	$c_1e_1j_1k_1k_2k_3$	-3.348 ± 1.904
J223619+132620	3.3	2.548	$c_1e_1j_1$	2.942 ± 5.207
J223619+132620	3.3	2.5548	$c_1d_1d_2e_1j_1$	1.732 ± 6.349
J223619+132620	3.3	3.1513	$c_1e_1j_1$	-4.005 ± 3.301
J234628+124859	2.52	0.73117	$a_2b_1b_2j_5j_7j_8$	-1.211 ± 0.975
J234628+124859	2.52	1.5899	$a_2b_2c_1d_1d_2e_1j_7j_8$	0.453 ± 1.187
J234628+124859	2.52	2.1711	$b_2c_1d_1d_2j_4j_6$	-0.961 ± 1.295
J234628+124859	2.52	2.43	$c_1e_1h_1h_2h_3j_1j_4j_7j_8k_1k_2k_3l_1l_2$	-1.224 ± 0.389
J234646+124527	2.77	1.0465	$a_2b_1b_2h_1j_4j_5j_6j_7j_8$	-0.747 ± 1.53
J234646+124527	2.77	1.1161	$a_2b_1b_2j_5j_6j_7j_8$	0.009 ± 1.963
J234646+124527	2.77	2.5378	$c_1e_1j_1$	-3.205 ± 2.094